Doctoral Dissertation

Doctoral Program in Electrical, Electronic and
Communications Engineering (35^{th}cycle)

Analytical Models and Artificial Intelligence for Open and Partially Disaggregated Optical Networks

By

Andrea D'Amico

******

Supervisor(s):
Prof. Vittorio Curri

Doctoral Examination Committee:
Prof. Paolo Serena, Referee, Università degli Studi di Parma
Prof. Oskars Ozoliņš, Referee, RISE Research Institutes of Sweden
Prof. Metodi Plamenov Yankov, Referee, Technical University of Denmark
Prof. Roberto Proietti, Politecnico di Torino
Dr. Stefano Straullu, LINKS Foundation

Politecnico di Torino
2023

Declaration

I hereby declare that, the contents and organization of this dissertation constitute my own original work and does not compromise in any way the rights of third parties, including those relating to the security of personal data.

Andrea D'Amico
2023

* This dissertation is presented in partial fulfillment of the requirements for **Ph.D. degree** in the Graduate School of Politecnico di Torino (ScuDo).

I would like to dedicate this thesis to my loving family

Acknowledgements

This long Ph.D. journey has been an invaluable experience that made me confront challenging problems and incredible moment of discoveries. All of the results that have been achieved despite various obstacles along the way would not have been possible without the people who have surrounded me during these exciting years.

First of all, I want to thank Professor Vittorio Curri for giving me this remarkable opportunity and for introducing me to the optical communications research community. His enthusiastic and tireless approach to research and teaching has been a great inspiration, and with his vast expertise and wise intuition, Prof. Curri has been an irreplaceable guide to my research activities.

I would like to thank all my colleagues at Politecnico di Torino for the constructive discussions and the nice moments: Alessio Ferrari, Emanuele Virgillito, Ihtesham Khan, Dario Pilori, Elliot London, Bruno Vinicius De Araujo Correia, Rasoul Sadeghi Yamchi, Giacomo Borraccini, Rocco D'Ingillo, Renato Ambrosone, Fehmida Usmani, Umar Masood and Hasan Awad.

Also, I want to thanks the researchers of LINKS Foundation, Stefano Straullu, Francesco Aquilino and Antonino Nespola, who carried out numerous experiments essential for the validation of novel proposed methodologies, and all the members of the PSE group within the TIP for the invaluable conversations and insights into the industry-driven research activities in optical communications.

Finally, I would like to thank all my friends and loved ones for their unwavering support, especially my family, to whom I dedicate this thesis.

Abstract

This thesis focuses on improvements and development of analytical models and artificial intelligence (AI) implementation for optical network design, planning and controlling based on the physical-layer-aware quality of transmission (QoT) estimation.

In general, with the increasing demand for capacity and traffic, network operators have started to look toward innovative solutions that can maximize transmission speeds and capacities. In this perspective, open and disaggregated optical network infrastructures have been considered as they offer more flexibility and allow for a multi-vendor approach to be realized. In such frameworks, software-defined networking (SDN) can be used to implement optical network control and management with lightpaths (LPs) being assigned dynamically. A partially disaggregated optical network with a SDN approach to control and management, is composed of disaggregated re-configurable optical add-drop multiplexers (ROADMs) connected by independent optical line systems (OLSs) that include the degrees of the ROADM multiplexer/de-multiplexer, fibers, and amplifiers (booster, in-line and pre-amp). These OLSs transport colored wavelength division multiplexing (WDM) optical tributary signals from ROADM to ROADM upon transparent LPs, with each OLS independently orchestrated using the SDN controller. To achieve this, a quality of transmission estimator (QoT-E) is required to compute the generalized signal-to-noise ratio (GSNR) of transparent LPs to assess network performance before, after and during deployment. Operating under the assumption that LPs are additive white Gaussian noise (AWGN) channels, the GSNR includes the accumulations of both the amplified spontaneous emission (ASE) noise that arises from the amplifiers, and the nonlinear interference (NLI) noise that is induced by the fiber propagation, with the interaction between these two contributions being negligible in terrestrial networks. This approach has been extensively validated and can be refined including system margins that take into account additional impairments as the intrinsic transceiver

SNR, the polarization mode dispersion, the polarization dependent loss (PDL) and filtering penalties. By means of this assumption, any LP can be separated into the OLSs and switching nodes that are traversed during signal propagation; crucially, the total QoT may be calculated as the proper cumulative function of each QoT contribution arising from these subdomains.

In this framework, the open-source library for design and lightpath computation in real-world mesh optical networks, GNPy, has been implemented by the Physical Simulation Environment (PSE) group, within the Telecom Infra Project, which includes the major operators and vendors in the optical networking field. As a matter of fact, GNPy has gained an increasing interest for both academia and industry, representing an accurate, vendor-agnostic QoT-E used for network design and standards definition and for lightpath computation, paving the way towards a SDN planning and controlling. This broad interest in GNPy is due to the rising request in optical network communities of a reliable and efficient digital twin of the optical systems. As a stand alone software, GNPy is a digital model where information exchange with the real system is performed through structured input/output data in a manual manner. By mean of further improvements, an advanced software framework based on an enhanced digital model has been implemented, including a more precise and efficient physical layer signal propagation model, along with a faster and more flexible structure, to enable the simulation of new transmission technologies, dynamic application of automated AI, and heuristic methods for optimization and margin management in SDN environments. This software framework, has been validated on several experimental setups including cutting-edge transmission scenarios.

Additionally, the enhanced transmission modeling has been employed for investigating wideband optical systems as future looking network innovation that provides significant capacity gain on already installed network infrastructures, with limited and cost-effective system upgrades.

Contents

List of Figures

List of Tables

List of Abbreviations

ADC	Analog-to-Digital Converter
AI	Artificial Intelligence
API	Application programming interface
ASE	Amplified Spontaneous Emission
AWGN	Additive White and Gaussian Noise
B2B	Back-to-Back
BER	Bit Error Rate
CAPEX	Capital Expenditures
CD	Chromatic Dispersion
CPE	Carrier Phase Estimation
CUT	Channel Under Test
DAC	Digital-to-Analog Converter
DEMUX	De-Multiplexer
DGE	Dynamic Gain Equalizer
DNN	Deep Neural Network
DP	Dual-Polarization
DP-CNLSE	DP Coupled Nonlinear Schrodinger Equation
DSP	Digital Signal Processing
DT	Digital Twin
ECL	External Cavity Laser
EDFA	Erbium-Doped Fiber Amplifier

FEC	Forward Error Correction
FFT	Fast Fourier Transform
FWM	Four-Wave-Mixing
GA	Genetic Algorithm
GGN	Generalized Gaussian Noise
GN	Gaussian Noise
GNPy	Gaussian Noise Model in Python
GSNR	Generalized Signal-to-Noise Ratio
IB-IC	Inter-Band Inter-Channel
IETF	Internet Engineering Task Force
IMDD	Intensity Modulated and Direct Detection
IoT	Internet of Things
LCoS	Liquid-Crystal on Silicon
LMS	Least Mean Square
LOGO	Local-Optimization Global-Optimization
MBT	Multi-Band Transmission
ML	Machine Learning
MUX	Multiplexer
NLI	Nonlinear Interference
NOS	Network Operating System
OCM	Optical Channel Monitor
ODA	Observe-Decide-Act
OIF	Optical Internetworking Forum
OLS	Optical Line System
ONF	Open Networking Foundation
OPEX	Operational Expenditures
OSA	Optical Spectrum Analyzer
OSNR	Optical Signal-to-Noise Ratio
OT	Optical Terminal

OTDR	Optical Time Domain Reflectometer
PCS	Probabilistic Constellation Shaping
PDL	Polarization Dependent Loss
PM	Polarization Multiplexed
PMD	Polarization Mode Dispersion
PS	Polarization Scrambler
PSD	Power Spectral Density
PSE	Physical Simulation Environment
QAM	Quadrature Amplitude Modulation
QoT	Quality of Transmission
QoT-E	Quality of Transmission Estimator
QPSK	Quadrature Phase-Shift Keying
RMSE	Root Mean Square Error
ROADM	Reconfigurable Optical Add-Drop Multiplexer
SC	Single-Channel
SCM	Subcarriers Multiplexed
SDN	Software-Defined Networking
SLM	Spatial Light Modulator
SNR	Generalized Signal-to-Noise Ratio
SNR_{NL}	NonLinear Signal-to-Noise Ratio
SNR_{RX}	Receiver Signal-to-Noise Ratio
SNR_{TX}	Transmitter Signal-to-Noise Ratio
SOA	Semiconductor Optical Amplifier
SRS	Stimulated Raman Scattering
SSFM	Split-Step Fourier Method
SSMF	Standard Single-Mode Fiber
TDFA	Thulium-Doped Fiber Amplifier
TIP	Telecom Infra Project
TRX	Transceiver

VOA	Variable Optical Attenuator
WDM	Wavelength Division Multiplexing
WSS	Wavelength Selective Switch
XC	Cross-Channel

List of Symbols

a	Fiber Core Radius
α	Fiber Loss Coefficient
$\vec{A}_\mathrm{L}$	Linear Dual-Polarization Modal Amplitude
$\vec{A}_\mathrm{NL}$	Nonlinear Dual-Polarization Modal Amplitude
$\vec{A}$	Dual-Polarization Modal Amplitude
A_{eff}	Effective Mode Area
B_A	Optical Amplifier Bandwidth
β	Mode Propagation Constant
β_2	Second Derivative of β
C_∞	Asymptotic SC-NLI Accumulation Coefficient
$\vec{\varphi}_\lambda$	Channel Transmitted Modulated Signal
ρ_λ	Channel Power Gain/Loss Profile
B_λ	Channel Bandwidth
$R_{s,\lambda}$	Channel Symbol Rate
f_λ	Channel Central Frequency
$P_{\mathrm{NLI};\lambda}$	Channel NLI Noise Power
$P_{\mathrm{ASE};\lambda}$	Channel ASE Noise Power
P_λ	Channel Power
D	Chromatic Dispersion
n_c	Cladding Refractive Index
n_1	Core Refractive Index
$P_{\mathrm{XC},\lambda}$	XC NLI Noise Power
Δ_n	Relative Step Index Wavelength Coordinate

Λ	Effective Length
$\langle\cdots\rangle$	Expectation Value Operator
f_{ref}	Reference Frequency
f	Frequency Coordinate
G	Optical Amplifier Gain
γ	Fiber Nonlinear Coefficient
γ_R	Mode Intensity Raman Gain Coefficient
g_R	Raman Gain Coefficient
h	Plank Constant
$\imath$	Imaginary Unit
k_{pol}	Unitary Polarization Coefficient
λ_0	Zero Dispersion Wavelength Coordinate
$\mathscr{L}$	Linear Operator
l_c	Fiber Input Connector Loss
n_2	Nonlinear Kerr Parameter
NF	Noise Figure
B_N	Noise Bandwidth
η	Nonlinear Efficiency
$\mathscr{N}$	Nonlinear Operator
N_{ch}	Number of Channels
ΔOSNR	OSNR Variation
$\mathbf{P}$	Permutation Space
$\mathscr{G}$	Power Spectral Density Profile
R_b	Bit Rate

r_T	Optical Amplifier Tilt Ripple
R_s	Symbol Rate
S_0	Zero Dispersion Slope
$P_{\mathrm{SC},\lambda}$	SC NLI Noise Power
SNR_λ	Lightpath SNR
L_s	Span Length
c	Speed of Light
$\cdot$	Standard Product in the Bi-Dimensional Polarization Space
T	Optical Amplifier Tilt
t	Time Coordinate
τ	Tolerance
V	Normalized Frequency
w	Mode Radius
λ	Wavelength
z	Longitudinal Spatial Coordinate

List of Scientific Contributions

List of scientific contributions carried out during the PhD is here reported along with a list of activities and collaborations.

Peer-Reviewed Journals

1. A. Ferrari, A. Napoli, J. K. Fischer, N. Costa, A. D'Amico, J. Pedro, W. Forysiak, E. Pincemin, A. Lord, A. Stavdas, J. P. F.-P. Gimenez, G. Roelkens, N. Calabretta, S. Abrate, B. Sommerkorn-Krombholz, and V. Curri. "Assessment on the Achievable Throughput of Multi-Band ITU-T G.652.D Fiber Transmission Systems". In: Journal of Lightwave Technology 38.16 (2020), pp. 4279–4291. DOI: 10.1109/JLT.2020.2989620.
2. A. D'Amico, S. Straullu, A. Nespola, I. Khan, E. London, E. Virgillito, S. Piciaccia, A. Tanzi, G. Galimberti, and V. Curri. "Using machine learning in an open optical line system controller". In: J. Opt. Commun. Netw. 12.6 (June 2020), pp. C1–C11. DOI: 10.1364/JOCN.382557.
3. E. Virgillito, A. Ferrari, A. D'Amico, and V. Curri. "Statistical Assessment of Open Optical Networks". In: Photonics 6.2 (2019). ISSN: 2304-6732. DOI: 10.3390/photonics6020064.
4. E. London, E. Virgillito, A. D'Amico, A. Napoli, and V. Curri. "Simulative assessment of non-linear interference generation within disaggregated optical line systems". In: OSA Continuum 3.12 (Dec. 2020), pp. 3378–3389. DOI: 10.1364/OSAC.410333.

5. I. Khan, M. Bilal, M. U. Masood, A. D'Amico, and V. Curri. "Lightpath QoT computation in optical networks assisted by transfer learning". In: J. Opt. Commun. Netw. 13.4 (Apr. 2021), B72–B82. DOI: 10.1364/JOCN.409538.
6. A. D'Amico, S. Straullu, G. Borraccini, E. London, S. Bottacchi, S. Piciaccia, A. Tanzi, A. Nespola, G. Galimberti, S. Swail, and V. Curri. "Enhancing Lightpath QoT Computation With Machine Learning in Partially Disaggregated Optical Networks". In: IEEE Open Journal of the Communications Society 2 (2021), pp. 564–574. DOI: 10.1109/OJCOMS.2021.3066913.
7. G. Borraccini, A. D'Amico, S. Straullu, A. Nespola, S. Piciaccia, A. Tanzi, G. Galimberti, S. Bottacchi, S. Swail, and V. Curri. "Cognitive and autonomous QoT-driven optical line controller". In: J. Opt. Commun. Netw. 13.10 (Oct. 2021), E23–E31. DOI: 10.1364/JOCN.424021.
8. A. D'Amico, E. London, B. L. Guyader, F. Frank, E. L. Rouzic, E. Pincemin, N. Brochier, and V. Curri. "Experimental validation of GNPy in a multi-vendor flex-grid flex-rate WDM optical transport scenario". In: J. Opt. Commun. Netw. 14.3 (Mar. 2022), pp. 79–88. DOI: 10.1364/JOCN.442208.
9. E. London, A. D'Amico, E. Virgillito, A. Napoli, and V. Curri. "Modelling non-linear interference in non-periodic and disaggregated optical network segments". In: Opt. Continuum 1.4 (Apr. 2022), pp. 793–803. DOI: 10.1364/OPTCON.453253.
10. A. D'Amico, B. Correia, E. London, E. Virgillito, G. Borraccini, A. Napoli, and V. Curri. "Scalable and Disaggregated GGN Approximation Applied to a C+L+S Optical Network". In: Journal of Lightwave Technology (2022), pp. 1–1. DOI: 10.1109/JLT.2022.3162134.
11. G. Borraccini, A. D'Amico, S. Straullu, F. Usmani, A. Ahmad, and V. Curri. "Iterative supervised learning approach using transceiver bit-error-rate measurements for optical line system optimization". In: J. Opt. Commun. Netw. 15.2 (Feb. 2023), pp. 111–118.
DOI: 10.1364/JOCN.475460.
12. G. Borraccini, S. Straullu, A. Giorgetti, R. Ambrosone, E. Virgillito, A. D'Amico, R. D'Ingillo, F. Aquilino, A. Nespola, N. Sambo, F. Cugini, and V.

Curri. “Experimental Demonstration of Partially Disaggregated Optical Network Control Using the Physical Layer Digital Twin”. In: IEEE Transactions on Network and Service Management, pp. 1-1. DOI: 10.1109/TNSM.2023.3288823.

13. E. Virgillito, A. Castoldi, A. D’Amico, S. Straullu, A. Bovio, R. Pastorelli, and V. Curri, "Spatially disaggregated model for self-channel interference in mixed fiber optical network segments," J. Opt. Commun. Netw. 15, C271-C287 (2023) DOI: 10.1364/JOCN.486713.

Contributions to International Conferences

1. E. Virgillito, A. D’Amico, A. Ferrari, and V. Curri. “Observing and Modeling Wideband Generation of Non-Linear Interference”. In: 2019 21st International Conference on Transparent Optical Networks (ICTON). 2019, pp. 1–4. DOI: 10.1109/ICTON.2019.8840528.

2. A. M. R. Brusin, U. C. de Moura, A. D’Amico, V. Curri, D. Zibar, and A. Carena. “Load Aware Raman Gain Profile Prediction in Dynamic Multi-Band Optical Networks”. In: 2020 Optical Fiber Communications Conference and Exhibition (OFC). 2020, pp. 1–3. T4B.3

3. A. D’Amico, E. London, E. Virgillito, A. Napoli, and V. Curri. “Quality of Transmission Estimation for Planning of Disaggregated Optical Networks”. In: 2020 International Conference on Optical Network Design and Modeling (ONDM). 2020, pp. 1–3. DOI: 10.23919/ONDM48393.2020.9133012.

4. A. D’Amico, S. Straullu, A. Nespola, I. Khan, S. Abdelfattah, E. Virgillito, S. Piciaccia, A. Tanzi, G. Galimberti, S. Abrate, and V. Curri. “Machine-learning aided OSNR prediction in optical line systems”. In: 45th European Conference on Optical Communication (ECOC 2019). 2019, pp. 1–4. DOI: 10.1049/cp.2019.0758.

5. G. Borraccini, A. Ferrari, S. Straullu, A. Nespola, A. D’Amico, S. Piciaccia, G. Galimberti, A. Tanzi, S. Turolla, and V. Curri. “Softwarized and Autonomous Raman Amplifiers in Multi-Band Open Optical Networks”. In: 2020 International Conference on Optical Network Design and Modeling (ONDM). 2020, pp. 1–6. DOI: 10.23919/ONDM48393.2020.9133036.

6. A. Ferrari, J. Kundrát, E. L. Rouzic, M. Filer, A. Campanella, A. D'Amico, K. Balasubramanian, Y. Yin, O. Havliš, M. Hažlinský, J. Vojtˇech, J. -L. Augé, G. Grammel, G. Galimberti, and V. Curri. "The GNPy Open Source Library of Applications for Software Abstraction of WDM Data Transport in Open Optical Networks". In: 2020 6th IEEE Conference on Network Softwarization (NetSoft). 2020, pp. 386–394. DOI: 10.1109/NetSoft48620.2020.9165313.

7. G. Borraccini, S. Straullu, A. D'Amico, A. Nespola, S. Piciaccia, A. Tanzi, G. Galimberti, and V. Curri. "Autonomous Physical Layer Characterization in Cognitive Optical Line Systems". In: 2021 Optical Fiber Communications Conference and Exhibition (OFC). 2021, pp. 1–3. M3C.4.

8. V. Curri, A. D'Amico, and S. Straullu. "Synergetical Use of Analytical Models and Machine-Learning for Data Transport Abstraction in Open Optical Networks". In: 2019 21st International Conference on Transparent Optical Networks (ICTON). 2019, pp. 1–4. DOI: 10.1109/ICTON.2019.8840219.

9. E. Virgillito, A. Castoldi, A. D'Amico, S. Straullu, S. Abrate, R. Pastorelli, and V. Curri. "Propagation Effects in Mixed 10G-100G Dispersion Managed Optical Links". In: 2019 21st International Conference on Transparent Optical Networks (ICTON). 2019, pp. 1–4. DOI: 10.1109/ICTON.2019.8840162.

10. A. D'Amico, E. London, E. Virgillito, A. Napoli, and V. Curri. "Inter-Band GSNR Degradations and Leading Impairments in C+L Band 400G Transmission". In: 2021 International Conference on Optical Network Design and Modeling (ONDM). 2021, pp. 1–3. DOI: 10.23919/ONDM51796.2021.9492485.

11. E. Virgillito, E. London, A. D'Amico, B. Correia, A. Napoli, and V. Curri. "Single- vs. Multi-Band Optimized Power Control in C+L WDM 400G Line Systems". In: 2021 Optical Fiber Communications Conference and Exhibition (OFC). 2021, pp. 1–3. Th4C.3.

12. J. Kundrát, E. L. Rouzic, J. Mårtensson, A. Campanella, O. Havliš, A. D'Amico, G. Grammel, G. Galimberti, V. Curri, and J. Vojtˇech. "GNPy & YANG: Open APIs for End-to-End Service Provisioning in Optical Networks". In: Optical Fiber Communication Conference (OFC) 2021. Optical Society of America, 2021. M1B.6.

13. A. D’Amico, E. London, B. L. Guyader, F. Frank, E. L. Rouzic, E. Pincemin, N. Brochier, and V. Curri. “GNPy experimental validation on flex-grid, flex-rate WDM optical transport scenarios”. In: Optical Fiber Communication Conference (OFC) 2021. Optical Society of America, 2021. W1G.2.
14. G. Borraccini, S. Straullu, A. D’Amico, E. Virgillito, L. Kumar, S. Piciaccia, S. Bottacchi, S. Swail, G. Galimberti, and V. Curri. “QoT-E Driven Optimized Amplifier Control in Disaggregated Optical Networks”. In: Optical Fiber Communication Conference (OFC) 2021. Optical Society of America, 2021. M3E.6.
15. M. S. Raza, A. D’Amico, F. Usmani, S. M. Alavi, M. A. Taimoor, V. Curri, and A. Ahmad. “LYNX: A GNPy-based web application for multi-vendor optical network planning”. In: Optical Fiber Communication Conference (OFC) 2022. Optica Publishing Group, 2022. M3Z.13.
16. A. D’Amico, L. Guyader, F. Frank, E. Le Rouzic, E. Pincemin, A. Napoli, H. Sun, B. Spinnler, N. Brochier, and V. Curri. “GNPy Experimental Validation for Nyquist Subcarriers Flexible Transmission up to 800 G”. In: 2022 Optical Fiber Communications Conference and Exhibition (OFC). 2022, pp. 1–3. M4F.6.
17. G. Borraccini, S. Straullu, A. Giorgetti, R. D’Ingillo, D. Scano, A. D’Amico, E. Virgillito, A. Nespola, N. Sambo, F. Cugini, and V. Curri. “QoT-Driven Optical Control and Data Plane in Multi-Vendor Disaggregated Networks”. In: Optical Fiber Communication Conference (OFC) 2022. Optica Publishing Group, 2022, M4F.5. DOI: 10.1364/OFC.2022.M4F.5.
18. A. D’Amico, E. London, B. L. Guyader, F. Frank, E. L. Rouzic, E. Pincemin, N. Brochier, and V. Curri. “Experimental validation of GNPy in a multi-vendor flex-grid flex-rate WDM optical transport scenario”. In: J. Opt. Commun. Netw. 14.3 (Mar. 2022), pp. 79–88. DOI: 10.1364/JOCN.442208.
19. E. London, E. Virgillito, A. D’Amico, A. Napoli, and V. Curri. “Observing cross-channel NLI generation in disaggregated optical line systems”. In: Asia Communications and Photonics Conference 2021. Optica Publishing Group, List of Contributions to International Conferences xix 2021, W3B.3. DOI: 10.1364/ACPC.2021.W3B.3.

20. T. Mano, A. D'Amico, E. Virgillito, G. Borraccini, Y. -K. Huang, K. Kitamura, K. Anazawa, A. Masuda, H. Nishizawa, T. Wang, K. Asahi, and V. Curri. "Accuracy of Nonlinear Interference Estimation on Launch Power Optimization in Short-Reach Systems with Field Trial". In: 2022 European Conference on Optical Communication (ECOC). 2022, pp. 1–4. We3B.1.

21. J. Kundrát, E. L. Rouzic, J. Mårtensson, S. Melin, A. D'Amico, G. Grammel, G. Galimberti, and V. Curri. "GNPy: Lessons Learned and Future Plans [Invited]". In: European Conference on Optical Communication (ECOC) 2022. Optica Publishing Group, 2022, We3B.6.

22. E. Virgillito, A. Castoldi, A. D'Amico, S. Straullu, R. Bratovich, F. M. Rodriguez, A. Bovio, R. Pastorelli, and V. Curri. "Spatially Disaggregated Modelling of Self-Channel NLI in Mixed Fibers Optical Transmission". In: 2022 European Conference on Optical Communication (ECOC). 2022, pp. 1–4. Tu5.32.

23. R. Bratovich, F. M. R., S. Straullu, E. Virgillito, A. Castoldi, A. D'Amico, F. Aquilino, R. Pastorelli, and V. Curri. "Surveillance of Metropolitan Anthropic Activities by WDM 10G Optical Data Channels". In: 2022 European Conference on Optical Communication (ECOC). 2022, pp. 1–4. Tu3B.6.

24. S. Straullu, F. Aquilino, R. Bratovich, F. M. Rodriguez, A. D'Amico, E. Virgillito, R. Pastorelli, and V. Curri. "Real-time Detection of Anthropic Events by 10G Channels in Metro Network Segments". In: 2022 IEEE Photonics Conference (IPC). 2022, pp. 1–2. DOI: 10.1109/IPC53466.2022.9975561.

25. M. Devigili, P. N. Goki, N. Sambo, P. Castoldi, L. Potì, A. D'Amico, and V. Curri. "Multi-band Optical Network Assisted by GNPy: an Experimental Demonstration". In: 2022 IEEE Latin-American Conference on Communications (LATINCOM). 2022, pp. 1–5. DOI: 10.1109/LATINCOM56090.2022.10000774.

26. A. D'Amico, B. L. Guyader, F. Frank, E. L. Rouzic, E. Pincemin, N. Brochier, and V. Curri. "An Experimental Observation of the Disaggregated Nonlinear Interference Noise Generation". In: 2022 Asia Communications and Photonics Conference (ACP). 2022, pp. 530–533. DOI: 10.1109/ACP55869.2022.10088915.

27. A. D'Amico, G. Borraccini, S. Straullu, F. Aquilino, S. Piciaccia, A. Tanzi, G. Galimberti, and V. Curri. "Statistical Analysis of PDL Penalty on Coherent Transmission Technologies Based on WSS Experimental Characterization". In: 2022 Asia Communications and Photonics Conference (ACP). 2022, pp. 874–877. DOI: 10.1109/ACP55869.2022.10088670.

28. E. Virgillito, A. Castoldi, A. D'Amico, S. Straullu, R. Bratovich, F. M. Rodriguez, A. Bovio, R. Pastorelli, and V. Curri. "Disaggregated SCI Estimation for QoT-E in Mixed Fibers Network Segments". In: Optical Fiber Communication Conference (OFC) 2023. Optica Publishing Group, 2023, Th2A.29.

29. A. D'Amico, G. Borraccini, S. Straullu, F. Aquilino, S. Piciaccia, A. Tanzi, G. Galimberti, and V. Curri. "Experimental Probing and Modeling of the PDL Impact on the Optical Signal-to-Noise Ratio". In: Optical Fiber Communication Conference (OFC) 2023. Optica Publishing Group, 2023, W1E.6.

30. G. Borraccini, R. Ambrosone, A. Giorgetti, S. Straullu, F. Aquilino, E. Virgillito, A. D'Amico, R. D'Ingillo, N. Sambo, F. Cugini, and V. Curri. "Disaggregated Optical Network Orchestration based on the Physical Layer Digital Twin". In: Optical Fiber Communication Conference (OFC) 2023. Optica ublishing Group, 2023. Tu3D.4.

31. F. Usmani, A. D'Amico, R. Bratovich, F. M. Rodriguez, S. Straullu, E. Virgillito, F. Aquilino, R. Pastorelli and V. Curri. "Road Traffic Detection with a LSTM Autoencoder using State of Polarization on Deployed Metropolitan Fiber Cable". In: 2023 International Conference on Optical Network Design and Modeling (ONDM).

32. T. Mano, A. D'Amico, E. Virgillito, G. Borraccini, Y. -K. Huang, K. Anazawa, H. Nishizawa, T. Wang, K. Asahi, and V. Curri. "Modeling Transceiver BER-OSNR Characteristic for QoT Estimation in Short-Reach Systems". In: 2023 International Conference on Optical Network Design and Modeling (ONDM).

33. G. Borraccini, A. D'Amico, S. Straullu, F. Aquilino, S. Piciaccia, A. Tanzi, G. Galimberti, and V. Curri. "Local vs. Global Optimization for Optical Line System Control in Disaggregated Networks". In: 2023 International Conference on Optical Network Design and Modeling (ONDM).

34. E. Virgillito, S. Straullu, F. Aquilino, R. Bratovich, H. Awad, R. Proietti, A. D’Amico, R. Pastorelli, and V. Curri. “Detection, Localization and Emulation of Environmental Activities Using SOP Monitoring of IMDD Optical Data Channels”. In: 2023 23rd International Conference on Transparent Optical Networks (ICTON). DOI: 10.1109/ICTON59386.2023.10207513.

35. R. Ambrosone, R. D’Ingillo, G. Borraccini, S. Straullu, A. D’Amico, E. Virgillito, A. Giorgetti, and V. Curri. “Autonomous Equalization of Independent Open ROADMs via NETCONF Protocol”. In: 2023 23rd International Conference on Transparent Optical Networks (ICTON). DOI: 10.1109/ICTON59386.2023.10207261.

36. E. London, E. Virgillito, A. D’Amico and V. Curri. “Observing Disaggregated Cross-Channel NLI Generation in Dispersion-Managed Links”. In: 2023 23rd International Conference on Transparent Optical Networks (ICTON). DOI: 10.1109/ICTON59386.2023.10207225.

Activities and Collaborations

- Collaboration with Cisco Photonics on optical transmission simulations - 2019/ongoing
- Collaboration with the Physical Simulation Environment group of the Telecom Infra Project on the development and validation of GNPy: a vendor-agnostic QoT estimator - 2019/ongoing
- Collaboration with Orange for GNPy experimental validation campaigns - 2021/2022
- Collaboration with SM Optics on fiber sensing in optical networks - 2022/ongoing
- Collaboration with NTT and NEC Labs America on GNPy validation on short reach and greenfield transmission scenarios - 2021/ongoing
- Internship at NEC Labs America within the Optical Networking and Sensing group - Summer 2022.

Chapter 1

Introduction

Optical networks are critical infrastructures for modern communications, enabling the transmission of vast amounts of data over long distances with high speed and reliability. These networks use optical fiber as the medium to carry information through light pulses, and have revolutionized the way we communicate and access information. As internet traffic continues to grow due to the proliferation of connected devices, the increasing popularity of data-intensive applications such as streaming video, cloud computing, and the internet of things (IoT), and the upcoming wide deployment of 5G networking [1], optical networks are expected to cope with this ever-increasing demand for data traffic. In this perspective, both optical network operators and vendors are in constant search of infrastructure improvement and technology innovation for minimizing the capital expenditures (CAPEX) and maintaining a limited operational expenditures (OPEX), essential requirements to achieve an adequate level of revenues and avoid the so called "fiber capacity crunch". In general, increasing capacity with minimal CAPEX corresponds to maximizing the usage of already-deployed fiber, as new fiber deployment is typically a prohibitively expensive procedure [2].

The development of fast digital-to-analog converter (DAC) and analog-to-digital converter (ADC) and energy efficient electronic processors implementing digital signal processing (DSP) based algorithms has enabled a significant improvement of optical network capacity with the proliferation of coherent transceivers (TRXs) [3, 4], currently the prevalent transmission technologies in long-haul and high-capacity optical infrastructure. Unlike Intensity Modulated and Direct Detection (IMDD) transmission, which requires chromatic dispersion (CD) compensation after each fiber span and is limited by accumulated polarization mode dispersion (PMD), coherent transmission enables the compensation of such linear propagation impairments to be performed at the receiver side [5–8]. This essential improvement, which involves decoupling the optical terminals (OTs)s from the optical line systems (OLSs)s, has ushered in a new era of flexibility and efficiency in optical networks and operators have gained unprecedented control and adaptability in managing their network resources. In this perspective, coherent transmission has complemented the implementation of reconfigurable optical add-drop multiplexers (ROADMs). These devices allow for dynamic and remote-controlled deployment of lightpaths, adding an extra layer of agility to the optical network [9]. With ROADMs, operators can remotely control the routing and switching of wavelengths, enabling on-demand provisioning and reconfiguration of optical connections. The ability to deploy dynamic and remote-controlled lightpaths brings several benefits to optical networks. Firstly, it allows for efficient resource utilization by enabling the establishment of temporary connections when and where needed. This flexibility is particularly valuable in scenarios where bandwidth demands fluctuate over time or in response to specific events or applications. Moreover, the remote control capability offered by ROADMs simplifies network management and maintenance. Operators can remotely monitor and adjust the routing of wavelengths, eliminating the need for manual interventions at physical network nodes. This not only reduces operational costs but also minimizes service disruptions and downtime associated with traditional manual reconfigurations.

1.1 Software-Defined, Open and Disaggregated Optical Networks

As optical networks are evolving to meet the increasing demands for capacity, flexibility, and cost-efficiency, the concepts of software-defined, open and disaggregated networking is gaining prominence [10–15]. Software-Defined networking (SDN) involves separating the control plane from the data plane, enabling an independent development, deployment, and management of each network layer and a hierarchical architecture that provides abstraction, programmability and scalability of the network infrastructure. Openness and disaggregation emphasizes interoperability, standard-

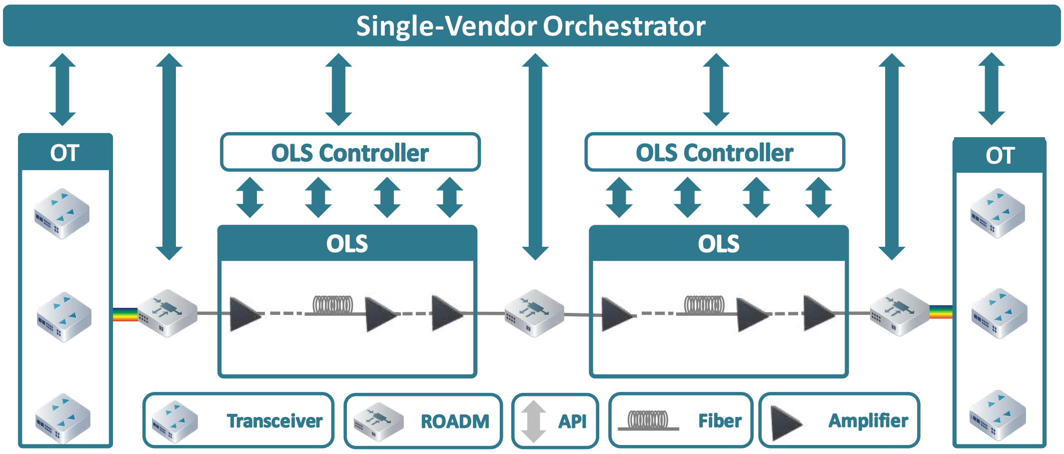

Fig. 1.1 Single-vendor fully aggregated network architecture controlled and managed with proprietary software and functionalities.

ization, and collaboration among vendors and stakeholders, standing in contrast to a fully aggregated network architecture, illustrated in Fig. 1.1, where a single vendor deploys the entire infrastructure and managed it using proprietary software and functionalities in a closed manner.

Leveraging the decoupling OTs from OLSs enabled by coherent transmission and ROADMs deployment, a large scale implementation of partially disaggregated architecture is the current objective of major network operators. As a matter of fact, a fully disaggregated scenario, where the entire network can be composed of a multi-vendor heterogeneous set of independently controlled components, is not currently feasible or likely in the foreseeable future in large scale network infrastructures, primarily due to efficiency limitations in terms of performance and power consumption. Nevertheless, an open and partially disaggregated software-defined networking (SDN), represented in Fig. 1.2, has revolutionized the optical networking landscape by providing operators with greater control, agility, and scalability enabling operators to deploy and integrate multi-domain network infrastructures with OTs and OLSs from different vendors. This paradigm shift in network architecture offers opportunities for advanced network orchestration, dynamic resource allocation, and the development of new services that can meet the evolving demands of the digital era. Moreover, it reduces vendor lock-in and promoting vendor diversity leading to increased competition, innovation, and cost efficiency. Operators can select the best possible hardware components and software solutions that suit their specific requirements. In particular, open and partially disaggregated SDN has found

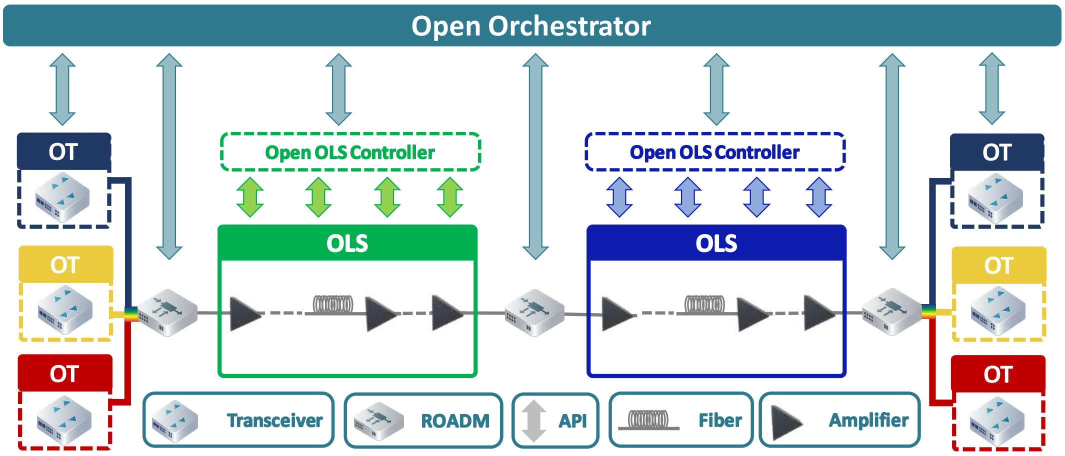

Fig. 1.2 Multi-vendor, multi-domain partially disaggregated network architecture controlled and managed with open APIs and NOS. Different colors represent distinct vendor domains and dashed line boxed open interfaces.

practical applications in optical communication in the framework of network virtualization, where operators can create virtual network slices with specific performance characteristics to support different services and applications, as path computation and failure recovery, along with an optimized network planning and design. Furthermore, open and partially disaggregated SDN enables efficient resource sharing and the provisioning of services tailored to specific customer requirements. Another use case is traffic engineering, where the central network orchestrator can dynamically steer traffic flows to optimize network utilization. Even more, progress towards a robust and reliable open and partially disaggregated SDN solution in optical networks is an ongoing process with constant advancements in technologies and industry collaborations. Future developments include the integration of artificial intelligence (AI) and machine learning (ML) techniques to enhance network automation, optimization, and predictive maintenance.

While open and partially disaggregated SDN brings numerous benefits, it also poses challenges in terms of control, deployment and management. Ensuring compatibility and interoperability between different vendor solutions is a fundamental and non trivial requirement for such a paradigm implementation. Additionally, security considerations are paramount, as the use of open interfaces and software increases the potential attack surface or they may require sensitive information sharing between different vendors. Robust security mechanisms, such as authentication, encryption, and intrusion detection, must be implemented to protect network infrastructure and data.

In this perspective, the industry is exploring the potential of open source software and white-box hardware solutions to further drive vendor neutrality, interoperability, and innovation [16, 14]. Several organizations and initiatives are committed to advancing the development and adoption of open optical networking, such as Internet Engineering Task Force (IETF) [17], Open Networking Foundation (ONF) [18], Optical Internetworking Forum (OIF) [19], OpenROADM [20], OpenConfig [21], and Telecom Infra Project (TIP) [22]. These organizations and working groups play a crucial role in standardization defining common application programming interfaces (APIs)s, network operating systems (NOSs)s and data models for seamless integration, as well as in interoperability defining operational specifications and communal use cases[23, 24].

1.2 Physical Layer Aware Networking

As optical networks become more interconnected and span multiple domains, a federated and adaptable approach becomes essential. Efficient mechanisms for orchestrating and managing resources across different administrative domains need to be developed for inter-domain routing, resource discovery, and policy enforcement mechanisms enabling seamless and secure interconnection between disparate optical network domains. In this perspective, the notion of optical network digital twin (DT) is increasingly gaining traction [25–27]. In general, in a DT concept involves creating a digital model as a virtual replica of the physical system, including its components, connections, and operational characteristics, and a mutual automatic data flow mechanism between the two objects enabling continuous synchronization and real-time updates. Such a framework allows network operators to gain deeper insights into the optical infrastructure behavior, anticipate potential issues, perform effective planning and design, and optimize transmission performance. Moreover, optical network DT enables the implementation of advanced analytics and machine.

In this thesis work, Gaussian noise model in Python (GNPy) has been considered as one of the most promising digital models of optical systems. GNPy is an open-source library that facilitates the development of route planning and optimization tools specifically designed for multi-vendor optical networks in real-world scenarios and is developed and maintained by the Physical Simulation Environment working group, within the TIP Open Optical & Packet Transport project, as a collaborative initiative involving esteemed partners like Orange, Microsoft, Telia Carrier, Cisco, Juniper, Politecnico di Torino, and Meta [28]. Some of the analysis presented in this manuscript represent GNPy validations and software improvements as results of an intensive and prolific collaboration with other Physical Simulation Environment (PSE) and , in general, TIP participating companies. Regarding the data exchange between the digital and physical models, the current version of GNPy receive a static snapshot of the network status through structured input/output data. In particular, the input data structure of GNPy encompasses information such as the network topology description, network element characterization and configurations, as well as the desired design targets. Indeed, the accuracy of the digital model is significantly influenced by the quality of information provided for the virtual representation of the physical model. In order to implement a efficient, robust and reliable DT implementation, the data pipeline defining the automatic flow mechanism has to be implemented in the open and disaggregated SDN paradigm, leveraging the common open API, standardized data structures and network information obtained through diverse telemetry equipment. In the scope of this thesis, customized software framework solutions have been devised to cater to specific use cases to provide an enhanced implementation of GNPy with data of varying levels of accuracy.

In general, an optical network digital model must accurately and reliably estimate the Quality of Transmission (QoT) of a transparent lightpath connecting source and destination nodes in a coherent wavelength division multiplexing (WDM) transmission scenario [29–31]. In this transmission scenario, every lightpath can be approximated as an additive white and Gaussian noise (AWGN) channel and the generalized signal-to-noise ratio (GSNR) can be considered as QoT metric [32, 15], including all the generalized signal-to-noise ratio (SNR) impairments due to the signal transmission. The overall lightpath SNR of a given channel λ, SNR_λ, can be obtained considering the transmission GSNR, the transmitter signal-to-noise ratio (SNR_{TX}) and the receiver signal-to-noise ratio (SNR_{RX}):

$$\text{SNR}_\lambda = \left(\frac{1}{\text{SNR}_{\text{TX};\lambda}} + \frac{1}{\text{GSNR}_\lambda} + \frac{1}{\text{SNR}_{\text{RX};\lambda}} \right)^{-1}. \tag{1.1}$$

This quantity provides an accurate evaluation of the expected *pre*-forward error correction (FEC) bit error rate (BER), which is crucial for assessing lightpath feasibility and serves as unique figure of merit of network control, planning and optimization [33–35].

Additionally, by means of the AWGN assumption, the transmission GSNR can be expressed by properly combining the SNR degradations induced by the propagation through each independent OLS crossed by the lightpath [36]:

$$\mathrm{GSNR}_{\lambda} = \left(\sum_{n}^{N} \frac{1}{\mathrm{GSNR}_{\lambda}^{(n)}} \right)^{-1}, \tag{1.2}$$

where N is the total number of crossed OLSs, $n = 1, \cdots, N$, and $\mathrm{GSNR}_{\lambda}^{(n)}$ is the GSNR degradation on the channel λ introduced by the transmission through the n-th OLS. Consequently, the AWGN abstraction is perfectly aligned with the open and partially disaggregated SDN paradigm and allows for a separate optimization of each OLS within the network infrastructure. However, in realistic network implementations the deterministic SNR_{λ} value is not the unique factor contributing to overall transmission performance. This is due to the statistical nature of certain transmission phenomena like the polarization dependent loss (PDL), and device-specific thresholds such as the accumulated PMD and CD limitations of the DSP compensation. Therefore, a comprehensive the digital model must take into account supplementary metrics in order to evaluate additional SNR penalties and transmission limitation, ensuring a reliable reference including system margins [37].

Finally, the AWGN assumption implies a further decomposition of the single-OLS GSNR degradation on the channel λ, encompassing both the optical signal-to-

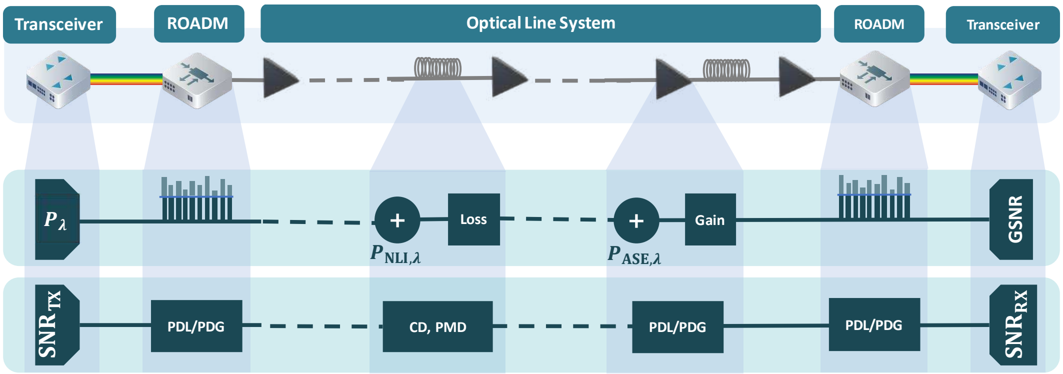

Fig. 1.3 Schematic of a comprehensive digital models able to evaluate the transmission GSNR and additional SNR penalties.

noise ratio (OSNR) and nonlinear signal-to-noise ratio (SNR $_{\mathrm{NL}}$):

$$\mathrm{GSNR}_{\lambda} = \left(\frac{1}{\mathrm{OSNR}_{\lambda}} + \frac{1}{\mathrm{SNR}_{\mathrm{NL};\lambda}}\right)^{-1} = \left(\frac{P_{\mathrm{ASE};\lambda}}{P_{\lambda}} + \frac{P_{\mathrm{NLI};\lambda}}{P_{\lambda}}\right)^{-1} . \tag{1.3}$$

Here, P_{λ} represents the channel power, whereas, $P_{\mathrm{ASE};\lambda}$ and $P_{\mathrm{NLI};\lambda}$ represent the total amounts of noise due to, respectively, the amplified spontaneous emission (ASE) generated by the optical amplifiers, and the nonlinear interference (NLI) due to the fiber Kerr effect [38]. A schematic of the comprehensive digital model considered in the scope of this thesis work is shown in Fig. 1.3.

1.3 Outline of the Remainder of this Thesis

This thesis work includes novel and effective analytical models and AI solutions for open and partially disaggregated SDN.

Chapter 2 presents an extensive physical layer modeling formulation for each network element. An efficient and precise approximation of the generalized Gaussian noise (GGN) model as a fast solution for multi-band transmission scenarios is proposed. Moreover, a perturbative solution of the stimulated Raman scattering (SRS) that offers an explicit formulation of higher order terms in the SRS-induced power transfer is defined. The chapter also discusses in details the PDL effect with a statistical approach.

Chapter 3 demonstrates the enhanced implementation of GNPy, based on the proposed transmission models, which is experimentally validated in a 20-span testbed installed at Orange Labs. GNPy shows significant accuracy on a flex-grid, flex-rate transmission scenario up to 800 Gbps, including Nyquist multi-subcarrier TRX. In the chapter a validation of the disaggregated implementation of GNPy is presented, along with validations of a statistical approach to the PDL effect.

In Chapter 4, the proposed digital model is validated using extensive simulation campaigns based on the split-step Fourier method (SSFM) and the numerical solution of the SRS. In this chapter a model-driven approach is proposed for the optimization of multi-band transmission problems, achieving highly satisfactory results through a fast and descriptive extension of the local-optimization global-optimization (LOGO).

Finally, in Chapter. 5, two ML solutions are proposed and experimentally validated for a variable spectral load transmission scenario, where a deep neural network (DNN) implementation provides very accurate prediction of signal and ASE noise power fluctuations induced by the erbium-doped fiber amplifier (EDFA) behavior in partially loaded transmission scenarios.

Chapter 2

Physical Layer Model

This chapter offers a comprehensive and in-depth depiction of the physical layer characteristics for every optical network element. The focus is on exploring analytical, numerical, and statistical methodologies with the goal of achieving efficient and accurate modeling of the optical transmission. The aim is to provide detailed insights into the intricate nature of the physical layer, enabling a thorough understanding of the optical network behavior.

2.1 Optical Transceiver

Within this manuscript, each WDM spectrum is defined as a collection of multiplexed channels that are transmitted or received by DSP-based coherent TRXs, employing polarization multiplexed quadrature amplitude modulation (QAM) formats. Each channel is characterized by a certain central frequency, f_λ, power, P_λ, symbol rate, $R_{s,\lambda}$, slot width, roll-off and modulation format.

As discussed in Sec. 1.2, SNR_λ serves as an estimation of the pre-FEC BER that has to be below a certain threshold to ensure an error-free digital stream after the FEC. Fig. 2.1(a) illustrates three distinct SNR-to-BER conversion functions for different modulation formats: quadrature phase-shift keying (QPSK), 8-QAM and 16-QAM. Establishing the lightpath feasibility results in a trade-off between the achievable capacity and required SNR_λ.

Conversely, the BER-to-SNR conversion functions play a crucial role in experimental validations of SNR prediction methodologies, as shown in Fig. 2.1(b), giving an accurate measurement of the total channel noise. Furthermore, a precise BER-to-SNR conversion function results in a telemetry means leveraging BER measurements that are readily accessible at the TRX side, and reducing the need for additional specialized equipment or monitoring devices. Generally, the SNR-to-BER conversion function can be obtain by means of the following expression [39, 40]:

$$\mathrm{BER} = k_1 \mathrm{erfc}\left(\sqrt{k_2 \mathrm{SNR}}\right), \tag{2.1}$$

where k_1 and k_2 are two modulation-format-dependent parameters,

$$\begin{aligned}
\mathrm{QPSK} &\equiv \left\{k_1 = k_2 = \frac{1}{2}\right\}, \\
8-\mathrm{QAM} &\equiv \left\{k_1 = \frac{2}{3}, k_2 = \frac{3}{14}\right\}, \\
16-\mathrm{QAM} &\equiv \left\{k_1 = \frac{3}{8}, k_2 = \frac{1}{10}\right\}.
\end{aligned}$$

When $\mathrm{SNR}_{\mathrm{TX}}$ and $\mathrm{SNR}_{\mathrm{RX}}$ are unknown, their joint contribution to SNR_λ can be evaluated with a back-to-back (B2B) characterization [41–43], measuring the BER variation induced by a controlled ASE noise loading. It is worth noting that in order to obtain an accurate measurement that can be used in a WDM spectrum transmission scenario, the B2B characterization must be performed transmitting the channel under test (CUT) with the two neighboring channels, one for each side. Fig.2.1(c) shows the results of the B2B characterization applied to several commercial TRXs, including different values of R_s and modulation format, along with the base SNR-to-BER evaluated curves obtained applying Eq. 2.1 to the bare OSNR variation, ΔOSNR, induced by the controlled ASE noise loading:

$$\mathrm{BER} = k_1 \mathrm{erfc}\left(\sqrt{k_2 \Delta\mathrm{OSNR}}\right). \tag{2.2}$$

It can be deduced that the mismatch between the measured and evaluated SNR-to-BER curves is exactly produced by the joint $\mathrm{SNR}_{\mathrm{TX}}$ and $\mathrm{SNR}_{\mathrm{RX}}$ contribution to SNR_λ, which can be evaluated fitting the measured B2B curve with Eq. 2.1 and

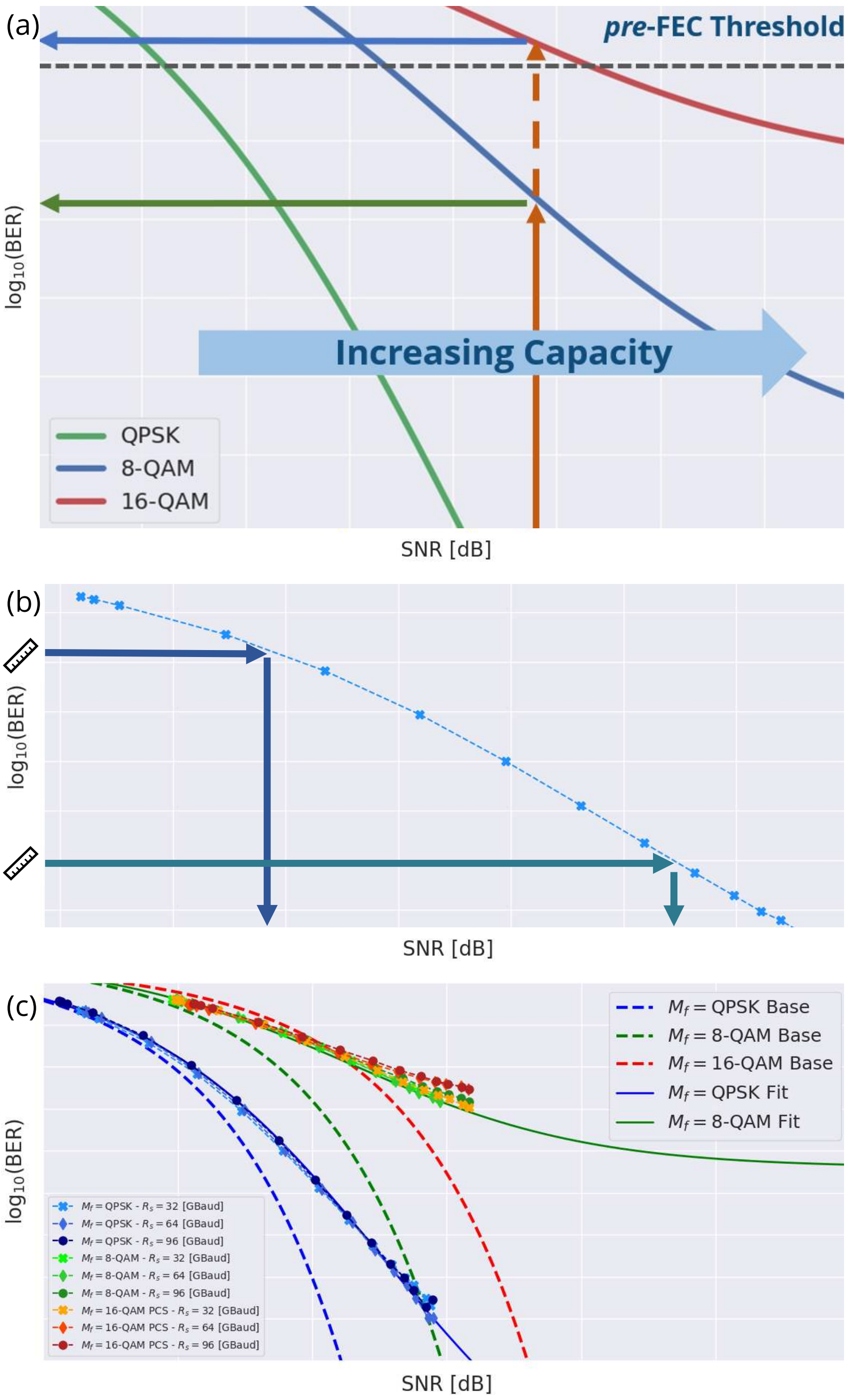

Fig. 2.1 (a) SNR-to-BER conversion function for QPSK, 8-QAM and 16-QAM modulation formats, respectively. (b) BER-to-SNR conversion for SNR prediction validations. (c) Back-to-back curves measured with commercial transceivers. Explicit values on x and y axis have been omitted because of non disclosure purposes.

slightly modified version of Eq.1.1:

$$\mathrm{SNR} = \left(\frac{1}{\mathrm{SNR}_{\mathrm{TX}}} + \frac{1}{\Delta\mathrm{OSNR}} + \frac{1}{\mathrm{SNR}_{\mathrm{RX}}} \right)^{-1}. \tag{2.3}$$

Moreover, Fig.2.1(c) demonstrate that the SNR-to-BER curves depend only on the modulation format, and slightly on the specific TRX instance, when the SNR is expressed on the channel R_s. Even more, among the characterized TRXs, all the 16-QAM formats employ the probabilistic constellation shaping (PCS) being in reality equivalent to 8-QAM formats and resulting in similar SNR-to-BER curves.

2.2 Optical Fibers

In order to provide a reference for the fiber parameters descriptions, Tab. 2.1 reports the frequency bounds of the each band composing the entire multi-band scenario considered in this work.

To ensure that the considered approach resembles a realistic use-case scenario, the description of fiber parameters has been obtained in two ways; by jointly utilizing experimental data retrieved by in-field measurements, and the use of theoretical models that are enhanced by commercial data-sheet information.

Within the following subsections, the essential physical layer parameters which must be considered to achieve an accurate wideband physical layer model are described in detail. For further in-depth analysis of these parameters see [44].

Table 2.1 Definition of the frequency bounds and total bandwidth of the each band from U to O.

BAND	Lowest Central Frequency [THz]	Highest Central Frequency [THz]	Bandwidth [THz]
U	**178.981**	**184.488**	**5.507**
L	**184.488**	**191.561**	**7.073**
C	**191.561**	**195.943**	**4.382**
S	**195.943**	**205.337**	**9.394**
E	**205.337**	**220.436**	**15.099**
O	**220.436**	**237.930**	**17.494**

2.2.1 Physical Layer Fiber Parameters

Intrinsic Loss Coefficient

The fiber loss coefficient, α, takes into account the power loss when an optical signal propagates through a fiber. The fiber attenuation depends on the propagating signal wavelength [45], which is a result of the fiber composition and manufacturing process. From a phenomenological point of view, the contributions involved in the wavelength range between 1.2 to 1.7 μm are the Rayleigh scattering, the violet and infra-red absorption, the OH-ion absorption peaks at approximately 1.25 and 1.39 μm, and the absorption due to phosphorous within the fiber core. An effective parametric model of the loss coefficient function with respect to each phenomenological factor has been provided by [46]. With all terms in logarithmic units (dB/km), the loss coefficient profile can be expressed with respect to the frequency, f:

$$\alpha(f) \simeq \alpha_{\mathrm{S}}(f)+\alpha_{\mathrm{UV}}(f)+\alpha_{\mathrm{IR}}(f)+\alpha_{13}(f)+\alpha_{12}(f)+\alpha_{\mathrm{POH}}(f)\,, \qquad (2.4)$$

where the right-hand side terms represent the Rayleigh scattering, ultraviolet, infrared, OH$^-$ and (P)OH peak absorption contributions, respectively:

$$\begin{aligned}
\alpha_{\mathrm{S}}(\lambda) &= A\lambda^{-4}+B\,,\\
\alpha_{\mathrm{UV}}(\lambda) &= K_{\mathrm{UV}}e^{C_{\mathrm{UV}}/\lambda}\,,\\
\alpha_{\mathrm{IR}}(\lambda) &= K_{\mathrm{IR}}e^{-C_{\mathrm{IR}}/\lambda}\,,\\
\alpha_{13}(\lambda) &= A_1\left(\frac{A_{\mathrm{a}}}{A_1}e^{\frac{-(\lambda-\lambda_{\mathrm{a}})^2}{2\sigma_{\mathrm{a}}^2}}+\frac{1}{A_1}\sum_{i=1}^{3}A_i e^{\frac{-(\lambda-\lambda_i)^2}{2\sigma_i^2}}\right),\\
\alpha_{12}(\lambda) &= A_1\left(\frac{1}{A_1}\sum_{i=4}^{5}A_i e^{\frac{-(\lambda-\lambda_i)^2}{2\sigma_i^2}}\right),\\
\alpha_{\mathrm{POH}}(\lambda) &= A_{\mathrm{POH}}e^{\frac{-(\lambda-\lambda_{\mathrm{POH}})^2}{2\sigma_{\mathrm{POH}}^2}}\,.
\end{aligned}$$

Focusing on a wideband scenario, the general model can be simplified by considering the relevant factors in the C-, L-, and S-bands, allowing the contributions due to the OH-ion absorption peaks at 1.25 μm and phosphorous to be neglected. Furthermore, ultraviolet absorption presents constant broadband behaviour within the band of interest. With these considerations a generic loss coefficient function may be created, considering the impact of each phenomenological contribution through the definition of four parameters; A, B, K_{IR} and A_1.

In this analysis, a loss coefficient function that has been retrieved from experimental measurements upon a standard single-mode fiber (SSMF) is considered. The full profile over the entire spectral region considered within this work is depicted in Fig. 2.2. By using this parametric model it is possible to separate the different contributions of each absorption phenomenon from a measured fiber intrinsic loss coefficient profile; remarkably this procedure has previously been performed within C-band experimental campaigns [42, 47]. For all the wideband investigations reported in this thesis, the fiber intrinsic loss coefficient profile shown in Fig. 2.2 has been considered. It is worth noting that the latest generation of deployed fiber does not feature OH absorption peaks [48], and $\alpha_{\mathrm{POH}}(f)$ can be neglected in this case.

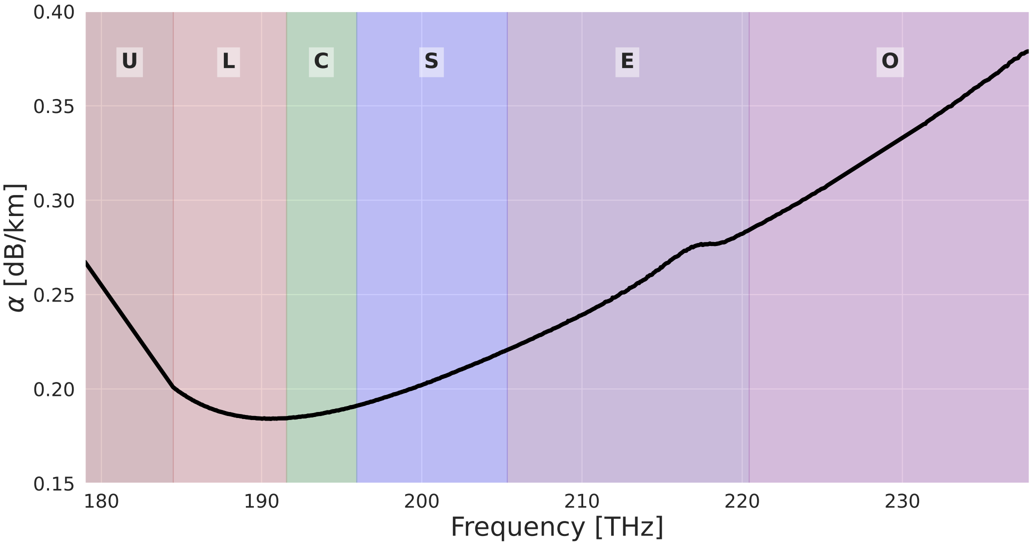

Fig. 2.2 The fiber intrinsic loss coefficients, α, evaluated over the U-to-O transmission bands.

Chromatic Dispersion

Chromatic dispersion is the dependence of the refractive index of the medium upon the propagating optical frequency; in optical communications systems this property determines the broadening of an optical pulse propagating through the fiber, due to the different speeds of each spectral component. This phenomenon is modelled by the Taylor series expansion of the mode-propagation constant, β, with respect to the central frequency of the pulse. Using this approach, β_2 is defined as the second derivative of β with respect to the optical frequency computed in the pulse central frequency, and is the parameter that describes the pulse broadening. From an application point of view, optical fiber producers report the dispersion parameter, D, as a function of the optical pulse wavelength within fiber data sheets. Considering SSMF fiber (e. g. Corning® SMF-28e®), a common expression of this parameter is:

$$D(\lambda) \approx \frac{S_0}{4}\left[\lambda - \frac{\lambda_0^4}{\lambda^3}\right], \tag{2.5}$$

where S_0 is the zero dispersion slope and λ_0 is the zero dispersion wavelength. D is related to β_2 according to the following relation:

$$\beta_2(f) = -\frac{c}{2\pi f^2} D(f), \tag{2.6}$$

where c is the speed of light in a vacuum. Values within the common tolerance ranges of commercial SSMF, $S_0 = 0.089\,\mathrm{ps/nm^2/km}$ and $\lambda_0 = 1314\,\mathrm{nm}$, have been considered for all the wideband investigations reported in this thesis. A graphical representation of D and the related β_2 parameters is reported in Fig. 2.3.

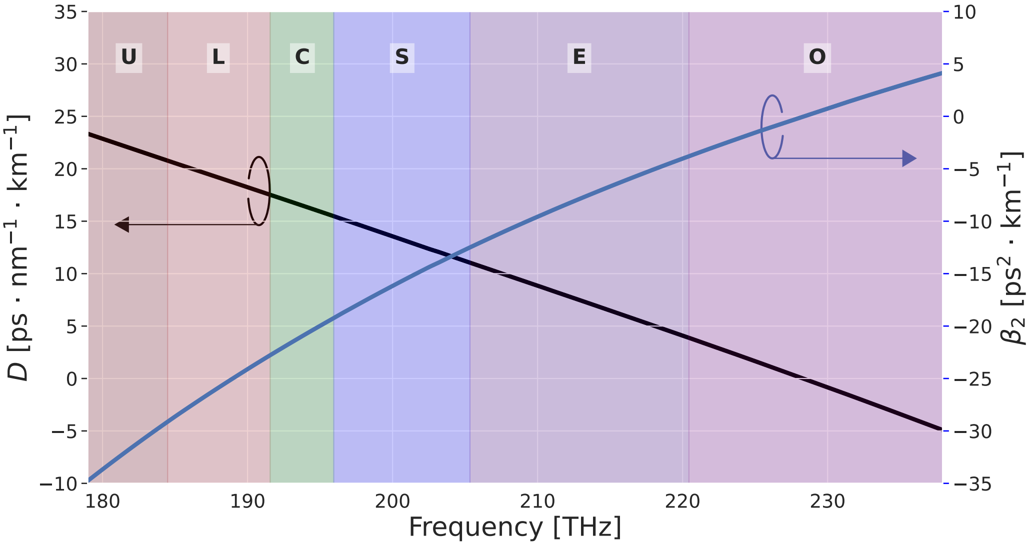

Fig. 2.3 The fiber chromatic dispersion coefficients, β_2 and D, evaluated over the U-to-O transmission bands.

Nonlinear Coefficient

The fiber nonlinear contribution is mathematically weighted within the pulse propagation equation by the nonlinear coefficient, γ. Formally, it is defined in terms of optical power as:

$$\gamma(f) = \frac{2\pi f}{c}\frac{n_2}{A_{eff}(f)}\,, \tag{2.7}$$

where n_2 is the nonlinear Kerr parameter and A_{eff} is the effective mode area. When the mode profile of the pulse is well approximated by a Gaussian function, the effective area can be evaluated as $A_{eff}= \pi w^2$, where w is the mode radius, which depends upon the central pulse wavelength and the fiber geometry. Specifically, the mode radius can be expressed as $w= a\,/\sqrt{\ln V}$, where a is the fiber core radius and the parameter V is the normalized frequency. This may be written in case of a small relative step index at the core-cladding interface, $\Delta_n \approx (n_1 - n_c)\,/\,n_1$, as:

$$V(\lambda) = \frac{2\pi}{\lambda} a n_1 \sqrt{2\Delta_n}\,, \tag{2.8}$$

where n_1 is the core refractive index and n_c is the cladding refractive index.

Fig. 2.4 showcase the frequency-dependent nonlinear coefficient and effective area profiles considered in this analysis, which have been obtained fixing the basic manufacturing fiber parameters to common SSMF values of $a= 4.2\,\mu$m and $n_2= 2.6\cdot 10^{-20}\,\text{m}^2/\text{W}$. Considering a step index fiber, the refractive indexes are computed assuming a cladding refractive index of 1.45 and a refractive index difference with respect to the core of 0.31%.

Raman Gain Coefficient

A significant broadband nonlinear phenomenon that takes place in WDM comb optical fiber propagation is the SRS [49]. The SRS involves the interaction between the propagating electromagnetic field and the dielectric medium of the fiber. In optical fiber communications, the SRS due to propagation of a WDM comb is also known as the Raman cross-talk, as the interaction in this case is only due to the different channels within the spectrum. The fundamental parameter that describes the regulation of the power transfer between channels during fiber propagation is the Raman gain coefficient, g_R, quantifying the coupling between a specific pair of

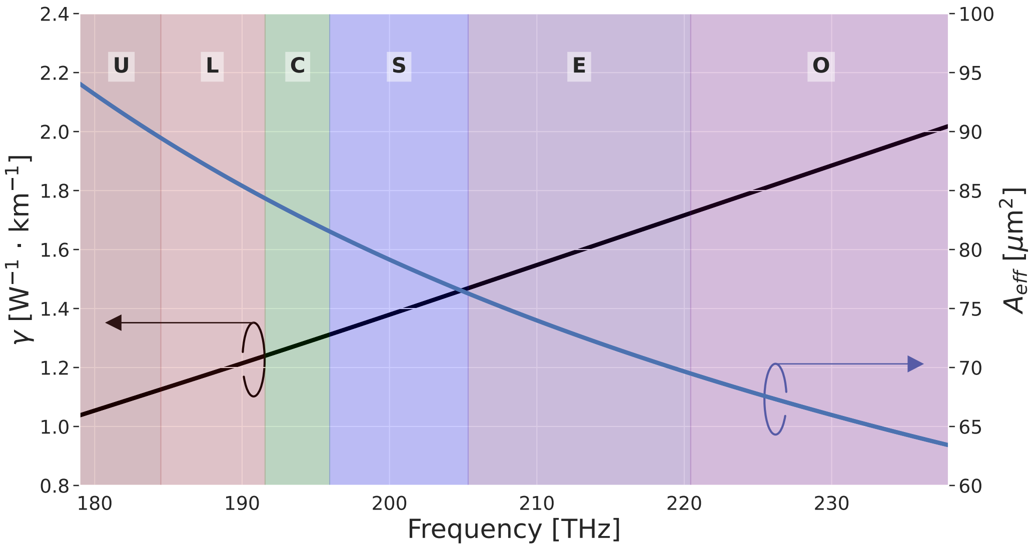

Fig. 2.4 The effective area, A_{eff}, and nonlinear coefficient, γ, evaluated over the U-to-O transmission bands.

channels with a frequency shift of $\Delta f = f_p - f_s$, where p and s represent the index of the channel at higher (pump) and lower (Stokes wave) frequencies, respectively. This coefficient depends on several features of the fiber and the propagating channel modes: the type and the concentration of dopants in the fiber core, the reciprocal polarization state, and the mode overlap between the pump and the Stokes wave and the absolute frequency of the pump. For a specific fiber, it is possible to measure the Raman gain coefficient profile using a reference pump at a frequency f_{ref} [50]. The resulting curve can be expressed in terms of optical power as:

$$g_0(\Delta f, f_{ref}) = \frac{\gamma_R(\Delta f, f_{ref})}{A_{eff}(\Delta f, f_{ref})} \ , \tag{2.9}$$

where γ_R is the Raman gain coefficient in terms of mode intensity (expressed in m/W) and $A_{eff}(\Delta f, f_{ref})$ is the effective area considering the overlap between the pump and the Stokes wave. The effective area can be estimated by taking the average of the effective areas at the single pump and Stokes wave frequencies, assuming a Gaussian mode intensity distribution [51].

In order to comprehensively simulate optical fiber propagation and include SRS effects, the complete Raman gain coefficient can be modelled by means of the following expression:

$$g_R(\Delta f, f_p) = k_{pol}^{ps} g_0(\Delta f, f_{ref}) \frac{f_p}{f_{ref}} \frac{A_{eff}(\Delta f, f_{ref})}{A_{eff}(\Delta f, f_p)} , \tag{2.10}$$

where k_{pol}^{ps} takes into account the reciprocal polarization state between the pump and the Stokes wave, and the ratios between the frequencies and effective areas account for the scaling of the pump and effective area.

Focusing on germano-silicate fibers, in particular on SSMF, the germanium concentration within the core fiber is extremely low, producing a refractive index difference of a fraction of a percentage point. In Fig. 2.5, it is shown an experimental Raman gain coefficient curve that corresponds to that of the fused silica reported in with respect the reference frequency 206.185 THz, characterized by the double peak at approximately 15 THz frequency distance between the probe and the pump. In the simulation model, all propagating channels within the WDM comb are assumed to be depolarized, introducing a unitary polarization coefficient, k_{pol}.

In the following, for a matter of simplicity, the notation of the Raman gain coefficient is:

$$g_R(\Delta f, f_{ref}) = g_R(f, f') \tag{2.11}$$

where f is the frequency of the channel under investigation and f' is the interfering channel.

2.2.2 Stimulated Raman Scattering

The first order differential equation describing the SRS is defined on the power spectral density, $\mathscr{G}(z, f)$, as follows:

$$\frac{\mathrm{d}}{\mathrm{d}z}\mathscr{G}(z, f) = \left[-\alpha(f) + \int \mathrm{d}f' g_R(f, f')\mathscr{G}(z, f')\right]\mathscr{G}(z, f) . \tag{2.12}$$

The general solution of Eq. 2.12 can be decomposed as the product of the solution of the linear operator, $\mathscr{L}(z, f)$, and a nonlinear term, $\mathscr{N}(z, f)$:

$$\mathscr{G}(z, f) = \mathscr{L}(z, f)\mathscr{N}(z, f) , \tag{2.13}$$

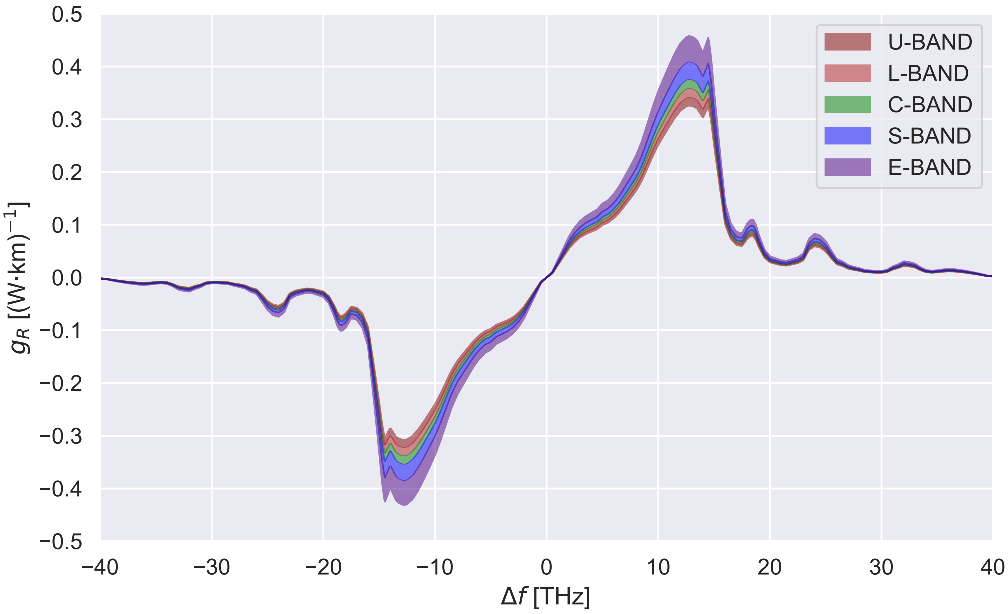

Fig. 2.5 Experimental Raman gain coefficient curve for fused silica.

given the boundary conditions:

$$\mathscr{G}(z,f)|_{z=0} = \mathscr{G}_0(f) \Rightarrow \mathscr{N}(z,f)|_{z=0} = 0\,. \tag{2.14}$$

In particular, the solution of the linear operator is defined by the following expression:

$$\begin{aligned} \left(\frac{\mathrm{d}}{\mathrm{d}z} + \alpha(f)\right)\mathscr{L}(z,f) &= 0 \\ \Rightarrow \mathscr{L}(z,f) &= \mathscr{G}(z=0,f)e^{-\alpha(f)z} \\ &= \mathscr{G}_0(f)e^{-\alpha(f)z} = \mathscr{G}_0(f)\frac{\mathrm{d}}{\mathrm{d}z}\Lambda(z,f)\,, \end{aligned} \tag{2.15}$$

where the effective length, $\Lambda(z,f)$, is defined as the integral along z of the intrinsic fiber loss:

$$\Lambda(z,f) = \frac{1-e^{-\alpha(f)z}}{\alpha(f)} \tag{2.16}$$

On the other hand, the nonlinear term must satisfy Eq. 2.17:

$$\frac{\mathrm{d}\mathscr{N}(z,f)}{\mathrm{d}z} = \mathscr{N}(z,f)\int \mathrm{d}f' g_R(f,f')\mathscr{L}(z,f')\mathscr{N}(z,f')\,. \tag{2.17}$$

A well-known exact solution of Eq. 2.17, see [52, 53] for the details, can be derived considering a flat intrinsic loss coefficient, $\alpha(f) = \alpha \Rightarrow \Lambda(z,f) = \Lambda(z)$, and a linear Raman gain coefficient, $g_R(f,f') = -(f-f')K_R$. By means of these simplifications, the solution of Eq. 2.17 is:

$$\mathscr{N}(z,f) = \frac{P e^{-fK_R P\Lambda(z)}}{\int \mathrm{d}f' \mathscr{G}_0(f') e^{-f' K_R P\Lambda(z)}}, \tag{2.18}$$

where $P = \int \mathrm{d}f \mathscr{G}_0(f)$ is the total launch power.

In general, as shown in Fig. 2.2 and Fig. 2.5, both the assumptions, a flat loss coefficient and a linear Raman gain coefficient, are increasingly inaccurate when the total bandwidth exceeds roughly 15 THz. In [54], a correction of Eq. 2.18 is proposed considering the triangular approximation of the Raman coefficient profile [55] and an interpolation of the intrinsic fiber loss coefficient.

In this work, a perturbative approach is defined, validated and analysed. The advantage of this approach is that, when the numerical series defined by the perturbative expansion converges, a truncated solution can be defined with an arbitrary level of accuracy, depending on the order of the truncation. Moreover, the solution of the perturbative expansion provides a straightforward expression of the correlation between the system parameters and the final result.

First, by means of the substitution $\Gamma(z,f) = \ln(\mathscr{N}(z,f))$, Eq. 2.17 can be written as follows:

$$\frac{\mathrm{d}\Gamma(z,f)}{\mathrm{d}z} = \int \mathrm{d}f' g_R(f,f') \mathscr{L}(z,f') e^{\Gamma(z,f')} \tag{2.19}$$

$$\Rightarrow \Gamma(z,f) = \int_0^z \mathrm{d}z' \int \mathrm{d}f' g_R(f,f') \mathscr{L}(z',f') e^{\Gamma(z',f')}. \tag{2.20}$$

Considering the Raman gain coefficient maximum value as a perturbative parameter, $\Gamma(z,f)$ can be formally defined as an infinite sum in terms of a perturbative expansion:

$$\Gamma(z,f) = \sum_{k=1}^{\infty} \Gamma^{(k)}(z,f) = \Gamma^{(1)}(z,f) + \Gamma^{(2)}(z,f) + \Gamma^{(3)}(z,f) + \cdots, \tag{2.21}$$

where the k-th order term $\Gamma^k(z,f)$ is proportional to the k-th power of the perturbative parameter, $\max\left[g_R(f,f')\right]$. By mean of this expansion, Eq.2.20 becomes:

$$\begin{aligned}
\Gamma(z,f) &= \int_0^z \mathrm{d}z' \int \mathrm{d}f' g_R(f,f')\mathscr{L}(z',f') \prod_{k=1}^{\infty} e^{\Gamma^{(k)}(z,f)} \\
&= \int_0^z \mathrm{d}z' \int \mathrm{d}f' g_R(f,f')\mathscr{L}_0(z',f') \prod_{k=1}^{\infty}\sum_{n=0}^{\infty} \frac{1}{n!}\left(\Gamma^{(k)}(z',f')\right)^n , \qquad (2.22)
\end{aligned}$$

and the k-th can be expressed as follows:

$$\begin{aligned}
\Gamma^{(k)}(z,f) &= \int_0^z \mathrm{d}z' \int \mathrm{d}f' g_R(f,f')\mathscr{L}(z',f') \\
& \sum_{\{n_j\}}\prod_{j=1}^{k-1} \frac{1}{n_j!}\left(\Gamma^{(k_j)}(z',f')\right)^{n_j} , \qquad (2.23) \\
& \forall\{n_j\} \quad \text{such that} \quad \sum_{j=1}^{k-1} k_j n_j = k-1 \, .
\end{aligned}$$

Given Eq. 2.23, successive orders can be evaluated knowing previous orders.

In particular, the first four orders are:

$$\begin{aligned}
\Gamma^{(1)}(z,f) &= \int_0^z \mathrm{d}z' \int \mathrm{d}f' g_R(f,f')\mathscr{L}(z',f') \\
&= \int \mathrm{d}f' g_R(f,f') P_0(f')\Lambda(z,f') , \qquad (2.24) \\
\Gamma^{(2)}(z,f) &= \int_0^z \mathrm{d}z' \int \mathrm{d}f' g_R(f,f')\mathscr{L}(z',f') \left[\Gamma^{(1)}(z',f')\right] , \qquad (2.25) \\
\Gamma^{(3)}(z,f) &= \int_0^z \mathrm{d}z' \int \mathrm{d}f' g_R(f,f')\mathscr{L}(z',f') \\
& \left[\Gamma^{(2)}(z',f') + \frac{1}{2}\left(\Gamma^{(1)}(z',f')\right)^2\right] , \qquad (2.26) \\
\Gamma^{(4)}(z,f) &= \int_0^z \mathrm{d}z' \int \mathrm{d}f' g_R(f,f')\mathscr{L}(z',f') \Big[\Gamma^{(3)}(z',f') \\
& + \Gamma^{(1)}(z',f')\Gamma^{(2)}(z',f') + \frac{1}{3!}\left(\Gamma^{(1)}(z',f')\right)^3\Big] . \qquad (2.27)
\end{aligned}$$

Beyond the first order, the integration in z' can be analytically solved for any other orders, obtaining an expression that depends only on the system parameters and input. As an example, the integrated solution for the second order:

$$\begin{aligned}\Gamma^{(2)}(z,f) \;&= \int \mathrm{d}f' g_R(f,f')P_0(f') \int \mathrm{d}f'' g_R(f',f'')P_0(f'') \\ &\frac{1}{2}\left[\Lambda(z,f')\Lambda(z,f'') + \left(\frac{\alpha(f')-\alpha(f'')}{\alpha(f')\alpha(f'')}\right)\frac{1-e^{-[\alpha(f')+\alpha(f'')]z}}{\alpha(f')+\alpha(f'')}\right].\end{aligned} \tag{2.28}$$

It is worth to underline that, depending on the system characteristics and the specific software implementation, it may be convenient, in terms of computational cost, to perform the analytical integration in or, instead, perform a numerical integration, maintaining an explicit expression of the previous order. As a matter of fact, looking at Eq.2.28 it can be observed that the analytical integration removes the dependency of the solution on multiple distances, required for a numerical integration, but it implies additional integrals in the frequency space.

In conclusion, considering the perturbative expansion Eq. 2.21 up to the k-th order, the truncated solution of Eq. 2.13 is:

$$\mathscr{G}^{(k)}(z,f) = \mathscr{L}(z,f)\exp\left[\sum_{j=1}^{k}\Gamma^{(j)}(z,f)\right]. \tag{2.29}$$

Considering a total number of channels, N_{ch}, combined in a WDM spectrum propagating through a single fiber span, Eq. 2.29 can be used to evaluate the corresponding k-th order power profile truncated solution:

$$\mathscr{P}_\lambda^{(k)}(z) = \int_{B_\lambda}\mathrm{d}f\,\mathscr{G}^{(k)}(z,f) = P_\lambda\, e^{-\alpha_{ch}z}\exp\left[\sum_{j=1}^{k}\Gamma_\lambda^{(j)}(z)\right], \tag{2.30}$$

where $\lambda \in [1,\cdots,N_{ch}]$ and B_λ the λ-th channel bandwidth. α_λ and $\Gamma_\lambda^{(j)}(z)$ are evaluated at the channel central frequency and considered flat within B_λ, and $P_\lambda = \int_{B_{ch}}\mathrm{d}f\,\mathscr{G}_0(f)$ is the λ-th channel launch power.

In order to quantify the accuracy of the proposed methodology, the k-th order relative error can be defined in logarithmic units as follows:

$$\mathscr{E}_\lambda^{(k)}(z) = 10\log_{10}\left(\frac{\mathscr{P}_\lambda(z)}{\mathscr{P}_\lambda^{(k)}(z)}\right) = \frac{10}{\ln(10)}\sum_{j=k}^{\infty}\Gamma_\lambda^{(j)}(z). \tag{2.31}$$

Eq. 2.31 provides an explicit expression of the accuracy achieved with different orders considered in the perturbative expansion, as the estimation error is defined as the remainder left out the truncated solution of Eq. 2.12.

2.2.3 Kerr Effect

Regarding the NLI noise, a significant level of complexity remains in modeling and simulation, even when the fiber physical parameters described in Sec. 2.2.1 are accurately known. Valuable models have been proposed in order to estimate the NLI noise generation including the SRS [56–58, 54]. These models have been accurately validated in different scenarios, both with simulations and experiments. Nevertheless, a satisfactory level of accuracy is not guaranteed, and likely compromised in a wideband scenario. The objective of this analysis is to obtain a wideband extended model that includes the frequency-dependent variations of all physical layer parameters described in Sec. 2.2.1, that also maximally enables spectral disaggregation (a fully disaggregated model is prevented by the nonlinear nature of the investigated phenomena). As described in Sec. 1.1, the disaggregated approach enables the most dynamic, flexible and efficient system optimization and operation. Moreover, as per the span-by-span accumulation, spectral disaggregation allows the distinct, simultaneous effects that contribute to the NLI noise generation to be separated.

Consequently, a spectrally disaggregated version of the GGN NLI power spectral density presented in Eq. 2 in [56] is considered. This model has been chosen as the solution of the SRS equations is not approximated, which enables further investigations into larger bandwidths. Additionally, a spectrally separated implementation of the GGN is already present in GNPy, and has been validated in several experimental test-beds, both in laboratories and brown-field infrastructures [59, 41, 43]. However, this spectrally separated GGN implementation is not explicitly disaggregated and does not take into account the frequency-dependent variations of the fiber physical parameters.

In order to obtain a disaggregated model where all frequency-dependent variations are properly considered, first the dual-polarization (DP) Manakov equation [60] is considered:

$$\partial_z \vec{A}(z,t) \;=\; \left[-\hat{\alpha}(z)+\imath\hat{\beta}\right]\vec{A}(z,t)-\imath\frac{8}{9}\hat{\gamma}\left[\vec{A}(z,t)\cdot\vec{A}^{*}(z,t)\right]\vec{A}(z,t)\,, \qquad (2.32)$$

where $\vec{A}(z,t)$ is the DP modal amplitude at the position z at the time t; $\hat{\alpha}(z)$, $\hat{\beta}$ and $\hat{\gamma}$ are the gain/loss, chromatic dispersion and nonlinear coefficient operators, respectively; $\imath$ represents the imaginary unit, and the operator $\cdot$ is the standard product in the bi-dimensional polarization space. As Eq. 2.32 is expressed in time-domain representation, the gain/loss, dispersion and nonlinear coefficient are defined as operators. In particular, $\hat{\beta}$ is a convolution in the time-domain representation that can be expressed as a frequency-dependent multiplicative factor considering a basis in the frequency-domain representation space. Whereas, $\hat{\alpha}(z)$ accounts for the power variation along the position induced by both the intrinsic fiber loss and the SRS. In this analysis, the Kerr effect is considered as a perturbative nonlinear effect generated by the DP modal amplitude solution of the SRS equation described in Sec.2.2.2, therefore, $\hat{\alpha}(z)$ can be defined as a linear operator and can be expressed as a frequency- and position-dependent multiplicative factor considering a basis in the frequency-domain representation space.

The Manakov equation significantly simplifies NLI estimation by neglecting the PMD introduced by the fiber propagation. A more general approach can be obtained considering the dual-polarization coupled nonlinear Schrodinger equation (DP-CNLSE) [60], which takes into account the stochastic birefringence realization inducing the PMD. Nevertheless, the focus of this study is a solution in a disaggregated network framework, where the signal transmitted through a specific OLS can be considered as fully Gaussian and depolarized, for each span. Under these conditions, it has been shown that the effect of PMD on the NLI generation is negligible [61], and that the small differences between the solutions of the Manakov equation and the DP-CNLSE do not vary significantly when enlarging the investigated bandwidth up to 4 THz. In this analysis the solutions of the Manakov equation and the DP-CNLSE are assumed to be not significantly different when a wideband transmission scenario is considered, as their differences do not depend on the overall bandwidth.

The formal solution of Eq. 2.32 is a combination of a linear, $\mathscr{L}(z)$, and a nonlinear, $\mathscr{N}(z)$, operators applied to the modal amplitude at the fiber input, $\vec{A}(z=$

$0,t) = \vec{A}(t)$:

$$\vec{A}(z,t) = \mathscr{L}(z)\mathscr{N}(z)\vec{A}(t)\,, \tag{2.33}$$

given the following properties:

$$\partial_z \mathscr{L}(z)\mathscr{L}^{-1}(z) = \left(-\hat{\alpha}(z) + \imath\hat{\beta}\right)\,, \tag{2.34}$$

$$\mathscr{L}(z)\partial_z \mathscr{N}(z)\mathscr{N}^{-1}(z)\mathscr{L}^{-1}(z) = -\imath\frac{8}{9}\hat{\gamma}\left[\vec{A}(z,t)\cdot\vec{A}^*(z,t)\right]. \tag{2.35}$$

In standard fiber-optic transmission the nonlinear term in Eq. 2.32 can be considered as a perturbation source of the NLI noise amplitude, $\vec{A}_{\mathrm{NL}}(z,t)$, of the linear propagation of the signal, $\vec{A}_{\mathrm{L}}(z,t) = \mathscr{L}(z)\vec{A}(t)$:

$$\vec{A}(z,t) \approx \vec{A}_{\mathrm{L}}(z,t) + \mathscr{L}(z)\vec{A}_{\mathrm{NL}}(z,t)\,, \tag{2.36}$$

where $\vec{A}_{\mathrm{NL}}(z,t)$ includes the perturbative expansion of $\mathscr{N}(z)$ up to a certain γ order, and Eq. 2.36 is an identity only when all perturbation orders are summed to obtain $\vec{A}_{\mathrm{NL}}(z,t)$. In optical communications scenarios, an accurate estimation of the NLI can be obtained by considering the $\mathscr{N}(z)$ first order perturbation in γ, and the noise amplitude can be calculated as the solution of the following differential equation:

$$\mathscr{L}(z)\partial_z \vec{A}_{\mathrm{NL}}(z,t) = -\imath\frac{8}{9}\hat{\gamma}\left[\vec{A}_{\mathrm{L}}(z,t)\cdot\vec{A}_{\mathrm{L}}^*(z,t)\right]\vec{A}_{\mathrm{L}}(z,t)\,. \tag{2.37}$$

In general, $\vec{A}(z,t)$ is the superposition of N_{ch} uncorrelated signals and can be written as follows:

$$\vec{A}(z,t) = \sum_{i=1}^{N_{ch}} \vec{A}_{\lambda_i}(z,t) = \sum_{i=1}^{N_{ch}} \int_{-\infty}^{\infty} \mathrm{d}f \vec{A}_{\lambda_i}(z,f) e^{\imath 2\pi f t}\,, \tag{2.38}$$

where $\vec{A}_{\lambda_i}(z,f_i)$ is the Fourier transformation of $\vec{A}_{\lambda_i}(z,t)$. In the frequency domain, the $\mathscr{L}(z)$ is diagonal and has the following solution for the ith channel:

$$\vec{A}_{\mathrm{L},\lambda}(z,f) = \sqrt{\frac{P_\lambda}{2R_{s_\lambda}}\rho_\lambda(z)}\, e^{-\imath\beta(f)z}\, \vec{\varphi}_\lambda(f)\,, \tag{2.39}$$

where P_λ is the total channel power over the two polarization states, $R_{s,\lambda}$ is the channel symbol rate, $\rho_\lambda(z)$ is the channel power gain/loss profile along z, and $\vec{\varphi}_\lambda(f)$ is the channel transmitted modulated signal, in the frequency domain, normalized with respect to both the average channel power for each polarization and the channel symbol rate. In particular, $\rho_\lambda(z)$ can be found for each channel by solving the coupled SRS equations [51]. This set of coupled equations can be solved numerically by evaluating the power profile for all channels incrementally by position [62], or considering the perturbative SRS solution presented in Sec.2.2.2.

In general, the metric $P_{\mathrm{NLI};\lambda}$ used in Eq. 1.3 can be defined as the variance of the noise amplitude, $\vec{A}_{\mathrm{NL}}$, evaluated for a specific received channel. In further detail, in order to estimate $P_{\mathrm{NLI};\lambda}$, the channel signals are supposed to be received after propagation through the fiber span with an ideal receiver that applies the matched filter for the channel, compensates for all accumulated CD and PMD, and equalizes the channel signal by compensating for the entire fiber gain/loss profile. By means of these transformations, the channel signal reduces to $\vec{\varphi}_\lambda(f)+\vec{A}_{\mathrm{NL},\lambda}(f)$, where L_s is the span length and $\vec{A}_{\mathrm{NL},\lambda}(f)=\vec{A}_{\mathrm{NL},\lambda}(z=L_s,f)$ is the solution of Eq. 2.37 in the frequency domain. At this point, the ideal receiver can sample the signal and the $P_{\mathrm{NLI};\lambda}$ can be defined as the variance of the $\vec{A}_{\mathrm{NL},\lambda}(f)$ power over all symbol sequences in the realization space:

$$\begin{aligned} P_{\mathrm{NLI};\lambda} &= \int_{-\infty}^{\infty}\mathrm{d}f\int_{-\infty}^{\infty}\mathrm{d}f'\,\mathbf{Cov}\left[\vec{A}_{\mathrm{NL},\lambda}\right], \qquad (2.40)\\ \mathbf{Cov}\left[\vec{A}_{\mathrm{NL},\lambda}\right] &= \left\langle\vec{A}^*_{\mathrm{NL},\lambda}(f')\cdot\vec{A}_{\mathrm{NL},\lambda}(f)\right\rangle-\left\langle\vec{A}^*_{\mathrm{NL},\lambda}(f')\right\rangle\cdot\left\langle\vec{A}_{\mathrm{NL},\lambda}(f)\right\rangle, \end{aligned}$$

where $\langle\cdots\rangle$ represents the expectation value operator over the symbol ensemble. As each normalized transmitted channel signal, $\vec{\varphi}_\lambda(f)$, can be considered as Gaussian distributed (in the symbol sequence realization space), with a unitary power on each polarization, and statistically independent with respect to other channels, the expectation value operator verifies the following property:

$$\begin{aligned} \left\langle\prod_{i,j}^{N}\vec{\varphi}^*_{\lambda_i}(f_i)\cdot\vec{\varphi}_{\lambda_j}(f_j)\right\rangle &= \sum_{p\in\mathbf{P}}\prod_{i,j}^{N}\left\langle\vec{\varphi}^*_{\lambda_i}(f_i)\cdot\vec{\varphi}_{\lambda_j}(f_j)\right\rangle\\ &= \sum_{p\in\mathbf{P}}\prod_{i,j}^{N}2\delta^{\lambda_i}_{\lambda_j}\delta(f_i-f_j), \qquad (2.41) \end{aligned}$$

where $\mathbf{P}$ is the space of all i, j permutations that results in a nonzero expectation value,$\delta^{\lambda_i}_{\lambda_j}$ and $\delta(f_i-f_j)$ are the Kronecker and Dirac deltas, respectively.

With a few steps of algebra, as in [56], the solution of Eq.2.37 can be evaluated in Eq. 2.40 and, separating the self-channel, $P_{\mathrm{SC},\lambda}$, and cross-channel $P_{\mathrm{XC},\lambda}$ NLI noise powers:

$$P_{\mathrm{SC},\lambda} = \eta_{\lambda,\lambda} P_\lambda^3 = \gamma_\lambda^2 \mathscr{W}_{\mathrm{SC}} \mathscr{I}_\lambda^\lambda (L_s) \frac{P_\lambda^3}{{Rs_\lambda}^3}, \tag{2.42}$$

$$P_{\mathrm{XC},\lambda,\kappa} = \eta_{\lambda,\kappa} P_\lambda P_\kappa^2 = \gamma_\lambda^2 \mathscr{W}_{\mathrm{XC}} \mathscr{I}_\kappa^\lambda (L_s) \frac{P_\lambda}{Rs_\lambda} \left(\frac{P_\kappa}{Rs_\kappa} \right)^2, \tag{2.43}$$

where λ and κ represent the CUT and the interfering channel, respectively. Additionally:

$$\begin{aligned} \mathscr{W}_{\mathrm{SC}} &= (1+C_\infty) \left(\frac{8}{9} \right)^2 \frac{6}{2^3} = (1+C_\infty) \frac{16}{27}, \\ \mathscr{W}_{\mathrm{XC}} &= 2 \frac{16}{27}, \end{aligned}$$

are the single-channel (SC) and cross-channel (XC) weights coming from the statistics and the polarization, whereas

$$\begin{aligned} \mathscr{I}_\kappa^\lambda (L_s) &= \int_{-\infty}^{\infty} \mathrm{d}f \int_{-\infty}^{\infty} \mathrm{d}f' \int_{-\infty}^{\infty} \mathrm{d}f'' \mathrm{I}_\kappa(f') \mathrm{I}_\kappa(f'-f'') \\ &\quad \cdot \mathrm{I}_\lambda (f-f'') \mathrm{I}_\lambda (f) \left| \Psi_\kappa \left(L_s; f', f'', f \right) \right|^2, \end{aligned} \tag{2.44}$$

where:

$$\mathrm{I}_\lambda (x) = \begin{cases} 1 & \text{if} \quad x \in \mathrm{I}_\lambda \equiv \left[f_\lambda - \frac{R_{s_\lambda}}{2}, f_\lambda + \frac{R_{s_\lambda}}{2} \right] \\ 0 & \text{otherwise} \end{cases},$$

$$\Psi_\kappa \left(L_s; f', f'', f \right) = \int_0^{L_s} \mathrm{d}z \, \rho_\kappa^2 (z') e^{\imath 2\pi^2 \Delta\beta_\kappa^\lambda (f', f'', f) z}, \tag{2.45}$$

$$\begin{aligned} \Delta\beta_\kappa^\lambda (f', f'', f) &= \beta(f') - \beta(f'-f'') + \beta(f-f'') - \beta(f) \\ &\approx \frac{(2\pi)^2}{2} f''(f'-f) \left[\beta_2(f') + \beta_2(f) \right] . \end{aligned}$$

In general, further analytical simplifications of Eq.2.44 may be possible, but Eq. 2.45 cannot be analytically integrated, as $\rho_\kappa^2(z)$ is evaluated numerically and its exact value depends on the signal launch power. As a disaggregated version of the GGN has been obtained, allowing a more accurate depiction of the multi-band scenario, the next objective is finding a numerical approximation to Eq. 2.44 that allows a fast and accurate simulation of the investigated wideband transmission scenario.

The GGN implementation in GNPy evaluates Eq. 2.44 by numerical integration with a less precise expression of the frequency-dependent fiber parameters. This solution is time consuming, does not scale properly with the number of the interfering channels, and it is prone to numerical errors due to artificial resonances, especially when the interference channel is spectrally distant from the CUT. In this work, a numerical solution to Eq. 2.44 is obtained through an approximation: first dividing the fiber length in N uniform steps, $\{z_0 = 0, ..., z_m = m\Delta z, ..., z_N = L_s\}$, such that within each step $\rho_{\kappa,m}^2(z) = \rho_{\kappa,m}^2(z_m)e^{-\tilde{\alpha}_m(z-z_m)}$. By means of this decomposition, Eq. 2.45 can be solved incrementally by applying an analogous methodology to the one reported in [63], providing the following approximate solution on the m-th step:

$$\Psi_\kappa\left(z_m; f', f'', f\right) \approx \frac{\Lambda(z_m)}{\left[1 - \imath \frac{\Delta\beta_\kappa^\lambda(f', f'', f)}{\tilde{\alpha}_m}\right]}. \tag{2.46}$$

where the effective length evaluated at the m-th step, $\Lambda(z_m)$, is defined as follows:

$$\Lambda(z_m) = [\rho_{\kappa,m}^2(z_m) - \rho_{\kappa,m}^2(z_{m+1})]/\tilde{\alpha}_m. \tag{2.47}$$

Finally, by substituting this approximated solution into Eq. 2.44:

$$\mathscr{I}_\kappa^\lambda(L_s) \approx \sum_{m,n} \frac{\sqrt{|\tilde{\alpha}_m\tilde{\alpha}_n|}\Lambda(z_m)\Lambda(z_n)R_{s_\lambda}R_{s_\kappa}}{4\pi\left|\frac{(\beta_\kappa+\beta_\lambda)}{2}(f_\kappa - f_\lambda)\right|}. \tag{2.48}$$

Eq. 2.48 is based on an approximation that is verified and has been validated in this work for all the XC terms and all the CUTs. In order to extend the approximation to the SC term, $\kappa = \lambda$, further analysis are required and in this study SC estimator equivalent to the GGN implementation is used.

This solution enables accurate and fast NLI computation, and scales properly with the number of CUTs and interfering channels, providing a result for the investigated wideband transmission scenario in a computational time adequate for streaming operations.

2.3 Optical Amplifier

Optical amplifiers are devices that amplify optical signals without converting them to electrical signals, thus allowing for all-optical long-distance transmission. There are several types of optical amplifiers, including doped fiber amplifiers, Raman amplifiers, and semiconductor optical amplifiers (SOAs). EDFAs are the most commonly used type of optical amplifier, and they work by introducing erbium ions into the fiber core, which can be excited by a pump laser to amplify the signal. The efficient amplification bandwidth of erbium is limited to the C and L band, therefore, in wideband transmission scenarios, other rare-earth ions are used for manufacturing doped fiber amplifiers. Moreover, in a multi-band transmission scenario, each band is amplified by a distinct device. Raman amplifiers use stimulated SRS to amplify the signal, and SOAs use the injection of a current to create a population inversion in the semiconductor material, allowing for amplification. Within this thesis work, only doped fiber amplifiers have been considered, but all the results can be extended to different types of optical amplifications.

In order to adequately model optical amplifiers and their effects on the signal transmission, both the amplification and generated noise profiles must be taken into account. In general, the target of optical amplifiers is an amplification profile applied to the input signal, which is characterized by a gain offset, G, recovering the overall fiber loss, and a linear tilt, T, compensating for the SRS induced power transfer. Additionally, the gain profile has fluctuations/ripples [64] due to specific device manufacturing. Without any loss of generality, the frequency-dependent gain profile can be expressed as follows:

$$G(f) = G + T\frac{(f - f_0)}{B_A} + r_T(f)\,, \tag{2.49}$$

where f_0 and B_A are the central frequency and the total amplification bandwidth, respectively, and r_T is a ripple profile of the specific device; the latter depends on the target tilt and on the specific device implementation [65].

The ASE noise generated by the optical amplifiers can be analytically estimated for each channel using the well-known ASE noise power formula:

$$P_{\text{ASE}}(f) = hfNF(f)[G(f)-1]B_n \tag{2.50}$$

where, h and B_N are the Planck constant and the considered noise bandwidth, respectively, and NF is the EDFA noise figure.

The described modeling and characterization are verified when a full spectral load transmission is considered. As a matter of fact, when the amplified spectral load occupies portions of the entire amplification bandwidth, additional fluctuations are observed. These variations undermine the accuracy of Eq. 2.49 and Eq. 2.50 and must be taken into account in partially loaded spectrum transmission scenarios. Remarkably, the spectral load induced fluctuations cannot be described by analytical models and represent the perfect ground for ML applications as shown in Ch. 5.

2.4 Optical Switch

ROADMs are a type of optical switch that allows network operators to add or drop optical channels at different points in the network, enabling a dynamic and flexible routing of the traffic in meshed network infrastructures. State-of-the-art ROADMs are based on wavelength selective switches (WSSs), exploiting liquid-crystal on silicon (LCoS) spatial light modulator (SLM) technologies [66], which may introduce substantial PDL.

2.4.1 Polarization-Dependent Loss

The PDL impact has been extensively analyzed for propagation of polarized intensity-modulated channels [67], while the impact on DP coherent technologies has not yet been entirely clarified in order to be used within the physical layer model of optical networks [15].

Every ROADM degree is composed of a pair of WSSs that serve as multiplexer (MUX) and de-multiplexer (DEMUX) of the relative WDM spectrum, enabling the add and drop of specific channels and the routing of the crossing spectrum through multiple input/output ports. Additionally, each WSS component apply a

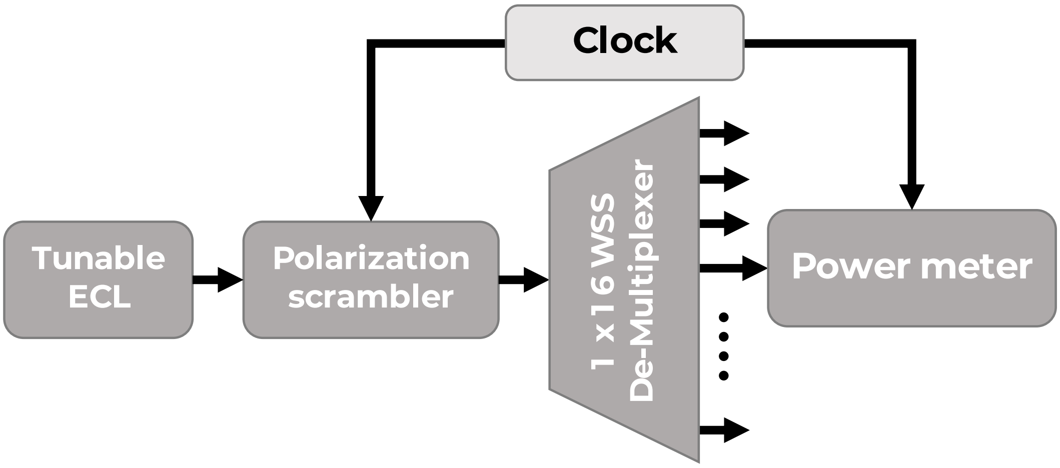

Fig. 2.6 Experimental setup for PDL measurement.

certain attenuation to each channel, enabling a selective equalization of the WDM spectrum. Due to specific manufacturing imperfections, each channel experiences a different polarization-dependent loss for each input/output port routing. As the propagation through the fiber span induces a frequency-dependent and random polarization rotation on each channel polarization state, the PDL effect on each channel as a stochastic nature. The statistic of the PDL effect has been experimentally characterized and investigated in [68, 69]. In this section, an analytical description of the PDL effect on the signal transmission is presented, drawing upon experimental observations.

PDL Characterization

The measurement setup utilized for the characterization of PDL in [68] is depicted in Fig. 2.6. At the transmitter side, a tunable C-band external cavity laser (ECL) ranging from 191.3 to 196 THz is used as optical source. The optical signal passes through an optical polarization scrambler (PS), which is able to explore all the states of polarization of the Poincaré sphere in about 1 minute, and then is fed to a 1x16 ROADM WSS DEMUX. Each port of the WSS can be programmed setting the filter bandwidth (50 GHz), the central frequency (matched to the ECL frequencies) and the attenuation (0-15 dB). The received signal is measured using a conventional power meter sampling the instant power at the sampling rate of 3 KSamples/s for a time lapse of 85 s.

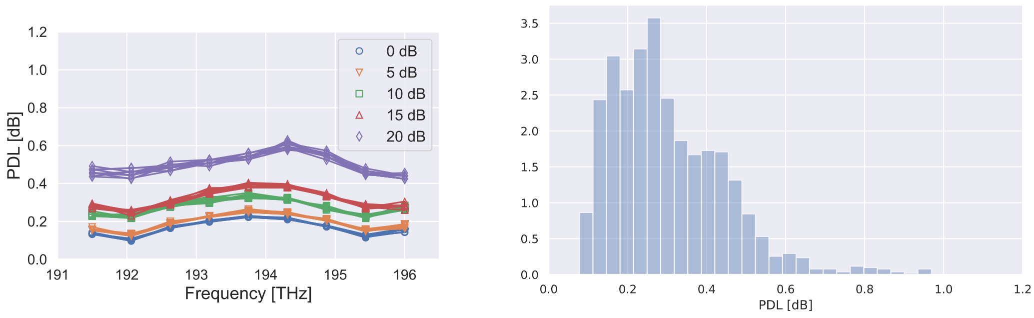

(a) (b)

Fig. 2.7 (a) Single-port PDL measurement repeated 10 times. (b) Overall distribution of the PDL experimental measurements for all VOA attenuation values.

The PDL for a specific port and specified ECL frequency and attenuation is evaluated using its definition:

$$\mathrm{PDL} \triangleq 10\log_{10}\left(\frac{P_{\mathrm{MAX}}}{P_{\mathrm{min}}}\right) , \tag{2.51}$$

where P_{MAX} and P_{min} are the maximum and minimum power values recorded during the whole time of a single measurement for a fixed frequency and WSS port, while the ECL orientation span the polarization space due to the PS.

The robustness of the experimental setup has been tested verifying the repeatability of the measurement process. Selecting a single port of the WSS, the PDL measurement has been repeated for 10 times for a set of 9 frequencies and 4 attenuation values. The result of this test is shown in Fig. 2.7(a), where the repeated measurements are plotted with different markers according to the attenuation. In general, each set of PDL values, obtained setting a specific value of attenuation, presents similar estimations despite of measurement uncertainty along the whole C-band range, proving that the PDL measurement is repeatable and deterministic.

After this preliminary phase, the PDL measurement has been performed for all the ports of the WSS, setting the same ranges of frequencies and attenuation values, for a total of 576 PDL measurements (36 per port). The complete distribution of PDL measurements is represented in Fig. 2.7(b).

The device under test presents an average PDL of 0.26 dB with a standard deviation of 0.14 dB. Since the port attenuation is a key factor for optical switching operations, it becomes crucial to understand how the PDL changes with respect to this quantity. Grouping all the PDL estimations according to the attenuation, 5 distributions are obtained showing both increasing average and standard deviation. The statistics are summarized in Tab. 2.2.

Attenuation [dB]	μ [dB]	σ [dB]
0	0.20	0.11
5	0.22	0.11
10	0.29	0.11
15	0.32	0.11

Table 2.2 Mean and standard deviation of the PDL experimental distribution for each value of VOA attenuation.

PDL Effect

Depending both on frequency and ports, the PDL introduced by each WSS must be treated as a random variable in the vast majority of use cases where a full characterization of all the WSS is not available and not feasible. In this scenario, a worst-case value of PDL can be considered for evaluating a conservative SNR penalty. Remarkably, this value is commonly provided in WSS datasheets, sometimes even varying with the attenuation. Therefore, in the scope of this thesis, worst-case value of PDL for each WSS is considered as a deterministic values with a certain polarization orientation. Even so, the PDL effect maintain a stochastic nature due to the fiber birifringence, whose effect is a random polarization rotation of the propagating signal. Thus, the total effect of the PDL along a lightpath including multiple WSSs varies in time as the fiber birifringence effect. Even more, the noise generated at distinct point of the lightpath experiences a different PDL effect with respect to the signal. This result in a complex and statistical final SNR impairment induced by the PDL

PDL Penalty

The PDL distribution of each WSS may be used in a Monte Carlo analysis to estimate the impact of the PDL on the system performance, allowing a realistic investigation of the phenomenon according to the attenuation value. Nevertheless, Monte Carlo simulations are time consuming and unfeasible for a dynamic and flexible digital model. Therefore, a simplified approach is required for estimating the PDL penalty in a fast and disaggregated manner.

As shown in [69], the PDL-induced SNR penalties can be quantified by means of a certain margin that guaranties a threshold tolerance of out-of-service, τ. In particular, the channel SNR at the receiver, on one polarization state, is a stochastic variable characterized by a Gaussian distribution (in linear units). For a given transmission scenario, the SNR distribution for one polarization state can be identified by two essential features: the distribution standard deviation, σ, and the difference between the maximum and minimum received SNR, χ. Given these two characteristic quantities, the PDL-induced SNR penalty can be evaluated by means of the probability equivalent to the integral of the truncated Gaussian distribution. The objective of this study is the definition of analytical expressions of both σ and χ.

First, it is important to notice that the statistical characterization of the PDL on the power of a single- and DP signal as been investigated and described in a large set of previous works in the literature [70–77]. In particular, the probability density function of the PDL effect on a DP signal power is given in [77] for a generic optical link composed of an arbitrary number, n, of elements introducing PDL that can be described as the stochastic power transfer matrix $T^{\dagger}_{(1\to n)}T_{(1\to n)}$, where $T_{(1\to n)} = T_n \cdots T_i \cdots T_1$ is the composition of the field transfer functions of each i-th PDL section, and $T^{\dagger}_{(1\to n)}$ is its adjoint matrix.

In order to evaluate the PDL-induced SNR penalty, it is essential to define an adequate abstraction of the optical link and the receiver framework. Each general optical link can be divided in PDL subsystems, each consisting of an element introducing a certain PDL, corresponding to T_i, on both the transmitted signal and the accumulated noise fields, and a set of concatenated fiber and EDFA introducing a given amount of DP noise field, $\vec{N}_i$. In this framework, the transmitted DP signal field, $\vec{S}_{\mathrm{RX}}$, experiences the entire link PDL, whereas, the noise field generated in a specific PDL subsystem experiences only the PDL of the successive PDL subsystems. Therefore, the received DP signal field, $\vec{S}_{\mathrm{RX}}$, and noise field, $\vec{N}_{\mathrm{RX}}$, at the optical link termination can be written as follows:

$$\vec{S}_{\mathrm{RX}} = T_{(1\rightarrow n)}\vec{S}_{\mathrm{TX}}\,, \tag{2.52}$$

$$\vec{N}_{\mathrm{RX}} = \sum_{i=1}^{n} T_{(i+1\rightarrow n)}\vec{N}_i\,. \tag{2.53}$$

In this thesis, it is assumed that the receiver is able to recover completely the field transfer function of $\vec{S}_{\mathrm{RX}}$ in order to maintain the relationship between the transmission SNR and the BER described in 2.1 and to obtain a PDL-induced SNR penalty that is independent of the specific DSP implementation. In light of this consideration, Eq. 2.52 and Eq. 2.53 become:

$$\vec{S}_{\mathrm{RX}} = T^{-1}_{(1\rightarrow n)}T_{(1\rightarrow n)}\vec{S}_{\mathrm{TX}} = \vec{S}_{\mathrm{TX}}\,, \tag{2.54}$$

$$\vec{N}_{\mathrm{RX}} = T^{-1}_{(1\rightarrow n)}\sum_{i=1}^{n} T_{(i+1\rightarrow n)}\vec{N}_i = \sum_{i=1}^{n} T^{-1}_{(1\rightarrow i)}\vec{N}_i\,. \tag{2.55}$$

Consequently, the $\mathrm{SNR}_{\mathrm{RX},x}$ probability distribution of a single-polarization state, x, can be derived considering the deterministic signal x-projection power, $S_{\mathrm{RX},x} = |\vec{S}_{\mathrm{RX}} \cdot \hat{x}|^2$, and the stochastic noise x-projection power, $N_{\mathrm{RX},x} = |\vec{N}_{\mathrm{RX}} \cdot \hat{x}|^2$, obtained from equation Eq. 2.55. Additionally, as the PDL of successively crossed PDL subsystems has the same effect on both the signal and the noise fields, the $\mathrm{SNR}_{\mathrm{RX},x}$ can be expressed in a disaggregated manner as the proper sum of the separate contribution of SNR degradation generated in each distinct PDL subsystem:

$$\begin{aligned}\mathrm{SNR}_{\mathrm{RX},x} &= \left(\mathrm{SNR}^{-1}_{1,x} + \cdots + \mathrm{SNR}^{-1}_{n,x}\right)^{-1} = \frac{S_{\mathrm{RX},x}}{N_{1,x} + \cdots + N_{\mathrm{n},x}} \\ &= \frac{S_{\mathrm{RX},x}}{\left|\left(T_1^{-1}\vec{N}_1\right)\cdot\hat{x}\right|^2 + \cdots + \left|\left(T^{-1}_{(1\rightarrow n)}\vec{N}_{\mathrm{n}}\right)\cdot\hat{x}\right|^2}\,.\end{aligned} \tag{2.56}$$

Eq. 2.56 implies that both σ and χ can be expressed knowing the nominal and average values of the SNR degradation of each PDL subsystem, and the stochastic characterization of the noise power distributions. In particular, the probability density function of the PDL effect on the noise power given in [77] can be used to evaluate the average, $\mu_{N_{i,x}}$, the standard deviation, $\sigma_{N_{i,x}}$, and the difference between the maximum and minimum, $\chi_{N_{i,x}}$, of the i-th PDL subsystem noise power contribution,

$N_{\mathrm{i},x} = |(T^{-1}_{(1\to i)}\vec{N}_\mathrm{i}) \cdot \hat{x}|^2$. Consequently, σ and χ can be analytically evaluated by means of the following expressions:

$$\begin{aligned}\sigma &= \sqrt{\sum_{i,j=1}^{n}\left(\frac{\partial \mathrm{SNR}_{\mathrm{RX},x}}{\partial N_{i,x}}\frac{\partial \mathrm{SNR}_{\mathrm{RX},x}}{\partial N_{j,x}}\sigma_{N_{i,x}}\sigma_{N_{j,x}}\right)} \\ &= \mu\sqrt{\sum_{i,j=1}^{n}\left(\frac{\sigma_{N_{i,x}}\sigma_{N_{j,x}}}{S^2_{\mathrm{RX},x}}\right)}, \qquad (2.57)\end{aligned}$$

where μ is the average $\mathrm{SNR}_{\mathrm{RX},x}$ which is equal to the nominal $\mathrm{SNR}_{\mathrm{RX},x}$ obtained considering no PDL in the system, and

$$\chi = \left(\sum_i \frac{\mu_{N_{i,x}} - \frac{\chi_{N_{i,x}}}{2}}{S_{\mathrm{RX},x}}\right)^{-1} - \left(\sum_i \frac{\mu_{N_{i,x}} + \frac{\chi_{N_{i,x}}}{2}}{S_{\mathrm{RX},x}}\right)^{-1}. \qquad (2.58)$$

In particular, Eq. 2.57 has been obtained from the well-known covariance formula for the error propagation and it is not an exact solution, in general. Nevertheless, it provides a very accurate and conservative prediction of σ and it is expressed in a disaggregated manner, as Eq.2.58, such that the statistical characterization of the PDL effect on the channel SNR at a certain span can be easily evaluated considering only the previous and the current span.

In general, further analysis on the PDL statistics may provide a more accurate approach providing a more accurate estimation of the PDL-induced SNR degradation.

Chapter 3

Physical Layer Model Validations

In this chapter, experimental validations of the physical layer model presented in Sec. 2 are reported and discussed. Moreover, a Monte Carlo analysis of the PDL-induced GSNR penalty is included.

3.1 GNPy Validations

In this section, experimental validation and accuracy assessments of GNPy initially introduced in [78, 43, 79, 59], are documented. These experimental campaigns have been carried out in laboratory testbed at Orange Labs in Lannion, France, using commercial transmission and OLS equipment.

Experimental Setup

Fig. 3.1 and Fig. 3.2 illustrate a detailed description and a schematic of the experimental setup assembled at Orange Labs, which has been employed to measure various QoT transmission metrics in a flex-grid flex-rate scenario. The OLS under consideration is composed of 20×80 km spans of ITU.T G.652 fiber with an average loss of 16.6 dB, dispersion values of 16.7 ps / (nm·km) and effective areas of $80\,\mu\text{m}^2$, both evaluated at a reference wavelength of 1550 nm. After each fiber span, a JDSU WRA 200 EDFA is placed and operated in a constant gain mode in order to fully recover the fiber loss. In order to compensate for SRS effects, each EDFA gain tilt has been set so that 1 dB of tilt over the spectrum bandwidth is recovered

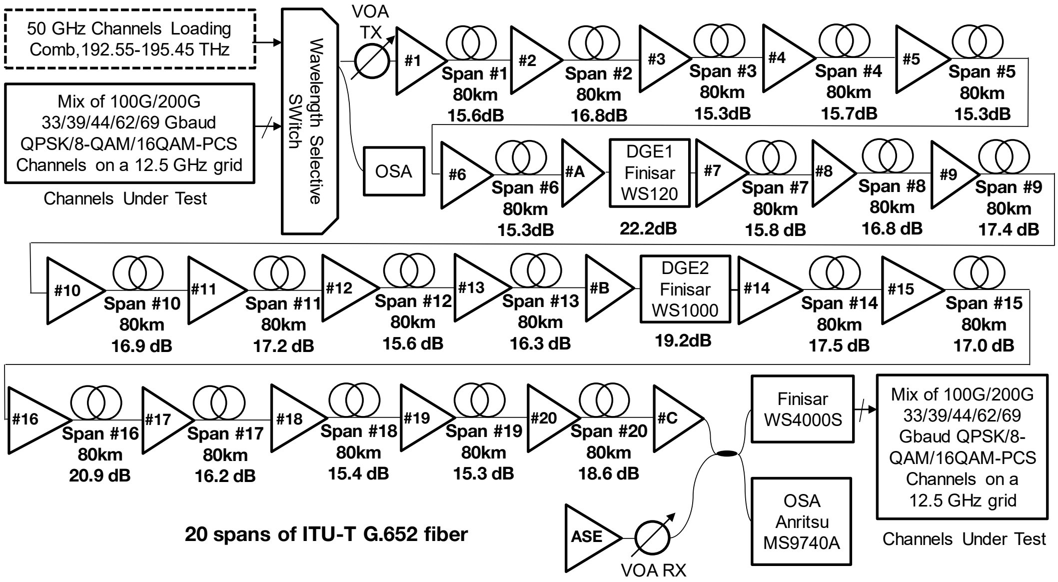

Fig. 3.1 A flow diagram providing a representation of the optical line used for transmission within this experiment.

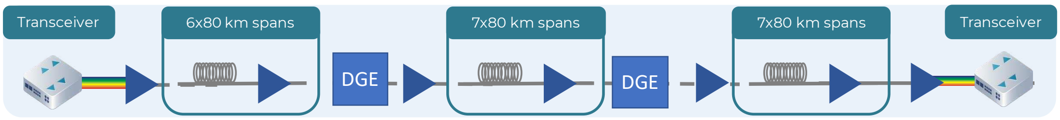

Fig. 3.2 Schematic of the experimental set up.

for each span. After the 6-th and 13-th spans two dynamic gain equalizers (DGEs) are used to equalize the spectrum, compensating for ripples due to the amplification process and for residual tilt caused by the SRS.

3.1.1 Multi-Vendor, Flex-grid and Flex-rate Transmission Scenario

In this analysis, the analysis performed in [78] is extended by considering 8 multi-vendor TRXs, with symbol rates ranging from 33 to 69 Gbaud, TRX constellations of QPSK, 8-QAM and PCS-16-QAM, for data rates ranging from 100 Gbit/s up to 300 Gbit/s, along with a flex-grid WDM configurations with channel spacing of 50 and 75 GHz. This experimental transmission has been performed upon a bandwidth of 3 THz in the C-band, with the remaining spectrum aside from these TRXs fully loaded with standard 100 Gbps channels. The experimental results are presented along with those corresponding to the GNPy model, including estimations for the interval of confidence, showing that the QoT prediction given by GNPy has an average error value that does not exceed 0.5 dB for every considered TRX. Besides confirming the reliability of GNPy as a vendor-neutral software model for WDM optical transport, it is shown that the optimal management of flex-grid flex-rate OLSs is enabled by managing Power Spectral Density (PSD) instead of power per channel, P_λ, as is used in fixed-grid management. This approach has been previously suggested and investigated for flex-grid transmission scenarios in [80, 81].

Table 3.1 The *adjacent* and *far apart* spectral configurations: 75 GHz and 300 GHz spacing between the 62 and 69 Gbaud carriers, respectively. These carriers are shown in bold and the loading comb is shown in italics.

adjacent spectral configuration								
f_0	*192.55–192.9*	192.975	193.05	193.125	**193.2**	**193.275**	193.35, 193.4, 193.45	*193.55–195.45*
N_{ch}	*8*	1	1	1	**1**	**1**	3	*39*
R_s [Gbaud]	*33*	33	33	44	**62**	**69**	39	*33*
M	*QPSK*	QPSK	QPSK	8-QAM	**16-QAM PCS**	**QPSK**	16-QAM PCS	*QPSK*
R_b [Gbit/s]	*100*	100	100	200	**300**	**200**	200	*100*

far apart spectral configuration								
f_0	*192.55–192.9*	**192.975**	193.05	193.125	193.2	**193.275**	193.35, 193.4, 193.45	*193.55–195.45*
N_{ch}	*8*	**1**	1	1	1	**1**	3	*39*
R_s [Gbaud]	*33*	**62**	33	44	33	**69**	39	*33*
M	*QPSK*	**16-QAM PCS**	QPSK	8-QAM	QPSK	**QPSK**	16-QAM PCS	*QPSK*
R_b [Gbit/s]	*100*	**300**	100	200	100	**200**	200	*100*

Regarding transmission, two different spectra have been propagated and analysed, for a total bandwidth that occupies a portion of the C-band located between 192.55 THz (1556.96 nm) and 195.45 THz (1533.86 nm). In both cases, a total of 55 channels organized in a flexible WDM grid with a minimum division of 12.5 GHz is considered. The overall bandwidth, along with the distinct propagated channels, can be schematically divided in two sub-regions:

- A 50 Hz fixed-grid loading comb composed of 47 QPSK-modulated 100 Gbit/s channels with symbol rates of 28 and 33 Gbaud;
- A sub-region of interest located between 192.95 THz (1553.73 nm) and 193.45 THz (1549.48 nm) that includes a total of 8 CUTs:
    - two QPSK 100 Gbit/s channels with symbol rates of 33 Gbaud;
    - three 16-QAM 200 Gbit/s channels with symbol rates of 39 Gbaud;
    - one 8-QAM 200 Gbit/s channel with a symbol rate of 44 Gbaud;
    - one 16-QAM 300 Gbit/s channel with a symbol rate of 62 Gbaud;
    - one QPSK 200 Gbit/s channel with a symbol rate of 69 Gbaud.

For this experimental investigation, the loading comb and two distinct TRX spectral combinations have been multiplexed using a WSS to create two distinct spectral configurations.

The two spectra are referred as the *adjacent* and *far apart* spectral configurations, described in detail in Tab. 3.1. The main difference between the two analysed spectra is that the two CUTs with the larger symbol rates, 62 and 69 Gbaud, are placed next to each other or with other CUTs between them; Fig. 3.3 includes a visual representation of these two configurations. Two configurations have been chosen in order to observe any variation upon the GSNRs within the spectral region of interest when the channels with the largest symbol rates change spectral occupations. If GSNR variations are present, they must be taken into account by the OLS controller when optimizing the configuration of the channels with respect to their symbol rates.

Both spectra have been transmitted at various launch powers and, at the OLS termination, the CUTs have been demultiplexed with a Finisar WaveShaper 4000S and then received, allowing QoT analysis. In particular, the launch powers for each channel have been set such that an approximately uniform PSD is attained over the

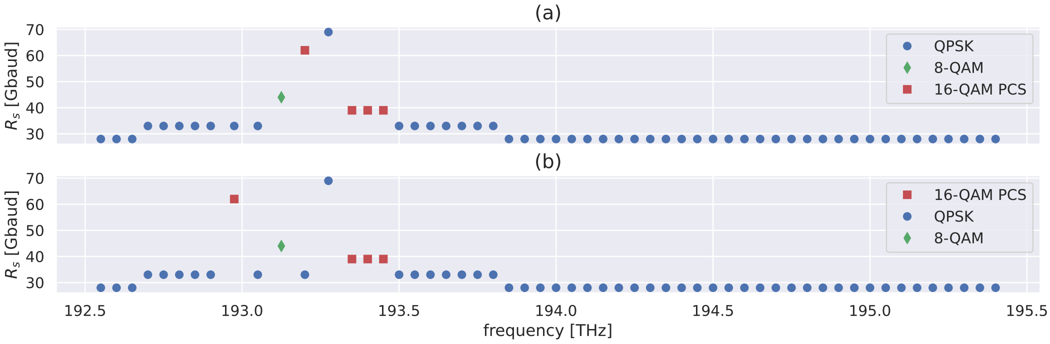

Fig. 3.3 Visualization of the (a) *adjacent* and (b) *far apart* spectral configurations, as fully described in Tab. 3.1.

entire bandwidth; this is performed by maintaining the ratio between the launch powers of any couple of distinct channels equal to the ratio between their symbol rates, which is also visible in Fig. 3.3. In order to observe the GSNR variation as the optimal power level is approached, this uniform PSD condition is retained and power sweep power sweep performed, varying the equivalent power per channel, $\overline{P}_\lambda$, between -2 and 2 dBm in 0.5dB increments, where $\overline{P}_\lambda$ is defined as the total signal power divided by the total number of channels.

In this framework, for each transmitted signal, the BER is measured at the receiver and the OSNR at the OLS termination for each TRX. In particular, the OSNR values are obtained from two distinct signal power measurements and the ASE noise after the last EDFA. The ASE noise power has been measured by switching off each TRX in turn and then evaluating the noise floor within the relative bandwidth. Both of these power measurements have been performed using a MS9740A Anritsu optical spectrum analyzer (OSA) in Fig. 3.4 an example of the transmitted signal power is shown.

In order to compare the performance of the CUTs to the predictions given by GNPy, the measured BERs have to be converted to GSNR values. This conversion also has the benefit of decorrelating the measurements to the specific characteristics of each distinct TRX. Furthermore, it enables a direct analysis of the relation between the QoT and the physical layer features of the investigated system and is crucial in enabling the network orchestrator to perform an optimal symbol rate and modulation format setting.

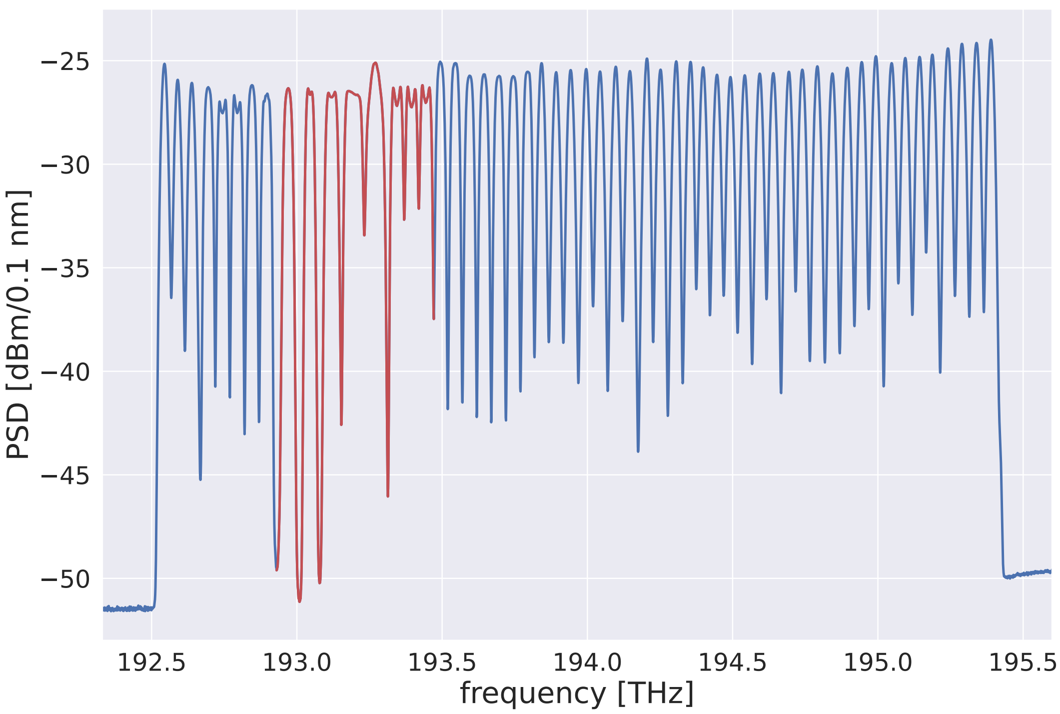

Fig. 3.4 Optical spectrum at the OLS input; the spectral region of interest where the CUTs are located is highlighted in red.

The first required step to convert from BER to GSNR is the B2B characterization of every TRX, as shown in Sec. 2.1. These B2B characterizations have been performed by measuring the BER and the OSNR (which, in this case, is equal to the GSNR) with an increasing level of ASE noise loading. In Fig. 3.5, the theoretical expectations for the different modulation formats are compared with the measured B2B characterizations. As anticipated in Sec.1.2, the detachment between the theoretical and measured curves is due to additional implementation-specific degradations that are not related to the lightpath QoT. As in Sec. 2.1, it can be observed that the B2B characterizations of the 16-QAM-PCS-modulated channels behave the same as the 8-QAM-modulated channel, as their constellation is reshaped into an equivalent 8-QAM modulation format. It is wort noting that the GSNR is expressed by considering the entire channel bandwidths as noise reference bandwidths, rather than a 0.1 nm bandwidth.

At this stage, as the *pre*-FEC BER is a parameter provided by the TRXs, which are commercial devices with limited access to the internal DSP unit, it has not been possible to properly estimate the error on the BER measurements and the

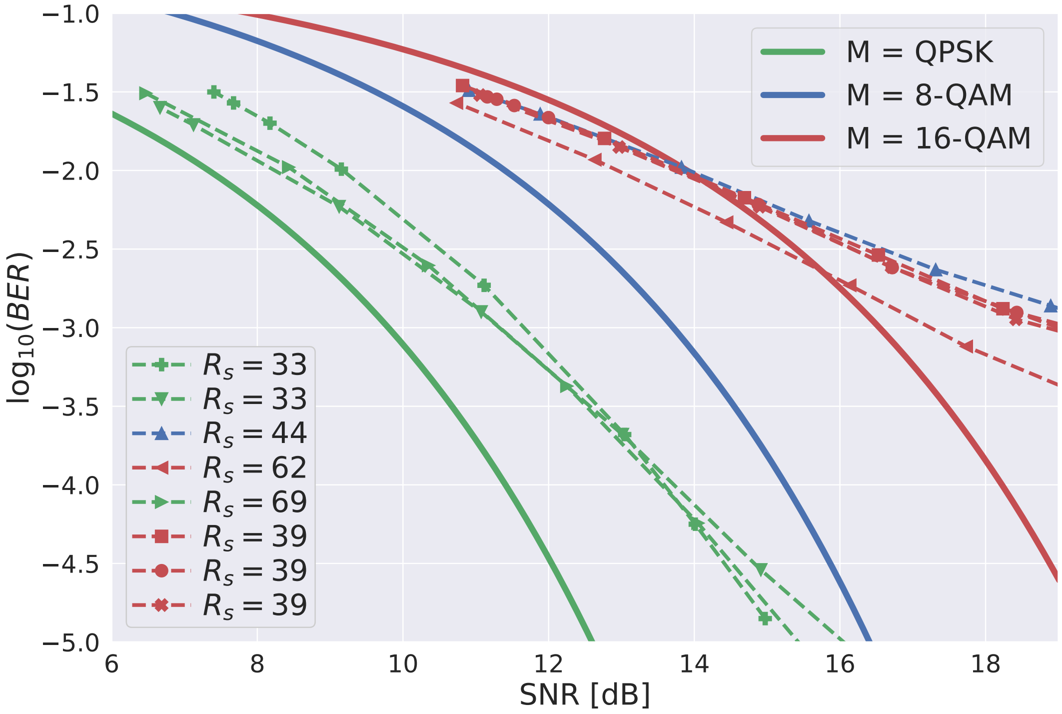

Fig. 3.5 Back-to-back characterization for each distinct channel within this experimental campaign; continuous and dashed lines represent the theoretical and measured back-to-back curves, respectively. The channel symbol rates, R_s, are given in Gbaud

consequent confidence interval in GSNR conversions. Properly estimating this quantity would allow a more precise analysis of the QoT investigation with a more accurate description of the system margin and will be the focus of further studies. In order to reasonably quantify the inaccuracies related to the indirect measurement of the GSNR, it is assumed an error corresponding to a rigid shift in the OSNR measurements up to a maximum ± 0.2 dB, providing a confidence interval, ε, of the derived GSNR values.

Following this B2B characterization for each TRX, the BER measurements can be directly converted to GSNR values and compared to the predictions provided by GNPy. Furthermore, the OSNR measurements obtained by the ASE provide an indirect evaluation of the SNR $_{\mathrm{NL}}$ degradation, as a subtraction estimate:

$$\mathrm{SNR}_{\mathrm{NL}} = \left(\frac{1}{\mathrm{GSNR}} - \frac{1}{\mathrm{OSNR}}\right)^{-1},$$

providing a deeper insight in the QoT estimation analysis. A schematic of this procedure applied to a specific TRX is shown in Fig. 3.6

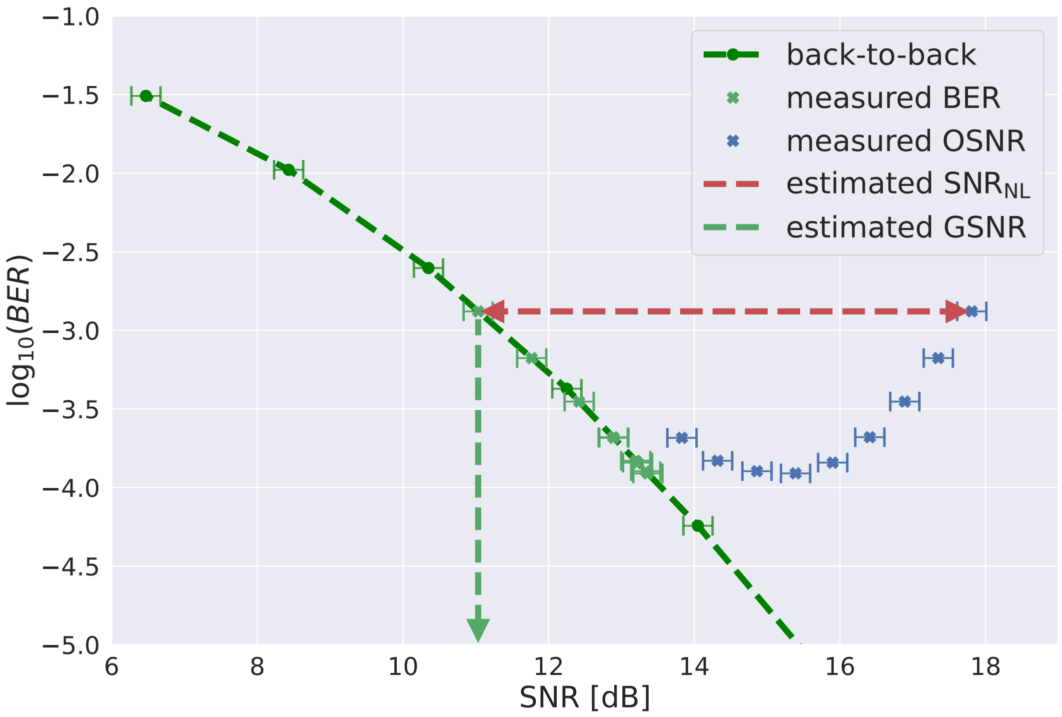

Fig. 3.6 Schematic of the GSNR and $\mathrm{SNR}_{\mathrm{NL}}$ evaluation procedure using the values for back-to-back characterization, measured BER and OSNR for the 69 Gbaud CUT.

At the time of this experiment, GNPy has been modified in order to allow variable WDM grid spacings and variable channel settings, such as channel-dependent input powers and symbol rates; these changes are now integrated in the lates version of GNPy. Moreover, leveraging the spectrally disaggregated structure of GNPy, the NLI estimator have been improved including a variable accumulation coefficient of the self-phase modulation component of the NLI, taking into account the span-by-span coherency dependence upon fiber variety and spectral characteristics [82]. These improvements allow the GNPy engine to adequately simulate the investigated experimental testbed that includes the propagation of flex-grid flex-rate spectral configurations. In general, the generalized GGN model implemented in GNPy provides accurate results when a precise evaluation of the physical layer parameters is available, as it has been extensively shown in previous fixed-grid experiments [83–85]. For the experimental setup under investigation some physical parameters involve a certain level of uncertainty, or are completely unknown. Among these variables,

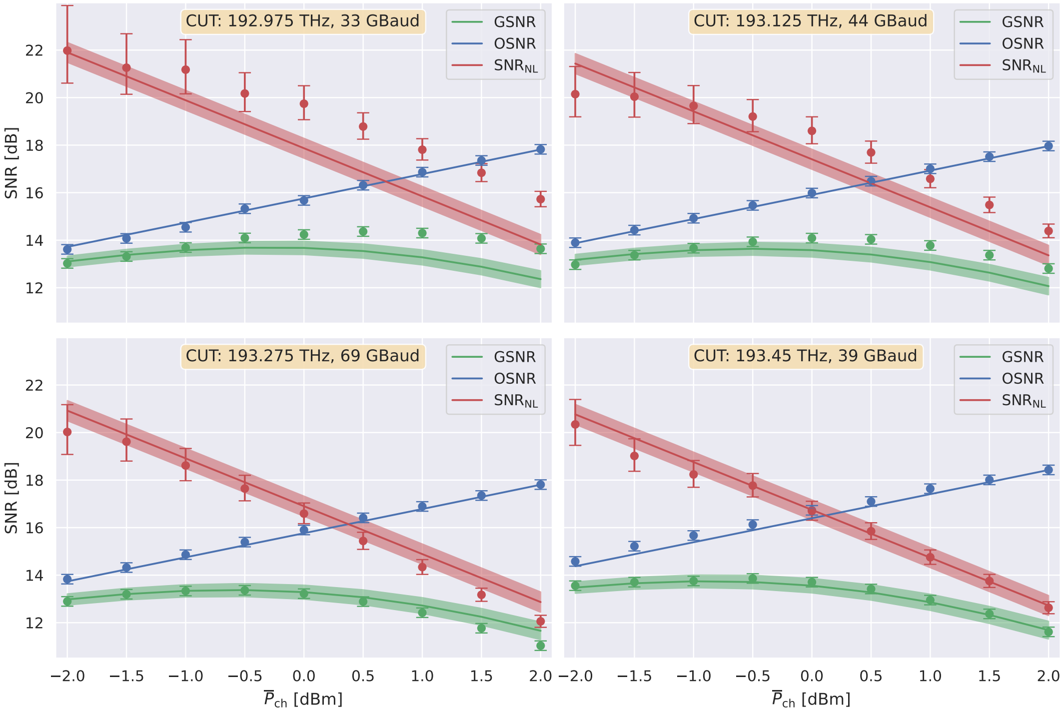

Fig. 3.7 The dots and the continuous lines represent, respectively, the measured and predicted GSNRs, OSNRs and SNR_{NL}s for 4 selected CUTs in the *adjacent* spectral configuration case, for every explored $\overline{P}_{\lambda}$ value. The shaded areas include the confidence interval obtained with the *upper* and *lower* simulations involving the extreme values of the input connector loss.

the EDFA NF and the fiber input connector losses, l_c, for each span are fundamental for an accurate system simulation to be achieved. In particular, the former quantity is necessary for an adequate prediction of the OSNR, whereas the input connector loss crucially affects the actual amount of power that is propagated through the fiber; both the SRS power tilt and the generated NLI noise strongly depend on the input power [85]. The EDFA NF for each span has been estimated from a single measurement of the OSNR at the OLS termination, with the total launch power set such that $\overline{P}_\lambda = 2\,\text{dBm}$. These measurements can be converted to an equivalent NF that has been equally redistributed for each span and also partially includes effects due to EDFA ripple. Regarding l_c, it is not possible to directly measure or estimate this value from an overall system metric in the same way as performed for the NF. Therefore, to accommodate uncertainty due to these unknown input connector loss values, a confidence interval of 0.25 ± 0.25 dB is considered for each span for the SNR $_{\text{NL}}$ and GSNR predictions. The GNPy simulations are then repeated with 0 and 0.5 dB connector loss values, and addressed as *lower* and *upper* extreme simulation cases, respectively.

The results obtained using these estimations are compared to the measured *pre*-FEC BER converted to the GSNR, along with the measured OSNR and the SNR $_{\text{NL}}$ obtained by subtraction of the inverse GSNR and OSNR. These results are shown in Fig. 3.7 for a subset of the CUTs: the best and the worst case scenario CUTs in terms of average GSNR prediction accuracy, and the CUTs with symbol rates of 44 and 69 Gbaud are included. In general, the GNPy engine provides very accurate predictions of the OSNR for all CUTs and launch powers explored in the power sweep. As expected, the generalized GN model implemented in GNPy provides conservative SNR $_{\text{NL}}$ predictions for almost all CUTs and $\overline{P}_\lambda$ values. Remarkably, by increasing $\overline{P}_\lambda$, the predicted and measured SNR $_{\text{NL}}$ values for all cases monotonically decrease and reach the same asymptotic slope, which demonstrates that the model under investigation provides a good representation of the underlying physical phenomena. On the other hand, the SNR $_{\text{NL}}$ measurements follow this trend less consistently at low $\overline{P}_\lambda$ values. Nevertheless, these deviations from the trend can be justified bearing in mind that the SNR $_{\text{NL}}$ measurements have been obtained by means of Eq. 1.3. As a consequence, the measured SNR $_{\text{NL}}$ includes also all the additional SNR degradations that are not included in the system abstraction. Therefore, this deviation can be explained by a constant additional degradation that is more evident at large SNR $_{\text{NL}}$ values and becomes negligible as the NLI increases. Furthermore, it can be observed that the the SNR $_{\mathrm{NL}}$ predictions for the TRX with the highest symbol rate, 69 Gbaud, are slightly optimistic for all $\overline{P}_\lambda$ values. This is due to this particular TRX having a received power that is below the optimal TRX power range.

To summarize, GNPy provides a conservative prediction with a satisfactory level of accuracy of the total GSNR for every CUT, for all $\overline{P}_\lambda$ values explored in the power sweep, with the exception of the 69 Gbaud channel, which suffers from additional impairments due to an insufficient received power. A quantitative estimation of the prediction accuracy can be obtained by inspecting the mean, μ, and root mean square (RMS), σ, of the errors in the GSNR simulations, ΔGSNR, defined explicitly in the following expressions:

$$\begin{aligned}
\Delta\mathrm{GSNR} &= \mathrm{GSNR}^{\mathrm{meas}} - \mathrm{GSNR}^{\mathrm{pred}}\Big|_{l_c=0.25} ;\\
\Delta\mathrm{GSNR}_{lower} &= \mathrm{GSNR}^{\mathrm{meas}} - \mathrm{GSNR}^{\mathrm{pred}}\Big|_{l_c=0} ;\\
\Delta\mathrm{GSNR}_{upper} &= \mathrm{GSNR}^{\mathrm{meas}} - \mathrm{GSNR}^{\mathrm{pred}}\Big|_{l_c=0.5} .
\end{aligned}$$

Both μ and σ are evaluated separately on the *adjacent* and *far apart* spectral configurations as:

$$\begin{aligned}
\mu &= \langle \Delta\mathrm{GSNR} \rangle , && (3.1)\\
\mu_{lower} &= \langle \Delta\mathrm{GSNR}_{lower} \rangle , \\
\mu_{upper} &= \left\langle \Delta\mathrm{GSNR}_{upper} \right\rangle ; \\
\sigma &= \sqrt{\left\langle (\Delta\mathrm{GSNR})^2 \right\rangle} , && (3.2)\\
\sigma_{lower} &= \sqrt{\left\langle (\Delta\mathrm{GSNR}_{\mathrm{lower}})^2 \right\rangle} , \\
\sigma_{upper} &= \sqrt{\left\langle \left(\Delta\mathrm{GSNR}_{\mathrm{upper}}\right)^2 \right\rangle} ;
\end{aligned}$$

where the operator $\langle \cdots \rangle$ represents the average over the entire set of measurements/predictions. These results are reported in Tab. 3.2, along with the minimum ΔGSNR, which represent the worst-case scenario; here, GNPy provides a non conservative prediction, which also provides a rough estimation of the required QoT margin. Moreover, the uncertainties, ε, reported in Tab. 3.2 have been calculated as

Table 3.2 Overall GNPy accuracy defined by means of μ, σ and the minimum value of the GSNR error, ΔGSNR. These results include both spectral configurations and the simulation extremes with respect to input connector losses. Uncertainties, $\pm\varepsilon$, are provided for all values.

	adjacent	*far apart*
μ	0.2 ± 0.2 dB	0.1 ± 0.2 dB
σ	0.4 ± 0.1 dB	0.3 ± 0.1 dB
min(ΔGSNR)	-0.6 ± 0.9 dB	-0.8 ± 0.9 dB
μ_{lower}	0.4 ± 0.2 dB	0.3 ± 0.2 dB
σ_{lower}	0.6 ± 0.1 dB	0.5 ± 0.1 dB
min($\Delta\mathrm{GSNR}_{lower}$)	-0.3 ± 0.9 dB	-0.5 ± 0.9 dB
μ_{upper}	0.1 ± 0.2 dB	-0.1 ± 0.2 dB
σ_{upper}	0.3 ± 0.1 dB	0.3 ± 0.1 dB
min($\Delta\mathrm{GSNR}_{upper}$)	-0.9 ± 0.9 dB	-1.1 ± 0.9 dB

follows:

$$\begin{aligned}
\varepsilon_{\min} &= \varepsilon_{\min(\mathrm{GSNR}^{meas})}\,; \\
\varepsilon_{\mu} &= \sqrt{\left\langle \left(\varepsilon_{\mathrm{GSNR}^{meas}}\right)^2 \right\rangle} \quad , \\
\varepsilon_{\sigma} &= \frac{1}{\sigma}\sqrt{\frac{1}{N}\left\langle \left(\Delta\mathrm{GSNR}^{meas}\cdot\varepsilon_{\mathrm{GSNR}^{meas}}\right)^2 \right\rangle}\,,
\end{aligned}$$

where N is the total number of measurements/predictions.

In general, GNPy provides very accurate (low value of σ) and unbiased (low value of μ) predictions, with the *upper* simulation providing the most precise estimations. On the other hand, the *lower* simulation provides a more reliable estimation, as the GSNR error on the worst-case scenario is more than halved with respect to the other simulations. These two simulations represent scenarios where either a more accurate or more reliable model may be chosen, depending upon the requirements of the network operator.

These results can be further analyzed from an application standpoint by investigating the optimal launch power and GSNR feasibility when higher-cardinality modulation formats are used. In general, the optimal launch power is an implementation-dependent quantity and can be described with different definitions. However, a per-channel power optimization is not straightforward due to the nonlinear effects (both the SRS and NLI) that are generated during fiber propagation. Managing the

NLI impairment can be simplified by considering the following heuristic idea: the NLI noise generated by the signal power contained in an infinitesimal bandwidth of an interfering channel does not depend upon the channel itself. E.g., the NLI generated by two interfering channels with symbol rates of 33 Gbaud is not significantly different from the NLI generated by one interfering channel with a 66 Gbaud symbol rate, if each of these channels occupy the same frequency slot width.

In a realistic use case, the optimal launch power can therefore be defined globally, where an optimization algorithm varies the offset and tilt of a uniform PSD configuration over the entire transmitted spectrum. This constant PSD configuration can then be tilted in order to recover the residual tilt due to uncompensated SRS. Defining a global optimal launch power using this uniform PSD leads to a uniform GSNR distribution for all channels; this reduces management complexity and allows system margins to be kept under control. It is worth underling that the optimization procedure used within this work does not require any additional equipment, as the optimal launch power configuration can be obtained by varying the EDFA gains (or output power) and tilts, which are parameters that are readily accessible in currently deployed infrastructures.

Additionally, it is worth underling that a more elaborate PSD distribution which takes into account all symbol rate variances within the spectrum can provide a better optimization, however in this analysis the priority is maintaining a lower level of complexity for ease of optimization management in a realistic use case.

In this work an analysis on the optimal launch power can only partially be performed, as the CUTs occupy a limited portion of the entire spectrum bandwidth. To define the optimal launch power, first it has to be considered that $\overline{P}_\lambda$ is defined as the total signal power divided by the total number of channels. Secondly, distinct $\overline{P}_\lambda$ values represent different power sweep measurements, and a uniform PSD over the entire bandwidth has been retained for all of these measurements. Bearing these details in mind, the optimal value of $\overline{P}_\lambda$ within the investigated range is defined as the optimal launch power. The definition of the optimal $\overline{P}_\lambda$ value is not straightforward, as distinct CUTs reach their maximum measured GSNR at different $\overline{P}_\lambda$ values (the same is true considering predicted GSNRs). Considering these individual optimal $\overline{P}_\lambda$ values for each CUT, the minimum to be the overall optimal $\overline{P}_\lambda$ is selected, ensuring that all channels do not exceed their own optimal values. Given this definition, the optimal launch power for both spectral configurations is $\overline{P}_\lambda =$ -0.5 dBm and $\overline{P}_\lambda =$

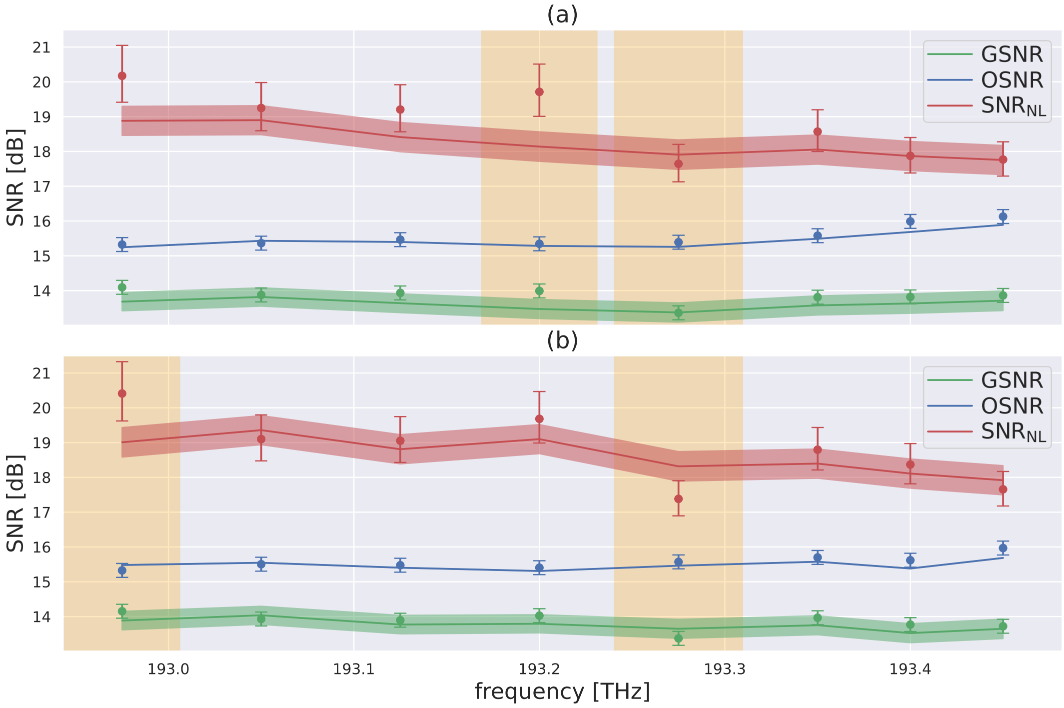

Fig. 3.8 The dots and the continuous lines represent, respectively, the measured and predicted GSNR, OSNR and SNR$_{NL}$ for all CUTs. The top and the bottom report the results for the (a) *adjacent* and (b) *far apart* spectral configurations, at the optimal measured working point $\overline{P}_\lambda = -0.5$ dBm. The shaded horizontal areas include the confidence interval obtained with the *upper* and *lower* simulations involving the extreme values of the input connector loss. The largest symbol rate CUTs, 62 and 69 Gbaud, are highlighted with the vertical yellow shades on the left- and right-hand sides respectively.

-1 dBm, considering the set of measured and predicted GSNRs, respectively. From an application standpoint, GNPy provides a sub-optimal launch power that results in a limited reduction in the achieved GSNR – this can be quantified as the RMS deviation between the measured GSNR at $\overline{P}_\lambda =$ -1 dBm and the maximum measured GSNR for each channel; for both investigated spectral configurations this metric is equal to 0.3 ± 0.1 dB.

Lastly, the comparison of the measured and predicted values of GSNR, OSNR and SNR $_{NL}$ for all CUTs is shown in Fig. 3.8 for $\overline{P}_\lambda =$ -0.5 dBm. It is visible that the flat GSNR assumption is verified in this case, as the GSNR standard deviation for all channels is 0.2 ± 0.1 dB for both spectral configurations. As previously mentioned, the CUT with the highest symbol rate, highlighted in yellow on the the right-hand in Fig. 3.8, appears to experience an additional penalty that is not included in the simulation abstraction; for all other CUTs, GNPy provides a conservative estimation of the SNR $_{\mathrm{NL}}$, which leads to an accurate GSNR prediction.

Moreover, the GSNR values do not vary significantly, with a RMS deviation of 0.1 ± 0.1 dB, when the CUT with symbol rate of 62 Gbaud is moved from the center to the edge of the sub-region of interest. This result is very important from an application standpoint as it suggests that the relative position of the large and narrow CUTs in a flex-rate framework is not significant when a constant PSD is implemented; consequently, system management and the optimization performed by the optical line controller is further simplified. It is worth noting that this observation can be combined with the results of [86] to consider an optimal system working point which provides a flat and uniform GSNR distribution over the entire C-band.

3.1.2 Nyquist Subcarriers Flexible Transmission up to 800 G

For the first time, GNPy predictions for Nyquist subcarrier transponders are experimentally validated at bit rate, R_b, up to 800 Gbit/s and symbol rate, R_s, up to 96 Gbaud, operated at full flex-grid WDM spectral load on the C-band. Results show an excellent accuracy of GNPy computation, both in predicting performance and optimal power per channel, confirming its reliability in abstracting the optical transport also in flex-grid mixed-technologies scenarios up to 800 Gbit/s per wavelength. Additionally, GNPy provides a reliable estimation of the maximum reach for the different bit rates under investigation. In this study, all the results are expressed by means of SNR variations, ΔSNR, with respect to an unrevealed reference in order to avoid any disclosure issues.

A total of 42 channels have been considered within this experimental framework. These channels have been organized in a flexible WDM grid with a minimum division of 6.25 GHz located between 192.55 THz and 194.9 THz within the C-band; a detailed description of the spectrum is reported in Table 3.3. The TRX, centred at 193.125 THz, has been transmitted with R_b from 400 up to 800 Gbit/s, with step of 100 Gbit/s. The TRX consist of 8 Nyquist subcarriers multiplexed (SCM), each working at 64-QAM PCS and data baud rate up to 12 Gbaud. This yields an equivalent total channel bandwidth, B_λ, up to 96 GHz. An example of the transmitted signal measured by a MS9740B Anritsu ASE is shown in Fig. 3.9.

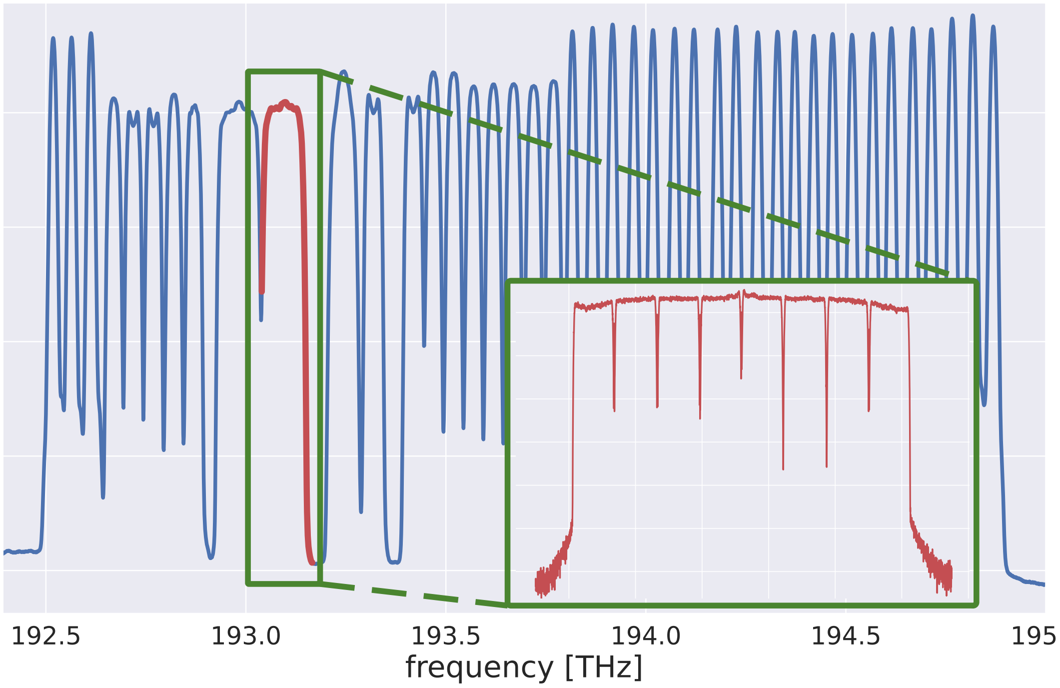

Fig. 3.9 800 Gbit/s - 96 Gbaud spectrum of the channel under test.

Δf [THz]	192.55-192.65	192.7-192.9	193.013-193.125	193.275	193.35-193.55	193.6-193.8	193.85-194.9
N_{ch}	3	5	2	1	4	5	22
R_b [Gbit/s]	100	100	up to 800	200	200	100	100
R_s [GBaud]	28	33	91/96 *	69	39	33	28
M	QPSK	QPSK	64-QAM PCS **	QPSK	16-QAM PCS	QPSK	QPSK

Table 3.3 Detail description of the transmitted spectrum. The spectrum is subdivided in terms of the occupied frequency interval, Δf, the number of channels, N_{ch}, the bit rate, R_b, the symbol rate, R_s, and the modulation format, M.

* it is an aggregated baud rate of the 8 sub channels working up to 12 GBaud individually.

** the individual modulation scheme per sub-channel were not recorded.

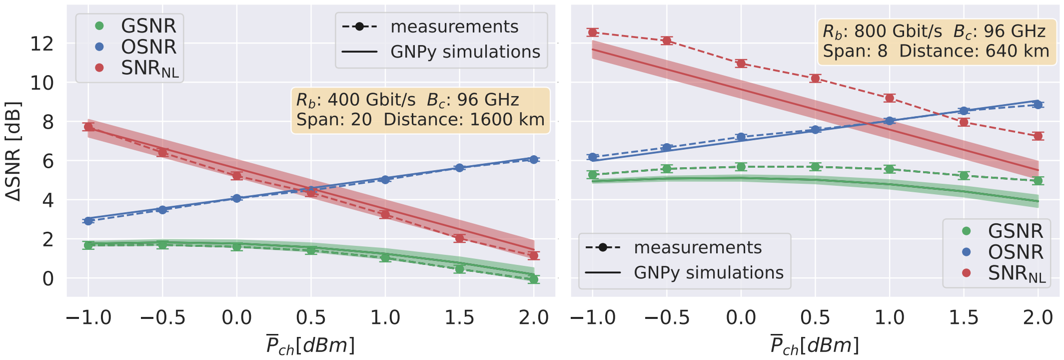

Fig. 3.10 Power sweeps for two selected bit rates. The shaded area surrounding the solid lines represents the variation of the GSNR and SNR_{NL} predictions varying the connector loss within a 0.5 dB range.

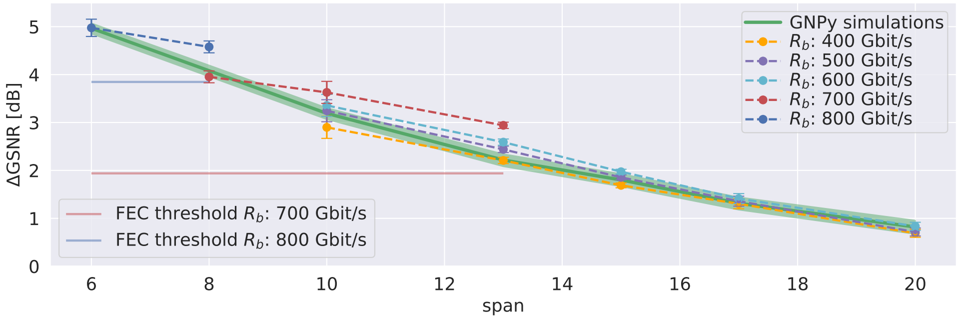

Fig. 3.11 Measured and simulated GSNR at different receiving distances for all the investigated bit rates. The FEC thresholds of the R_b lower than 700 Gbit are not shown in the figure as they are not significant being lower than the minimum GSNR reached after 20 spans of transmission.

This extensive experimental campaign encompassed the measurement of GSNRs and OSNRs, evaluated over the entire B_c, of the TRX operated at 400 up to 800 Gbit/s. In particular, the transmitted signal has been received at different distances along the entire OLS, depending on the R_b, between 6 and 20 crossed spans, which correspond to 480 up to 1600 km. For each R_b and receiving distance, the launch power at the input of the OLS has been varied in order to obtain an estimation of the optimal power.

In this investigation, the Nyquist subcarrier TRX has been simulated in GNPy as a single carrier with a symbol rate equivalent to the total TRX B_λ. Furthermore, the input connector loss at each fiber span has been set equal to a reference value of 0.25 dB, and all the simulations have been repeated varying this value between

0.00 and 0.50 dB in order to obtain an estimation of the interval of confidence of the GNPy predictions.

In Fig. 3.10, measurements and GNPy predictions are compared for the 400 and 800 Gbit/s transmission, at the $20-th$ and $8-th$ span, respectively. It can be observed that GNPy functions as a reliable QoT estimator for the investigated system for all the $\overline{P}_{ch}$ values, providing an adequate prediction of the GSNR and, in particular, of both its components, the OSNR and the SNR_{NL}, allowing an accurate prediction of the optimal power. The larger error obtained in the 800 Gbit case is due to a non-negligible difference between the actual and nominal TRX power at the specific span. It is worth to highlight that this discrepancy is not generated by an inaccuracy of the simulation but it rather provides an estimation of the system QoT fluctuations due to spectrum variations occurring in distinct measurements, mainly due to the equalization procedures. This behaviour can be further observed in Fig. 3.11, where the GSNR predictions and measurements are compared for all the considered R_s and receiving spans, for a fixed value of $\overline{P}_{ch} = -0.5\,\text{dBm}$. Theoretically, all the GSNR measurements should lie on the same curve, span-by-span, as this quantity does not depend on the symbol rate nor the modulation format. On the contrary, these measurements vary in a range of 1 dB depending on the R_b and the receiving span; this range is completely compatible with the error observed in GNPy predictions.

In general, Fig. 3.11 shows an excellent accuracy and reliability of GNPy in simulating the QoT along the entire OLS and for all the investigated R_b, also providing a precise prediction of the maximum reach for the distinct R_b.

3.1.3 An Experimental Observation of the Disaggregated Nonlinear Interference Noise Generation

Employing an investigation similar to [87], the spectrally disaggregated approach to the NLI evaluation implemented in GNPy is experimentally validated by measuring the cross-channel NLI contributions. Within a flex-grid, flex-rate spectrum including commercial multi-vendor channels at R_s from 33 up to 90 Gbaud propagating over a multi-span amplified line, the BER performance variations of a TRX are measured when selectively side-channels are switched off. Finally, GSNR values are derived from the BERs using the B2B TRX characterization and results are compared to the GNPy prediction, showing an excellent accuracy in the GNPy disaggregated computation of the cross-channel NLI components.

Regarding transmission, the spectrum used for carrying out the experiments is made of various industrial transponders from different vendors, and of padding channels made from an ASE noise source and shaped by a wavelength selective switch, Tab. 3.3. The transmitted spectrum is located in the C-band, and ranges from 192.1750 to 195.0250 THz. A total of 17 transponders and 24 ASE-based padding channels is considered and organized in a flexible WDM grid with a minimum division of 12.5 GHz, for a total of N_{ch} =41 transmitted channels. The launch power has been set such that an approximately uniform power spectral density is attained over the entire bandwidth. At the receiver side, the TRX at 192.7625 THz is demultiplexed with a 1×9 Lumentum WaveShaper. Both the launched and received power per channel measurements have been performed using a MS9740B Anritsu optical spectrum analyzer.

In this investigation, the aim is to observe the NLI-related GSNR variations obtained turning off each interfering channels, in turns. The transmission GSNR at a certain span, n, can be written as follows:

$$GSNR^{(n)} = \left(\frac{P^{(n)}_{\text{ASE},\lambda} + P^{(n)}_{\text{NLI},\lambda}}{P^{(n)}_{\lambda}} \right)^{-1} , \tag{3.3}$$

and the NLI power can be disaggregated by means of the following expression:

$$P^{(n)}_{\text{NLI},\lambda} = \sum_{i}^{N_{ch}} \eta^{(n)}_{\lambda,i} P_\lambda P_i^2 , \tag{3.4}$$

where $\eta^{(n)}_{\lambda,i}$ represents the NLI efficiency, λ is the TRX index and P_i for $i \in [1, N_{ch}]$ are the interfering channel powers. Given Eq.3.3 and 3.4, it is clear that in order to observe an NLI-induced GSNR variation when an interfering channel, $i = j$, is turned off, i.e. $P_{i=j} = 0$, both $P^{(n)}_{\text{ASE}}$ and the remainder $P_{i \neq j}$ must remain stable. Bearing this consideration in mind, the spectrum is received after 13 spans and at an equivalent launch power per channel of 2 dBm, i.e. defined as total power over the number of channels, as a trade-off between having high NLI contributions (high values of n and P_i) and maintaining a limited amount of fluctuations (low values of n and P_i).

In this framework, after the B2B characterization of the TRX, the TRX BER values have been measured for 41 distinct transmitted spectrum configurations: the full spectral load case and the 40 configurations obtained switching off, in turn, each interfering channel. Additionally, the transmitted and received power of each channel have been measured in order to obtain a rough estimation of the power transfer matrix which allows to evaluate an approximated NLI accumulation factor, assuming that all the fiber spans are identical.

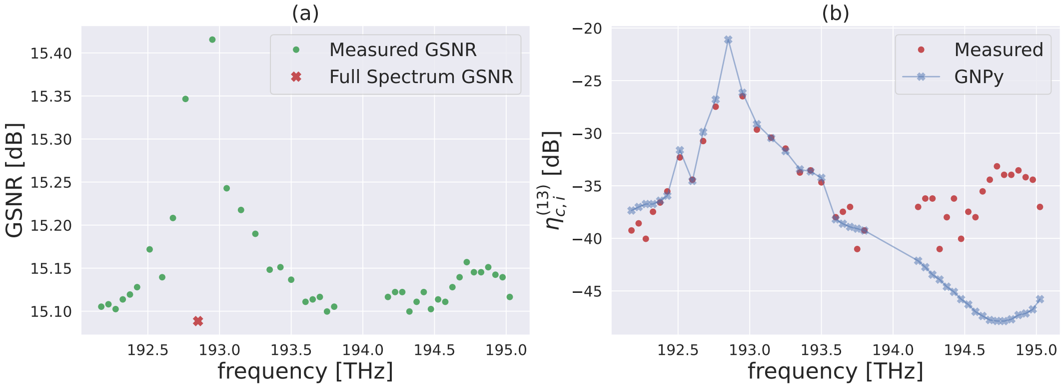

Fig. 3.12 (a) TRX measured GSNR values for all the propagated configurations, each frequency represents the channel that was turned off. At the TRX frequency, the red dot indicates the GSNR of the TRX measured at the full spectrum load. (b) Measured and simulated values of the distinct $\eta^{(13)}_{\lambda,i}$ terms of each interfering channel with the TRX, in red dots and blue dotted line respectively.

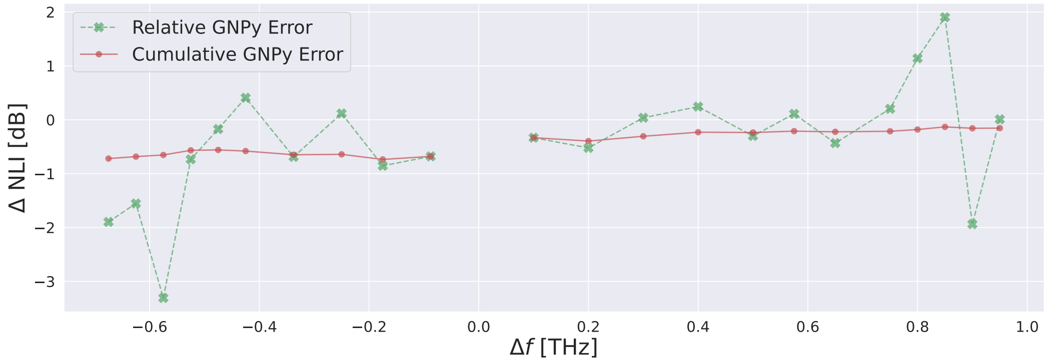

Fig. 3.13 Relative, considering separately each single interfering channel, and cumulative GNPy estimation error of the NLI contributions of the TRX neighboring interfering channels.

The estimated GSNR values derived from the TRX BER measurements for all the configurations of the propagated spectrum are shown in Fig. 3.12(a). In particular, at each frequency correspond the TRX GSNR value evaluated when the interfering channel centered in that specific frequency is turned off in the propagated spectrum, GSNR$_i$. Indeed, when the TRX itself is turned off, the GSNR measurement is meaningless and at the TRX central frequency in Fig. 3.12(a) it has been placed the TRX GSNR value evaluated when the full spectral load configuration is propagated, GSNR$_{full}$. As mentioned in the previous section, the entire experimental campaign has been performed such that the main variations observed in TRX GSNR measurements for distinct propagated spectrum configurations can be attributed to the variations of the NLI contributions to the overall TRX impairment. As expected, it can be observed that the full spectrum configuration results in the worst TRX GSNR measurement, as all the interfering channel are contributing to the overall NLI noise in this scenario. Moreover, the TRX GSNR increases when the interfering channel are switched off, in turn, with a GSNR increment that decays as the frequency distance between the TRX and the switched off interfering channel progressively increases. It is worth to notice that when the channels beyond the frequency gap at 194.0 THz are switched off, the measured TRX GSNR experiences an unexpected behaviour. In fact, increasing the frequency distance the contribution to the NLI impairment of an interfering channel continues to abate reaching a negligible value, roughly approached by the extreme channels before the frequency gap, with respect to the NLI contributions of the TRX neighboring interfering channels. Therefore, the TRX GSNR should continue to decrease approaching GSNR$_{full}$. In light of these considerations, it can be deduced that the TRX GSNR variations measured when the channels beyond the frequency gap are turned off are related with EDFAs-induces P_i and $P_{\text{ASE};\lambda}$ fluctuations. This hypothesis can be corroborated highlighting that these channels lays in the spectral hole burning frequency neighborhood.

In order to quantify the TRX GSNR variations in terms of NLI contributions, assuming the TRX $P_{\text{ASE};\lambda}$ and $P_{i\neq j}$ are constants, from Eq.3.3 and Eq. 3.4 the following expression is obtained:

$$\eta_{\lambda,i}^{(13)} = \frac{\text{GSNR}_{full}^{-1} - \text{GSNR}_i^{-1}}{P_i^2} K^{(13)} , \tag{3.5}$$

where $K^{(13)}$ is an accumulation factor calculated assuming that the NLI impairment introduced by each fiber is constant. Fig.3.12(b) reports both the evaluated $\eta_{\lambda,i}^{(13)}$ from the measured GSNR$_i$, by means of Eq.3.5, and the $\eta_{\lambda,i}^{(13)}$ obtained using the open-source library GNPy[28, 41], which includes a disaggregated implementation of the GN model, where the SC and XC components of the NLI noise are calculated separately. It can be observed that the disaggregated simulation provides very accurate prediction when the GSNR variations are strictly related to NLI variations induced by the spectral load modifications.

In order to quantify this accuracy, the interfering channels before the frequency gap at 194.0 THz are considered at first. As shown in Fig. 3.13, the GNPy estimation error absolute values of the separate NLI contributions increase approaching a frequency difference, Δf , of 1 THz between the TRX and the specific interfering channel; dashed green lines in Fig. 3.13. Nevertheless, the cumulative GNPy error, considering an increasing number of neighboring interfering channels with an increasing Δf, remains roughly constant around -0.65 and -0.25 dB considering the left-hand and right-hand sides, respectively, with regard to the TRX; continuous-circled red lines in Fig. 3.13. These metrics increase when considering interfering channels with an higher Δf; i.e. beyond the frequency gap at 194.0 THz. These variations do not contribute significantly to the overall NLI noise evaluation and the total simulated TRX XC-NLI noise, calculated as the sum of the NLI contributions of all the interfering channels, provides an accurate prediction with an error lower than 1 dB.

3.2 PDL Experimental Validation and Monte Carlo Analysis

PDL-induced polarization power fluctuations along the transmission have been statistically characterized for a limited or arbitrary number elements introducing PDL [76, 77], the effect of the PDL on the transmission performance has been reduced to an overall GSNR penalty that has to be included as an additional margin [88]. The interplay of the PDL and the transmission impairments produces a complex effect on the GSNR which may depend significantly on the optical system under consideration [89, 90]. In light of this consideration, a more accurate model of the PDL effect on the propagated spectrum can be investigated in order to obtain a case-specific evaluation of the PDL-induced quality of transmission penalty that can be included in a physical layer digital twin of the specific optical network. In order to further motivate the need of a more precise PDL model, in this section, an extensive simulation campaign is investigated observing the effect of the interaction between the PDL and the ASE noise in a specific use-case, showing that the accumulated PDL effect on the propagated signal is not enough to properly characterize the PDL-induced GSNR penalty. Recently, in a similar work, the effect of PDL on the SNR has been investigated on a sub-sea scenario using a numerical approach [91].

3.2.1 Metro Regional Scenario

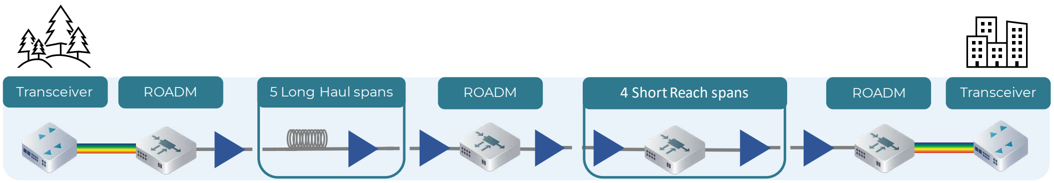

Fig. 3.14 Schematic of the investigated transmission scenario.

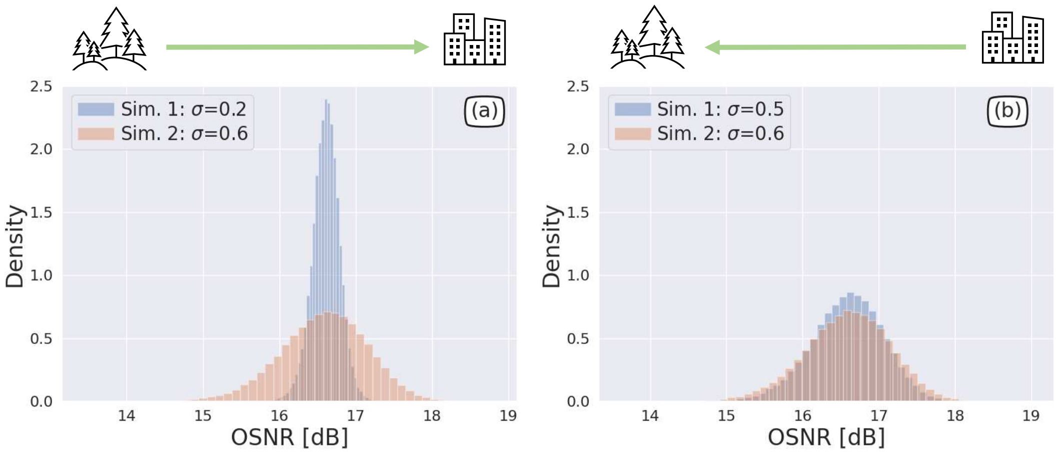

Fig. 3.15 Simulation results considering (a) the transmission in the rural-to-metro direction and (b) *vice versa*.

The specific transmission scenario investigated in this section consists of a network domain composed of two different subsystems, shown in Fig. 3.14:

- *Regional subsystem*: it is characterized by long distance fiber connections, a total length of 500 km, that result in a large amount of ASE noise due to the high loss, 20 dB per fiber span; on the contrary, the PDL generated in this section is relatively limited.

- *Metro subsystem*: in this network section a large number of ROADM, each one including two WSS, increases significantly the PDL computation while the ASE noise generation is limited by the low value of the interconnection fiber losses, 8 dB per fiber span.

In order to obtain a realistic simulation of the considered scenarios, a distinct value of NF for each EDFA type is set. In particular, the pre-amplifier and the in-line amplifiers in the rural area are set at 5 dB while the booster has a NF of 6.5 dB. Whereas, in the metro area NFs is 8.5 and 6.5 dB on the pre-amplifiers and booster, respectively. Finally, also the WSS PDL has been considered in a distinct manner in the two network sections; in the regional subsystem, where the signal ripple is expected to be significant, a WSS PDL distribution centered on an higher attenuation is considered, 10 dB with respect to the measurements presented in the previous section. On the contrary, in the metro area, the WSS PDL distribution is centered at 5 dB of attenuation.

In this framework, it has been carried out a Monte Carlo analysis of the transmission of a single channel in both directions, rural-to-metro and *vice versa*, with 10000 distinct simulations each. At each repetition of the propagation simulation, the PDL values of each element are extracted using the measured distribution. During the propagation, random polarization scramble matrices are applied to the signal between each element and the loss/gain balance is assumed to be unitary.

Fig. 3.15 illustrates the simulation results obtained for the transmission in both directions over all the simulated cases. The simulated OSNR have been evaluated with two distinct approach: In Simulation 1, the PDL is properly applied to both the signal and the ASE noise; in Simulation 2, the PDL has been applied only at the signal, whereas, the accumulated noise is used only at the end of the transmission in order to evaluate the OSNR. This distinction has been made in order to underline that the PDL and noise interplay required a complex model that takes into account the interaction of the two quantities along the entire transmission. It can be observed that, while in the metro-to-rural propagation, the two simulation methodologies provides similar results, Fig. 3.15(b), on the opposite direction the predicted OSNR fluctuations are significantly different with a standard deviation of 0.2 and 0.6 dB, respectively for Simulation 1 and 2. It is worth to notice that Simulation 2 produces identical results in both transmission directions, proving that this approach is not adequate for a physical layer model of the optical system under investigation.

3.2.2 Experimental Validation of the PDL Simulations

In this investigation, the effect of the accumulated PDL as an OSNR penalty is experimentally observed on a 100G QPSK commercial TRX crossing 4 WSSs and exploring a large number of polarization rotation realizations by means of 3 PS and different noise injection configurations: the ASE noise has been loaded either purely at the transmitter side (**Scenario TX**), at the receiver side (**Scenario RX**), or in a uniformly distributed manner by using all the 4 ASE noise sources (**Scenario DIST**). The experimental results clearly show the complex interplay of the PDL and noise source distribution. Following this, a numerical Monte Carlo PDL/OSNR simulator is verified over the experimental results and extended to OLSs with uniform PDL and ASE distributions, in order to provide a quantitative OSNR penalty analysis in reference use cases. The experimental setup used for the direct observation of the PDL-induced OSNR degradation is schematized in Fig. 3.16. An optical source consisting of a commercial card generates a 100 Gbaud, QPSK channel with 25% roll-off at 194.3 THz. The signal is propagated through a cascade of 4 1x17 WSSs, replicating a characteristic OLS in a metro transmission scenario. Each port of the WSS is programmed by setting the filter bandwidth at 50 GHz, centred at the channel frequency without any extra attenuation; the latter condition assures fixed PDL values for each device maintained, for all the measurements. In particular, the first WSS is used as a multiplexer which introduces the channel in the OLS (*add* operation). Next, a de-multiplexer and a multiplexer are coupled, constituting the equivalent of a crossed ROADM, and lastly a de-multiplexer is used to filter out the channel (*drop* operation). Finally, 3 optical PSs are used in place of fiber connections between the OLS components mentioned above, each modifying the polarization state of the input signal, exploring the entire Poincaré sphere, and replicating in roughly 1 minute the long-time variations of the polarization rotation induced by the fiber spans in real systems. For the specific port and frequency, the PDL introduced by each component has been separately characterized before the setup installation along with

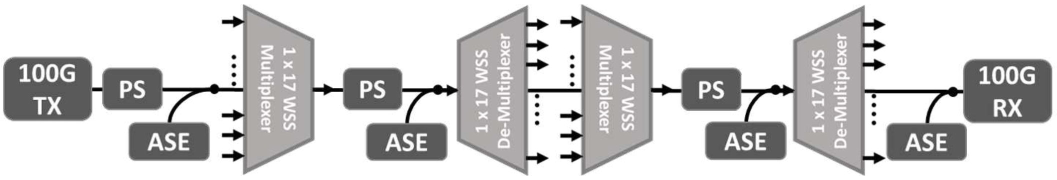

Fig. 3.16 Sketch of the experimental setup.

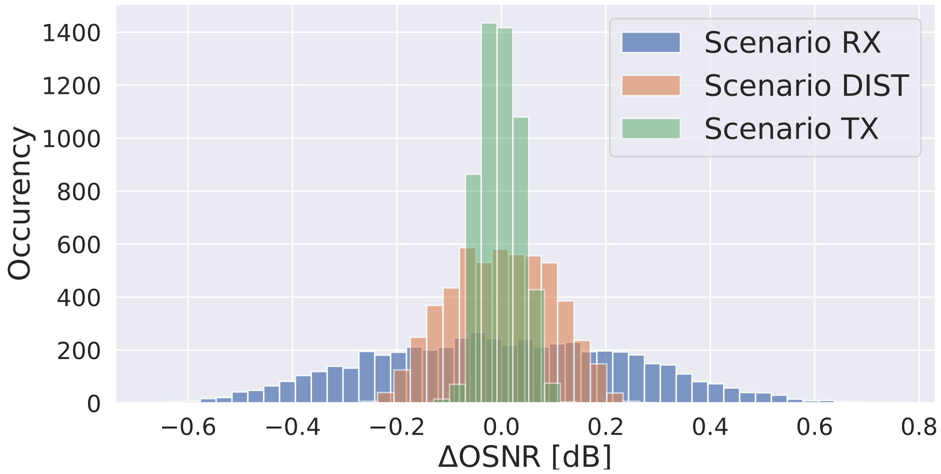

Fig. 3.17 Experimental distributions of the PDL-induced OSNR variation, ΔOSNR, for the three scenarios: RX, DIST and TX.

the resulting PDL of the entire OLS. PDL values of 0.2, 0.8 and 0.4 dB are obtained for the first multiplexer WSS, the ROADM equivalent coupled WSSs and the last de-multiplexer WSS, respectively; as the PS rotates the propagated signal along the entire Poincaré sphere, the measured total PDL roughly equals the PDL sum of the three components at 1.4 dB. Four distinct ASE noise sources are distributed along the OLS enabling a tunable distributed noise loading. For all three investigated scenarios, the amount of ASE noise injected has been precisely calibrated in order to provide a fixed overall OSNR value of 7.4 dB. After the propagation, the signal has been received and the OSNRs relative to the two distinct polarization directions have been separately obtained by converting the BER_X and BER_Y, respectively, evaluated by the commercial card. As the OSNR measurements on the two polarization directions provide equivalent results, in the following only one of the two metrics is considered and addressed simply as OSNR.

The measured distributions of the PDL-induced OSNR variations, ΔOSNR, with respect to the reference 7.4 dB value are shown in Fig. 3.17 for the three different scenarios. As quantitative metrics characterizing ΔASE are reported in Tab. 3.4, showing; the difference between the maximum and minimum measured ΔOSNR in dB, χ^m_OSNR, and the standard deviation of the ASE variations, σ^m_OSNR, expressed in dB as $\sigma^m_\text{OSNR, dB} = 10\log_{10}(1+\sigma^m_\text{OSNR, lin})$. As expected, ΔOSNR is strictly correlated to the noise distribution along the OLS. In particular, in **Scenario RX**, the PDL effect

Scenario	TX	DIST	RX
$\sigma^{m}_{\mathrm{OSNR}}$ [dB]	0.0	0.1	0.2
χ^{m}_{OSNR} [dB]	0.3	0.6	1.4
$\sigma^{s}_{\mathrm{OSNR}}$ [dB]	0.0	0.2	0.3
χ^{s}_{OSNR} [dB]	0.0	0.7	1.4

Table 3.4 Summary of σ_{OSNR} and χ_{OSNR} obtained from the experiments, m, and the simulations, s, for each scenario.

has the largest contribution and the ΔOSNR distribution coincides with the signal variation distribution, as the ASE noise introduced at the end terminal is constant. Moving the amount of added ASE noise towards the transmitter side, the ΔOSNR distribution shrinks reaching the minimum variation for **Scenario TX**. In this case, both the signal and the ASE noise undergo the same amount of PDL, therefore, the ASE is conserved along the entire OLS; in principle, the observed ΔOSNR should be equal to zero in this case. The residual PDL effect observed in **Scenario TX** can be attributed to the PDL experienced by the loaded ASE noise, which is filtered over the channel bandwidth using a separate WSS before being injected in the OLS.

In order to extend the PDL-induced degradation of the final ASE to various reference use cases, a Monte Carlo algorithm has been developed by replicating the propagation of the channel through the OLS, including the ASE noise injection, the local PDL effect, and the random polarization rotation of the channel induced by the fiber span. First, the measured ΔOSNR metrics with the simulated equivalents, χ^{s}_{OSNR} and $\sigma^{s}_{\mathrm{OSNR}}$, are compared. In Tab. 3.4, it can be observed that the simulations provide compatible results in terms of the chosen metrics and, in particular, preserve the behaviours highlighted in the description of the measurements. In addition, the Monte Carlo analysis has been extended to different reference use cases characterized by a uniform distribution of both PDL, summing up to a fixed value of 10 dB, and ASE noise generation, giving a final ASE of 20 dB, which is 3 dB above the reference *pre*-FEC threshold for the 400G transmission standard. In this work, the ASE is expressed by considering the entire channel symbol rate as the noise bandwidth. The simulation is iterated by propagating the channel through different OLSs, including, in turn, an incremental number of WSSs and ASE noise sources while maintaining the same amount of final total PDL, Σ_{PDL}, and ASE. In Fig. 3.18, the distributions of the simulated scenarios show that increasing the number of WSSs reduces the ASE variation for a given fixed total Σ_{PDL} value, suggesting that the realization

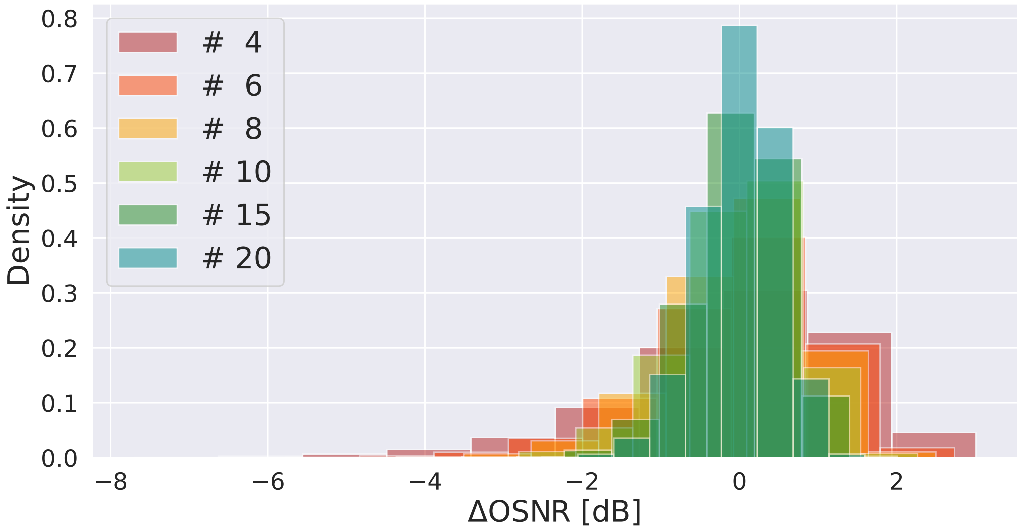

Fig. 3.18 Simulated ΔOSNR distributions for a growing number of WSSs introducing a fixed total PDL, $\Sigma_{\text{PDL}} = 10\,\text{dB}$.

probabilities of the worst case scenarios decrease sharply as the number of WSSs introducing the same total amount of PDL increases. Finally, the PDL-induced ASE penalty is quantified by fixing an arbitrary out-of-service τ equal to $0.1\,\%$. By approximating the simulated ASE distributions expressed in linear units with the equivalent truncated Gaussian distributions, it is possible to evaluate the minimum ASE margin that guaranties the fixed out-of-service probability, defined as PDL-induced ASE penalty. In Fig. 3.19, the evaluated ASE and PDL-induced penalties are shown for all simulated scenarios, along with the reference *pre*-FEC threshold given by the 400G transmission standard. It can be observed that, depending on the number of WSSs in the OLS, transmission scenarios involving the same amount of Σ_{PDL} may be affected by an overly large ASE penalty, preventing lightpath deployment. In any case, in most realistic scenarios, where the high value of accumulated PDL is given by a large number of WSSs that each introducing a reasonable PDL, the ASE penalty remains limited.

3.2.3 PDL Penalty Analytical Approach

In order to validate Eq.2.57 and Eq. 2.58, the Monte Carlo software framework reproducing the PDL effect has been leveraged to obtain an extensive simulated dataset in 5 distinct scenarios (5x10^5 samples each). For all the simulated optical systems, 9

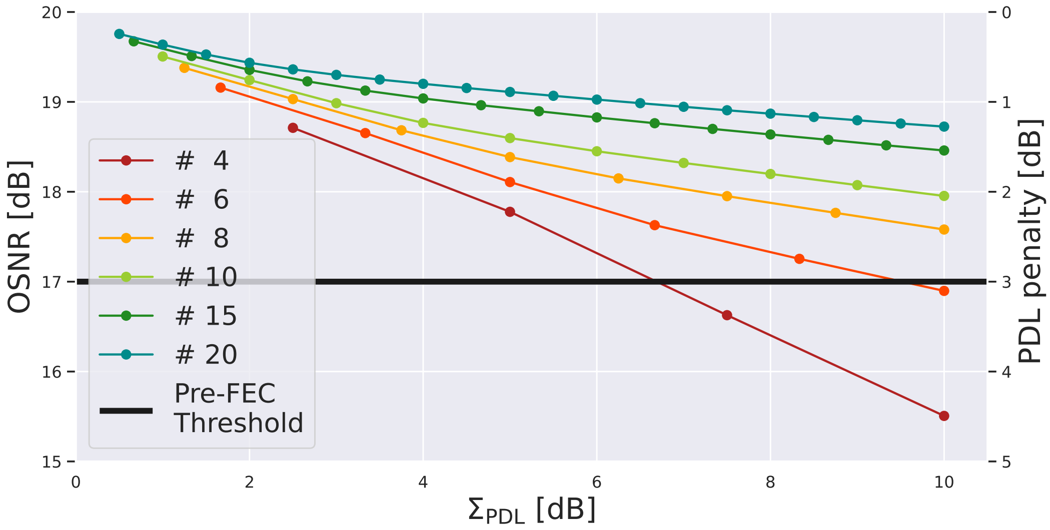

Fig. 3.19 OSNR and PDL-induced penalty vs. Σ_{PDL} for a growing number of WSSs.

PDL subsystems have been considered, composed of as many ROADMs and OLSs, and a single propagating channel. In particular, each PDL subsystem consists of a ROADM, which introduces a certain value of PDL on both the propagated signal and the accumulated noise, and an equivalent OLS which injects a given amount of noise. In this analysis, only the ASE noise generated by optical amplifiers within the OLSs has been considered. Additionally, the optical amplifier PDL has been neglected in order to simplify the system structure. Also, the channel launch power has been set to 0 dBm and no losses/gains induced by any fibers nor optical amplifiers have been considered. All the presented results can be seamlessly extended to a more realistic scenario. First, a uniform scenario is considered where each ROADM and each OLS introduce exactly 1.2 dB and 30 dB of PDL and OSNR degradation for each span. Then, maintaining a constant total PDL, $\Sigma_{\text{PDL}} = 1.2 \cdot 9 = 10.8$ dB, and final OSNR, roughly 20.35 dB, other four systems have been simulated, considering an increasing/decreasing PDL keeping an uniform OSNR degradation per span and *vice versa*. The entire set of PDL and OSNR degradation values per span are reported in Tab. 3.5.

	PDL [dB]			Noise [dBm]		
PDL Subsystem #	**Uniform**	**Increasing**	**Decreasing**	**Uniform**	**Increasing**	**Decreasing**
1	1.2	0.24	2.16	-30.0	-37.0	-27.4
2	1.2	0.48	1.92	-30.0	-34.0	-28
3	1.2	0.72	1.68	-30.0	-32.2	-28.5
4	1.2	0.96	1.44	-30.0	-31.0	-29.2
5	1.2	1.2	1.2	-30.0	-30.0	-30.0
6	1.2	1.44	0.96	-30.0	-29.2	-31.0
7	1.2	1.68	0.72	-30.0	-28.5	-32.2
8	1.2	1.92	0.48	-30.0	-28	-34.0
9	1.2	2.16	0.24	-30.0	-27.4	-37.0

Table 3.5 PDL and ASE noise values considered in all the investigated Monte Carlo simulations.

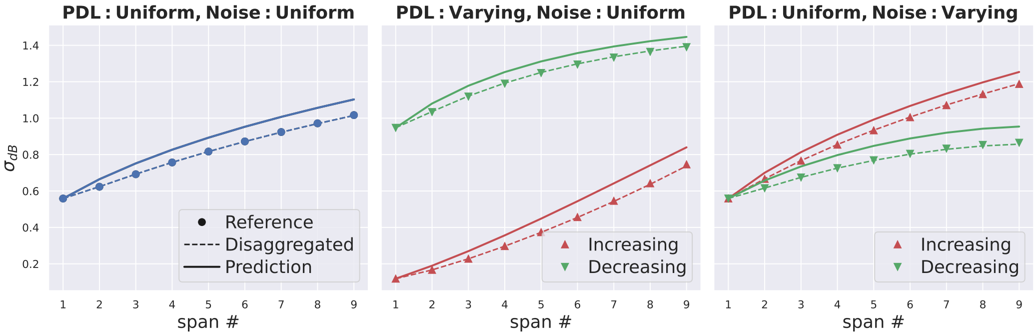

Fig. 3.20 OSNR PDL-induced σ simulated and evaluated with the proposed methodology for all the investigated transmission scenarios.

It is worth noting that high values of PDL have been considered in order to exacerbate its impact on the OSNR, therefore, the final obtained PDL penalty may differ significantly from a real-case scenario. Nevertheless, the scope of this study is the validation of the proposed methodology in such extremes conditions.

Fig. 3.20 and Fig. 3.21 demonstrate that Eq. 2.56 is verified and, for all the investigated scenarios, the reference Monte Carlo simulation, replicating the exact PDL effect abstraction, and the disaggregated Monte Carlo simulation, considering separately the PDL effect on distinct subsystems, produce equivalent OSNR distributions having negligible differences in terms of estimated σ and χ. Additionally, the proposed evaluation expressions of σ and χ, Eq. 2.57 and Eq. 2.58, provide an accurate and conservative estimation of the stochastic characterization of the PDL effect on the OSNR. Finally, in order to provide some estimation results from an operative standpoint, the PDL penalty has been evaluated for all the investigated scenarios, Fig. 3.22, with a fixed $\tau = 0.01$, demonstrating the different magnitude of the PDL effect on the OSNR depending on the relative distribution of PDL and injected noise, as shown in [68, 69].

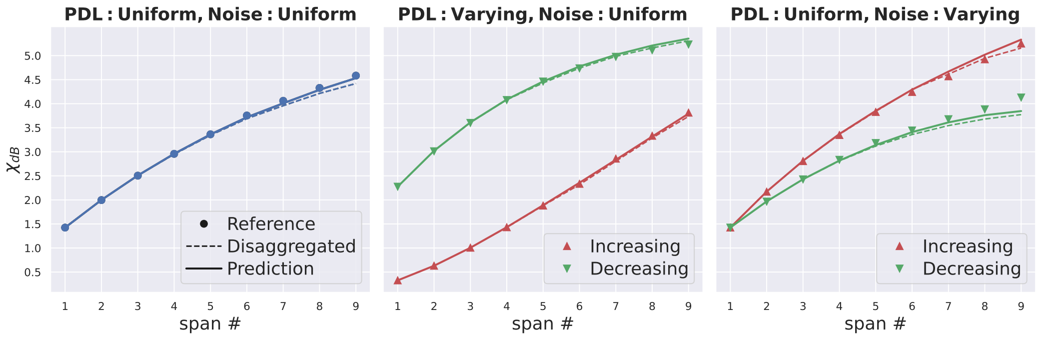

Fig. 3.21 OSNR PDL-induced χ simulated and evaluated with the proposed methodology for all the investigated transmission scenarios.

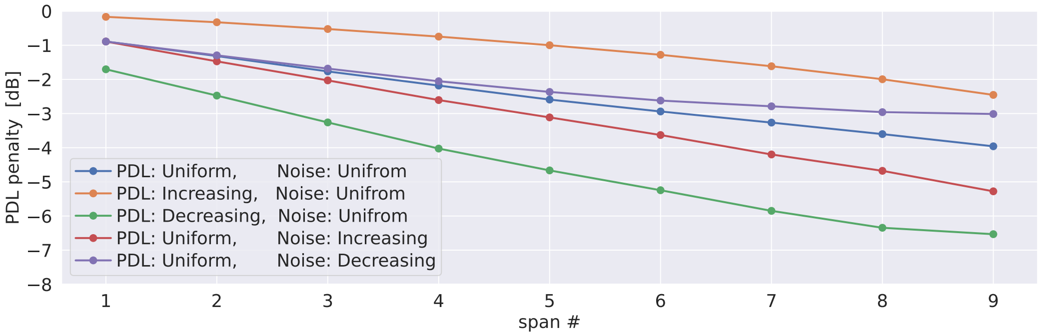

Fig. 3.22 PDL-induced penalty evaluated with the proposed methodology for all the investigated transmission scenarios.

Chapter 4

Simulation and Power Optimization in Multi-Band Transmission Scenario

In this chapter, the proposed methodologies introduced in Ch. 2 for the physical layer modeling are validated in multi-band transmission (MBT) scenarios using extensive simulation campaigns based on the SSFM and the numerical solution of the SRS. Aiming for a realistic testing scenario, first the multi-band optimization problem is defined and optimized transmission scenarios are considered in all the validations. Moreover, a model-driven approach is proposed for the optimization of MBT problems, achieving highly satisfactory results through a fast and descriptive extension of the LOGO.

4.1 MBT Optical Network Architecture and System Optimization

Without any loss of generality, the MBT optimization problem is defined on a multi-band C+L+S_1 transmission scenario for a given OLS, as illustrated in Fig. 4.1. In a comprehensive SDN framework, each OLS controller manages the operational optimization by setting the booster, pre-amplifier and in-line amplifier working points such that the optimal GSNR configuration [86] is found. In a MBT scenario, an appropriate definition of the optimal GSNR configuration is indispensable, as SRS effects may cause channel powers to differ significantly even within the same band.

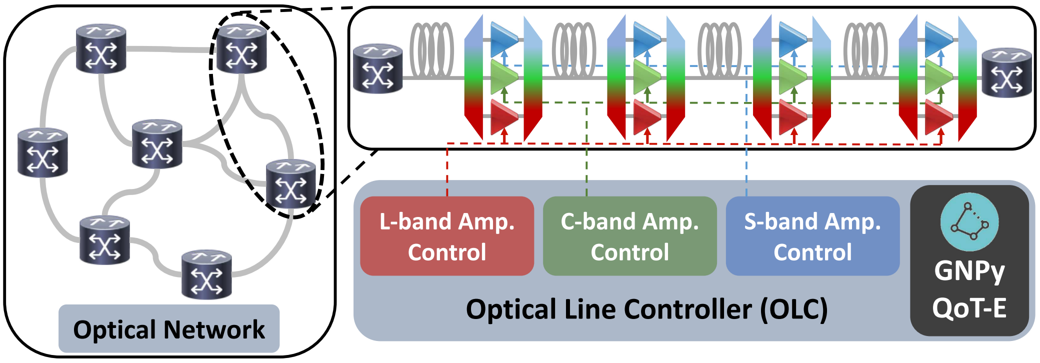

Fig. 4.1 The multi-band optical network architecture considered within this work. An independent OLS is considered, consisting of a series of fiber spans, each followed by amplifiers providing amplification for each band, controlled by an OLC. QoT is estimated using a GNPy-based model implementation.

Consequently, an approach that optimizes each individual channel power is required, going beyond a LOGO definition [92]. Bearing the disaggregated framework, it is necessary that spectral efficiency is maximized, while the spectral distribution across the entire available bandwidth is the most uniform possible [93, 94]. The latter requirement, when implemented on all OLSs, minimizes spectrum allocation complexity, enabling efficient, flexible, and dynamic lightpath deployment by the optical network orchestrator. It is worth noting that, in general, this implementation does not coincide with a maximum capacity solution on every OLS due to wavelength continuity constraints. In light of these considerations, the optimal GSNR configuration for each band is defined as the highest GSNR average value that can be reached while maintaining a certain level of flatness on the entire band. In general, finding this optimal solution is a complex task, as the trade-off between spectral flatness and maximum GSNR must be found in a large space of realizations, and several works tackling this problem have been proposed. In [95] a heuristics, which performs a power sweep per band to the point where no QoT gain is obtained, is evaluated and experimentally validated for C+L+S MBT scenario. Several works target the tilt and power settings of optical amplifiers for MBT scenarios using brute-force [96] or evolutionary algorithms, such as GA [97, 98] or particle swarm optimization [99, 100].

As shown in Fig. 4.1, in a multi-band scenario each set of channels within a spectral band is amplified by a distinct device. In a realistic scenario, two EDFAs amplify the C- and L-bands, whereas, S_1-band amplification is performed by a

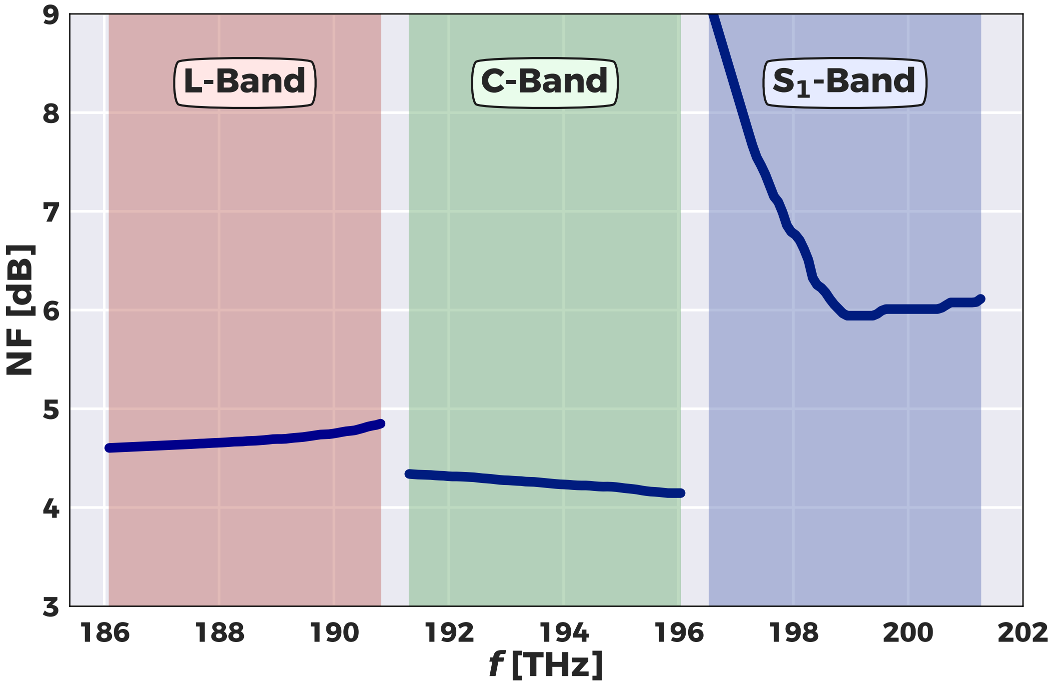

Fig. 4.2 The noise figures, NF, of the model EDFAs (C- and L-bands) and TDFA (S_1-band) used within this work as a function of frequency, along with the spectral regions representing the C-, L- and S_1-bands, and the 0.5 THz guard bands between them.

thulium-doped fiber amplifier (TDFA) [101]. The usage of different amplifiers for each set of channels comes from the fact that EDFAs, despite being a more mature technology than TDFAs, do not perform well for spectral regions outside of the C- and L-bands. Moreover, output power limitations of current amplifiers do not permit usage of an unlimited number of channels, which requires the L- and C-bands being amplified by distinct EDFAs, with two TDFAs also predicted to be required for full S-band amplification; here half of the entire S-band is considered and addressed as S_1-band. An alternative possibility is the usage of Raman amplification applied to MBT, which can provide an ultra-wide gain profile [102] and the potential to also control the mean gain and tilt [103].

In this analysis, ideal amplifiers that can recover the optimal launch power profile are considered. In general, amplifier NF varies with the amplifier gain values, and this phenomenon can be incorporated to the input power optimization procedure. Nevertheless, a constant frequency-dependent NF profiles shown in Fig. 4.2 is considered, except where explicitly indicated, which have been measured on commercial amplifier at a fixed gain level. Within the scope of this thesis,

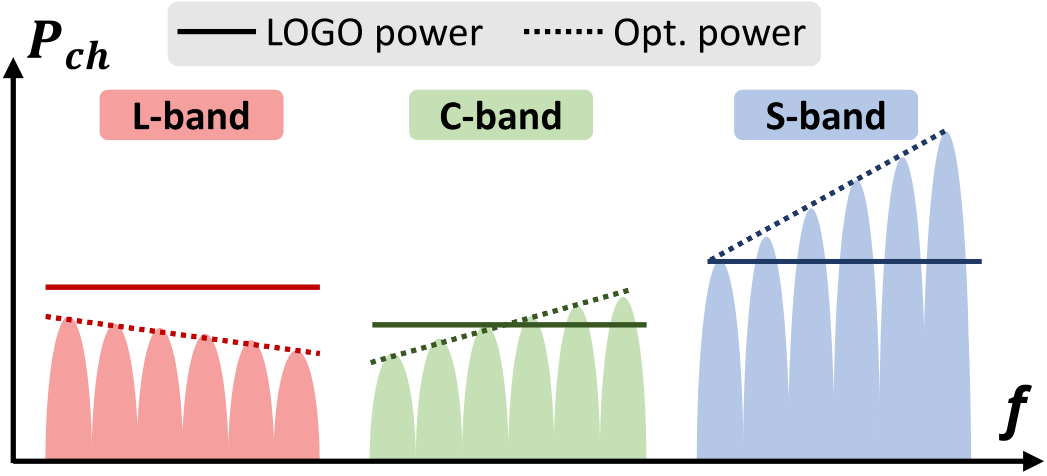

Fig. 4.3 EDFA/TDFA output power offset and tilt optimization.

for every transmission scenario, the launch power profile has been obtained by jointly optimizing the expected mean value and tilt of the GSNR by separately varying the average output power offset and tilt values of the EDFA/TDFA, for each band, as illustrated in Fig. 4.3. These optimizations are performed, maximizing the average GSNR value and flatness for all CUTs over the entire band under investigation. Remarkably, finer tuning strategies of the input power have been presented in literature and, in general, provide a better optimization, i.e. by using a per-channel equalization [104]. Nevertheless, shaping the launch power on a per-channel basis is not always possible, as DGEs that are able to perform this may not be available at all amplification sites. On the contrary, the adopted optimization procedure does not require any additional equipment, as the optimal input power obtained can be implemented by varying the EDFA/TDFA gains (or output power) and tilts, and these parameters are commonly available to be tuned in currently deployed infrastructures. When the EDFA parameters are known and the spectral load is constant, the single span ASE noise can be calculated by means of Eq. 2.50 using $R_{s,\lambda}$ as noise bandwidth. *Vice versa*, when EDFA parameters are unknown or inaccurate, and/or the spectral load is not constant, additional information is required in order to properly model and simulate the ASE noise power profile. In these scenarios, telemetry and monitoring data can be used to overcome the lack of information, e.g. with machine learning frameworks [105, 42], or with a model based characterization as in [47].

4.2 Multi-Band GGN approximation Validation

The single-OLS GSNR expressed in Eq. 1.3 can be further disaggregated on a span-by-span basis. Considering a periodical OLS, the OSNR_λ and $\mathrm{SNR}_{NL;\lambda}$, respectively, can be expressed as follows:

$$\mathrm{OSNR}_\lambda = \left(\sum_{s=1}^{N_s} \frac{P^{(s)}_{\mathrm{ASE};\lambda}}{P^{(s)}_\lambda}\right)^{-1} = \frac{1}{N_s}\frac{P_\lambda}{P_{\mathrm{ASE};\lambda}}, \tag{4.1}$$

$$\mathrm{SNR}_{\mathrm{NL};\lambda} \leq \left(\sum_{s=1}^{N_s} \frac{P^{(s)}_{\mathrm{NLI},\lambda}}{P^{(s)}_\lambda}\right)^{-1} = \frac{1}{N_s}\frac{P_\lambda}{P_{\mathrm{NLI};\lambda}}, \tag{4.2}$$

where $P^{(s)}_\lambda$, $P^{(s)}_{\mathrm{ASE};\lambda}$ and $P^{(s)}_{\mathrm{NLI};\lambda}$ are, respectively, the signal, ASE noise and NLI noise powers at the s-th span termination for a given λ. In this investigation, a periodic OLS is considered, as the disaggregation paradigm allows a straightforward generalization of this scenario. Consequently, the right-hand side expressions are obtained in both Eq. 4.1 and Eq. 4.2, defining $P_\lambda = P^{(s)}_\lambda$, $P_{\mathrm{ASE};\lambda} = P^{(s)}_{\mathrm{ASE};\lambda}$, $P_{\mathrm{NLI};\lambda} = P^{(s)}_{\mathrm{NLI};\lambda}$ $\forall s \in [1, N_s]$. Eq. 4.1 is verified with a high level of accuracy for a wide set of realistic optical systems, whereas the equality in Eq. 4.2 is verified only when there is no correlation between the NLI noise generated in each distinct fiber span. The latter condition is not fulfilled in a real transmission scenario and, as shown in [106, 107], this is due to the SC component of the NLI noise that accumulates coherently span-by-span. In general, Eq. 4.2 provides a non conservative estimation of the accumulated NLI noise, which can lead to a reduction of the expected margin or, in the worst case, an out of service scenario. As proposed in [82], this effect can be managed effectively by separating the NLI noise generated in each fiber span into its SC, $P_{\mathrm{SC};\lambda}$, and XC, $P_{\mathrm{XC};\lambda}$, contributions and including an asymptotic coefficient, C_∞, that takes into account the coherent SC accumulation. As observed in [106, 107], the four-wave-mixing (FWM) contribution to the NLI noise can be neglected without any significant loss in model accuracy for standard optical system transmissions. Even if the number of FWM contributions increase exponentially with the number of interfering channels, the overall FWM contribution to the NLI noise can be neglected also in a MBT scenario, as the entire inter-band NLI effect is negligible as shown in [93] for a C+L transmission scenario, roughly 10 THz of spectrum bandwidth. By means of the asymptotic overestimation, a conservative estimation of the NLI noise power, $P_{\mathrm{NLI};\lambda}$, can be substituted in Eq. 4.2 obtaining the following expression:

$$\mathrm{SNR}_{\mathrm{NL};\lambda,n} > \frac{1}{N_s} \frac{P_\lambda}{\left[(1+C_\infty)P_{\mathrm{SC};\lambda} + P_{\mathrm{XC};\lambda}\right]} \,. \tag{4.3}$$

Given this span-by-span disaggregation, the analysis of the signal degradations introduced by each OLS can be reduced to the investigation of the single span effects.

4.2.1 SSFM Detailed Description

To validate the proposed methodology an SSFM simulation campaign has been performed using an internal simulation software environment, developed starting from [108]. The SSFM provides a numerical solution to Eq. 2.32, simulating the propagation of a WDM signal time series through successive position steps, dz.

The WDM signal at the fiber termination can be calculated by dividing the fiber length into consecutive segments, z_m, separated by a variable step, dz_m, as depicted in Fig. 4.4. If the step lengths are sufficiently small, the linear and nonlinear operator in Eq. 4.4 can be applied separately, with negligible inaccuracy [109, 44], obtaining the following the operator notation:

$$\vec{A}(z_m + dz_m, t) \approx e^{\mathscr{L} dz_m} e^{\mathscr{N} dz_m} \vec{A}(z_m, t) \;, \tag{4.4}$$

where the linear operator $\mathscr{L}$ can be efficiently applied in the frequency domain by means of the fast Fourier transform (FFT) algorithm.

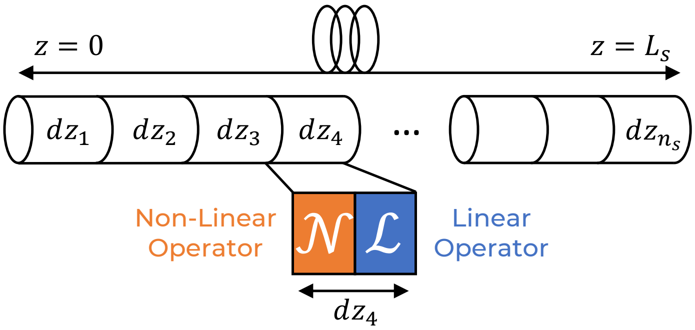

Fig. 4.4 Scheme of the split-step Fourier method. The linear, $\mathscr{L}$, and non-linear, $\mathscr{N}$, operators are applied separately in each dz step.

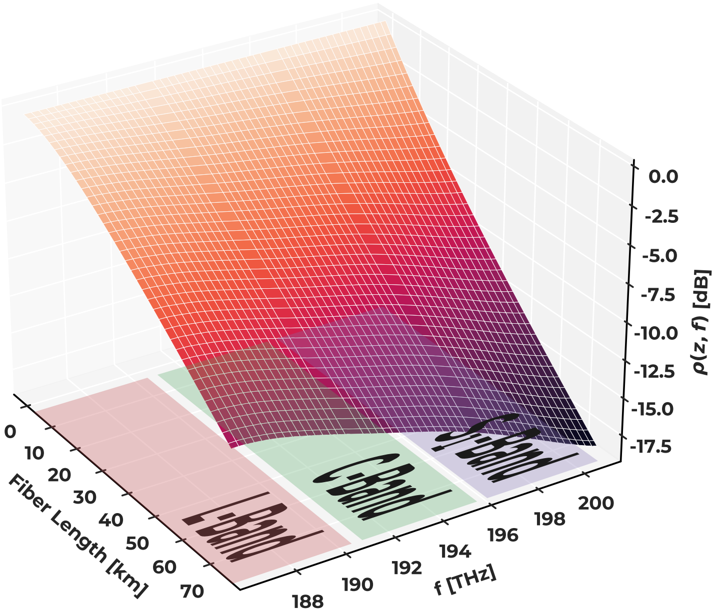

Fig. 4.5 Gain-Loss profile depending on SRS and frequency-dependent fiber loss.

Moreover, the step lengths can be optimized in order to find a trade-off between simulation accuracy and computational cost, as shorter steps implies more accuracy, but also more Fourier transform evaluations, which are the most computationally expensive steps in the SSFM algorithm. In this work, FWM-CLE step length optimization algorithm [109] is adopt, ensuring that the simulation error remains constant as the simulation bandwidth is enlarged (the accuracy parameter Φ_{FWM} is set to 0.01 radian for single channel simulations and to 1 radian otherwise). Starting from $z_0 = 0$, for each step the SSFM algorithm first applies the nonlinear operator in the time domain, expressed as follows:

$$\vec{A}_N(z_m + dz_m, t) = \mathscr{F}^{-1}[\vec{A}(z_m, f)] \cdot e^{-\imath \frac{8}{9}\gamma |\vec{A}(z_m,t)|^2 dz_m} , \tag{4.5}$$

where $\mathscr{F}$ stands for the Fourier transform applied using the FFT. The linear step is then applied to $\vec{A}_N(z_m + dz_m, t)$, obtaining the following evaluation of the WDM signal at the end of the m-th fiber step, in the frequency domain:

$$\vec{A}(z_m + dz_m, f) = \mathscr{F}[\vec{A}_N(z_m + dz_m, t)]\, e^{-\imath\beta(f) dz_m} \frac{\rho\,(z_m + dz_m, f)}{\rho\,(z_m, f)} , \tag{4.6}$$

where the exponential accounts for the dispersion accumulated along the length dz_m; the dispersion coefficient values for each frequency, $\beta(f)$, are interpolated along

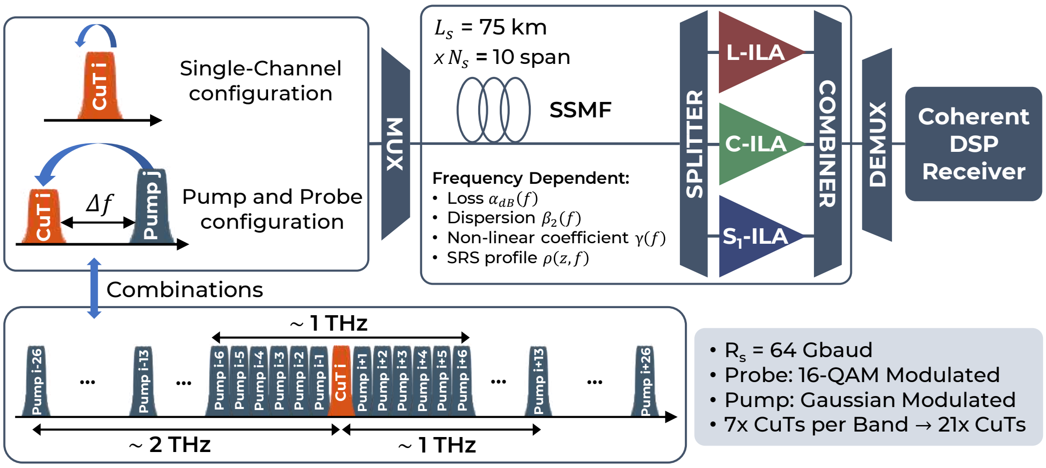

Fig. 4.6 A representation of the pump and probe campaign, simulated for each CUT. All pump and probe combinations within a 1 THz region encompassing the CUT, including a single-channel configuration, are propagated through the given line description and passed to the coherent DSP stage, along with additional pumps that lie 1 and 2 THz away from the CUT.

the simulated signal bandwidth using the measured curves of Fig. 2.3, and $\rho(z,f)$ is obtained by interpolating the solution of Eq. 2.12 for every considered frequency and position, as shown in Fig. 4.5. In particular, the solution of Eq. 2.12 has been obtain with a fast SRS solver implementation available in GNPy considering an optimized launch power profile. This launch power profile has been obtained optimizing the GSNR average and flatness.

4.2.2 SSFM Simulation Campaign

In this work, a C+L+S_1 400 Gbps transmission scenario over a periodic 10-span OLS has been investigated. Each band is populated with 64 square root-raised cosine shaped channels with roll-off values of 0.15 at R_s= 64 Gbaud in a 75 GHz fixed grid, for a total of 192 channels. A modulation format of polarization multiplexed 16-QAM is considered for all the CUTs, delivering 400 Gbit/s per channel, according to the 400G-ZR+ standard. A guard-band of 500 GHz has been placed between the bands in order to avoid band-splitting filter penalties, which is required to perform separate amplification, as depicted in the simulation setup of Fig. 4.6. The channel central frequencies range between 186.0 and 201.3 THz, respectively, for a total spectral occupancy of 15.3 THz. The channel launch power profile has been optimized using a exhaustive search algorithm [110], and it is shown in Fig. 4.7. It is worth noticing that, qualitatively, the launch power profile is flat in the S_1-band as a combined result of the propagation effects, resulting in a clockwise tilt observable in the L- and C-bands, and the counter-clockwise tilted NF profile in the S_1-band itself.

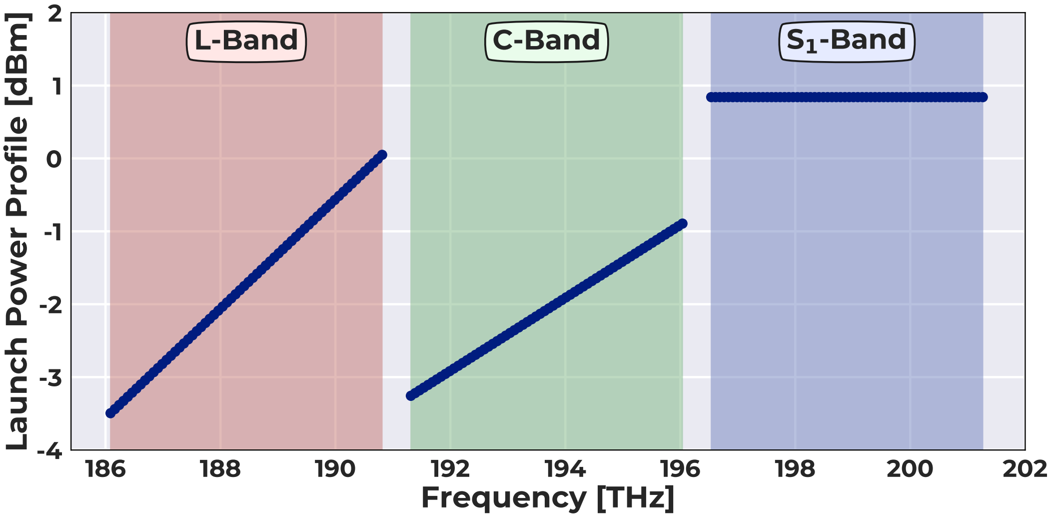

Fig. 4.7 Launch power profile with average of -1.72, -2.07 and 0.84 dBm and tilts of 0.75, 0.50 and 0.0 dB/THz for L-, C- and S_1-bands, respectively.

Concerning the OLS, 10 amplified fiber spans composed of ITU-T G.652D standard SSMF have been considered. All fiber spans are 75 km long and are characterized by the frequency-dependent physical layer parameters described in Sec. 2.2.1. In order to isolate the nonlinear term of Eq.1.3, the WDM signal is propagated assuming noiseless amplifiers during the SSFM simulation. At the OLS termination, the WDM signal enters the DSP-based coherent receiver. An ideal DAC/ADC is considered, and as such filter out the four quadratures/polarization components of each CUT by re-sampling the WDM signal at 2 samples per symbol. Then, an deal dispersion compensation is applied, exactly recovering the amount of dispersion accumulated by each CUT. The signal is then fed to the adaptive equalizer stage, which converges to the matched filter. The equalizer stage is based on a least mean square (LMS) algorithm with 42 taps and an adaptation coefficient of 10^{-4}. This large tap size is set to maximize equalizer performance and to allow detection of even small amounts of nonlinear noise in the very first span of the OLS.

Next, a carrier phase estimation (CPE) block recovers the nonlinear phase noise, neglecting transmitter laser phase noise. The phase recovery algorithm uses the knowledge of the transmitted symbols to recover the carrier phase by dynamically setting the CPE memory. The optimal memory value maximizes the circularity of the noise clouds around the transmitted symbol scattering diagram. It should be noted that the optimal CPE memory, obtained by considering only the NLI noise, may not coincide with the optimum of a real systems, where the presence of ASE noise, which is the dominant impairment, produce a further trade off. However, the CPE optimization is outside the scope of this work and the chosen optimal CPE memory ensures the most accurate simulation of the NLI noise introduced by the fiber propagation.

The SNR is then calculated upon the decision signal at 1 sample per symbol after the CPE stage. Considering noiseless amplifiers, the estimated signal-to-noise ratio coincides with the $\text{SNR}_{\text{NL};\lambda}$. Moreover, assuming an ideal receiver, the transmitted symbol series can be subtracted from the decision signal and $P_{\text{NLI};\lambda}$ can be evaluated as the variance of the residual signal.

4.2.3 Disaggregated SSFM using Single-Channel and Pump-and-Probe Configurations

Simulating the reference full spectral load scenario is practically unfeasible due to the enormous computational costs associated to the simulation of a WDM signal that occupies ≥ 15 THz. Furthermore, this approach would not allow the investigation of NLI generation in a spectrally disaggregated fashion. Therefore, for each band 7 equally spaced CUTs have been selected and two sets of simulations have been carried out in order to isolate the NLI contributors (the SC and XC) for each, as outlined in Fig.4.6:

- **Single-Channel Configuration**: simulation of the propagation of solely the CUT, λ, with the estimation after the DSP consequently accounting only for the SC NLI component.
- **Pump-and-Probe Configuration**: simulation of the propagation of the CUT (the probe), λ, and a single interfering channel (the pump), κ, with an incremental frequency distance, Δf, from the probe. In this case, the estimation

after the DSP accounts only for the XC NLI component; the SC NLI component is kept negligible by setting the probe power to a sufficiently low value (-20 dBm; the obtained result is then re-scaled to the required CUT power).

For practical reasons, a subset of pump and probe scenarios is simulated, as outlined in the bottom of Fig.4.6; for each CUT, all pumps up to $\Delta f = \pm 500\,\text{GHz}$ have been evaluated, along with four pumps located at $\Delta f = \pm 1\,\text{THz}$ and $\Delta f = \pm 2\,\text{THz}$. The CUTs are kept as 16-QAM modulated, whereas the pumps are modulated using a Gaussian distributed symbol sequence, which provides an upper bound to the NLI intensity generation [111]. Additionally, channels propagating through an OLS can be considered as Gaussian distributed if a sufficient amount of dispersion has been accumulated [63, 112]. The entire set of single-channel and pump-and-probe simulations are performed using the fiber gain/loss profile of the overall C+L+S_1 transmission scenario, including the Raman effect, shown in Fig.4.5.

4.2.4 GGN Approximation Accuracy

The results of 10-span 400 Gbis transmission through a C+L+S_1 OLS using the SSFM are compered with the simulation of the GGN-based GNPy current implementation and the approximated GGN model presented in Sec. 2.2.3 The separate contributions to the total $P^{(s)}_{\text{NLI};\lambda}$ at the s-th span is considered at first. As a periodic OLS is considered, $P^{(s)}_{\text{NLI};\lambda}$ can be normalized with respect to the launch power, obtaining:

$$\eta^{(s)}_{\lambda,\kappa} = \frac{P^{(s)}_{\text{NLI};\lambda}}{P_\lambda P_\kappa^2}\,, \tag{4.7}$$

which represents the NLI efficiency when a single fiber span is considered, providing a direct metric for the frequency-dependent fiber parameter effects, and the separate NLI contributions of each interfering channel, κ. Fig. 4.8 illustrates $\eta^{(n)}_{\lambda,\kappa}$ evaluated at the OLS termination for the C-, L-, and S_1-band central channels, respectively. For all investigated CUTs, the GGN and proposed approximation provide a conservative estimation with respect to the interfering channel contribution given by the SSFM implementation. Furthermore, close to the CUT the SC and XC contributions of interfering channels are highly accurate for both methodologies, with inaccuracies increasing proportional to the frequency difference between the CUT and the interfering channel. In order to quantify the accuracy of the simulations in terms of

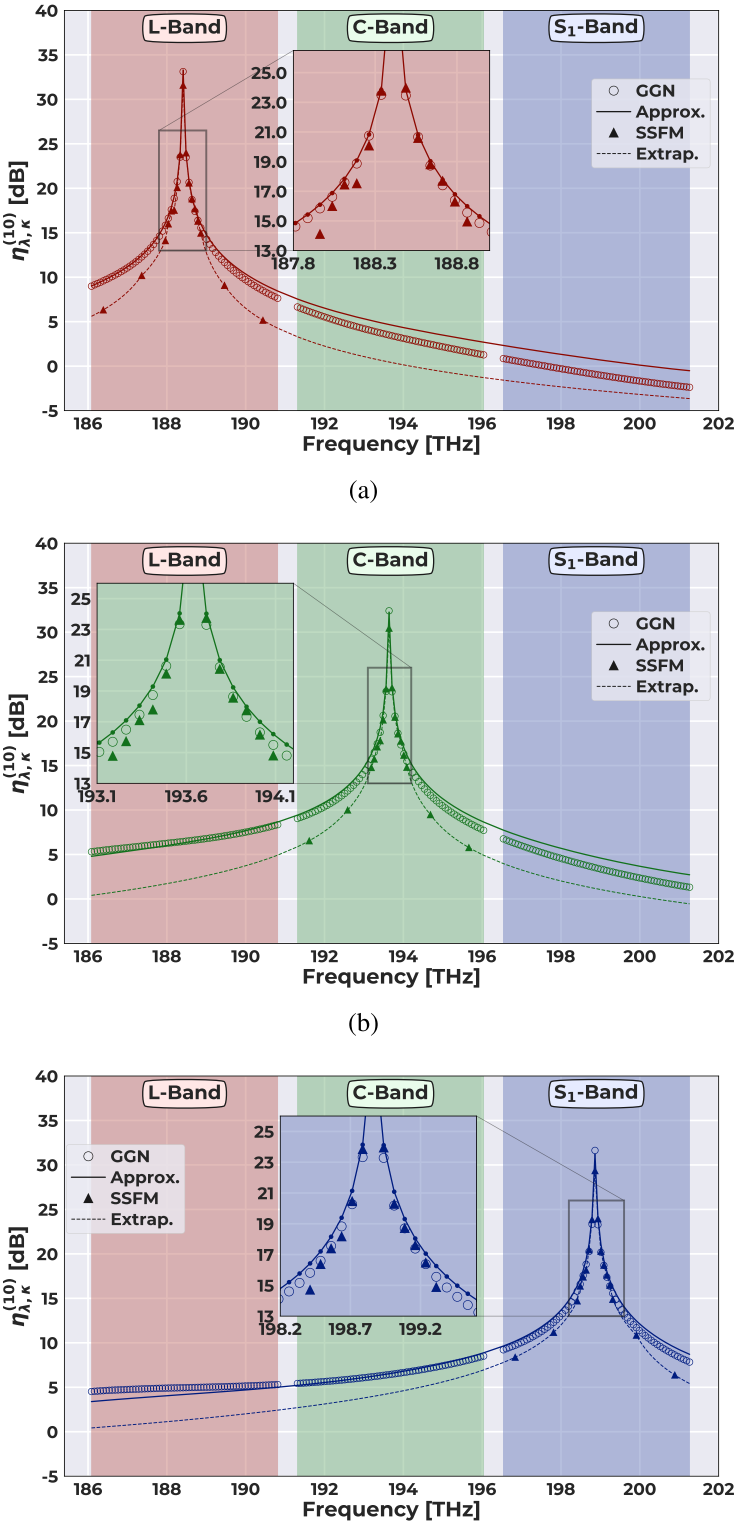

(a)

(b)

(c)

Fig. 4.8 Normalized NLI contribution for distinct pump and probe configurations at the OLS termination.

overall QoT for each CUT, as a reference, the extrapolated $\eta_{\lambda,\kappa}^{(n)}$ for all pump and probe configurations that have not been simulated using the SSFM is presented for each CUT; these extrapolations are shown with dashed lines in Fig. 4.8, and has been obtained applying the interpolation function defined in SciPy, a well-known open-source Python library, to the available $\eta_{\lambda,\kappa}^{(n)}$ simulations expressed in linear units. The SNR $_{\mathrm{NL}}$ can now be evaluated by summing all distinct NLI contributions. The SNR $_{\mathrm{NL}}$ comparisons between the extrapolated SSFM results, used as a reference in this analysis, the GGN-based GNPy implementation and the proposed approximation are shown in Fig.4.9(a) for all the CUTs. The GGN-based GNPy implementation and the proposed approximation provide an SNR $_{\mathrm{NL}}$ prediction with average errors of 1.3 and 1.2 dB, respectively, and an equal maximum error of 1.7 dB. These inaccuracies are reduced by combining the simulated SNR $_{\mathrm{NL}}$ values with the evaluated OSNR, as shown in Fig. 4.9(b), to find the GSNR for all implementations, shown in Fig. 4.9(c). With this QoT metric the two methodologies provide estimations with average errors of 0.3 and 0.2 dB, and maximum errors of 0.5 and 0.3, respectively. Considering these error margins, the proposed approximation provides a conservative, satisfactorily accurate and computationally fast result for all CUTs, and may reasonably be extended to larger bandwidths, given sufficient hardware and physical layer information.

In order to provide a reference value for the GSNR metrics, the results in Fig. 4.9(c) can be compared with the required minimum SNR threshold expressed in the OpenROADM 400G 16-QAM transceiver specifications included in the GNPy equipment library. Such a device required a minimum SNR of 24 dB that is equivalent to a GSNR of 17 dB evaluated over the channel symbol rate, as the GSNR results presented in this work. Considering this threshold, both the GNPy GGN implementation and the proposed approximation provide an accurate prediction of the lightpath feasibility considering the SSFM extrapolation as the real scenario reference. In particular, both methodologies confirm the GSNR availability for the 400G 16-QAM transmission over both the C- and L-band, whereas they predict that this transmission technology is unfeasible on the S_1-band, as it can be observed in Fig. 4.9(c). As a matter of fact, this analysis would be more complicated on a real scenario where additional penalties and inaccuracies of parameter values can affect the accuracy of the presented prediction. Nevertheless, QoT estimators as the GNPy GGN implementation have shown significant improvements in network planning, margin design and lightpath computation, gathering the interest of vendors and operators.

4.3 Multi-Band Perturbative SRS Validation

In this section, the truncated solution of the perturbative expansion is verified at the optimum launch power profile for each considered MBT scenario.

For the purpose of this investigation, a periodic multi-band OLS of 10 spans is considered. The assumed values of noise figure, NF, for each optical amplifier type are reported in Tab. 4.1 according to the corresponding band [113]. The fiber spans are 70 km long and are characterized by the realistic wideband parameter description reported in Sec. 2.2.1. The transmitted signal is implemented according to the 400G standard: Each channel carries a Polarization Multiplexed (PM)-16-QAM signal with a R_s of 64 Gbaud and a slot width of 75 GHz.

In this framework, a cutting-edge C+L+S-band transmission scenario is considered along with a more future looking U-to-E-band transmission scenario in order to perform a solid validation of the proposed methodology. In both cases, the optimal launch power has been evaluated.

Additionally, an ideal flat loss coefficient profile at 0.2 dB/km is considered in order to separately analyze the effect of the SRS effect on the power profile along the fiber. In this case, a flat launch power of -1 dBm per channel is considered. The impact of the real and ideal fiber loss coefficient profiles in terms of total attenuation along a single fiber span is shown in Fig. 4.10 and 4.11.

In these figures, also the effect of the effective area scaling is shown; its contribution produces variation within each transmission band in a range of 0.5 dB, suggesting that it is necessary to consider this phenomenon mainly for the OSNR estimation especially after the propagation of a WDM comb through a considerable number of sections. Even if this effect turns out to be of secondary importance, in a

Table 4.1 Optical amplifier noise figure values used in the considered wideband scenario.

	U	**L**	**C**	**S**	**E**
NF [dB]	**6.0**	**6.0**	**5.5**	**7.0**	**7.0**

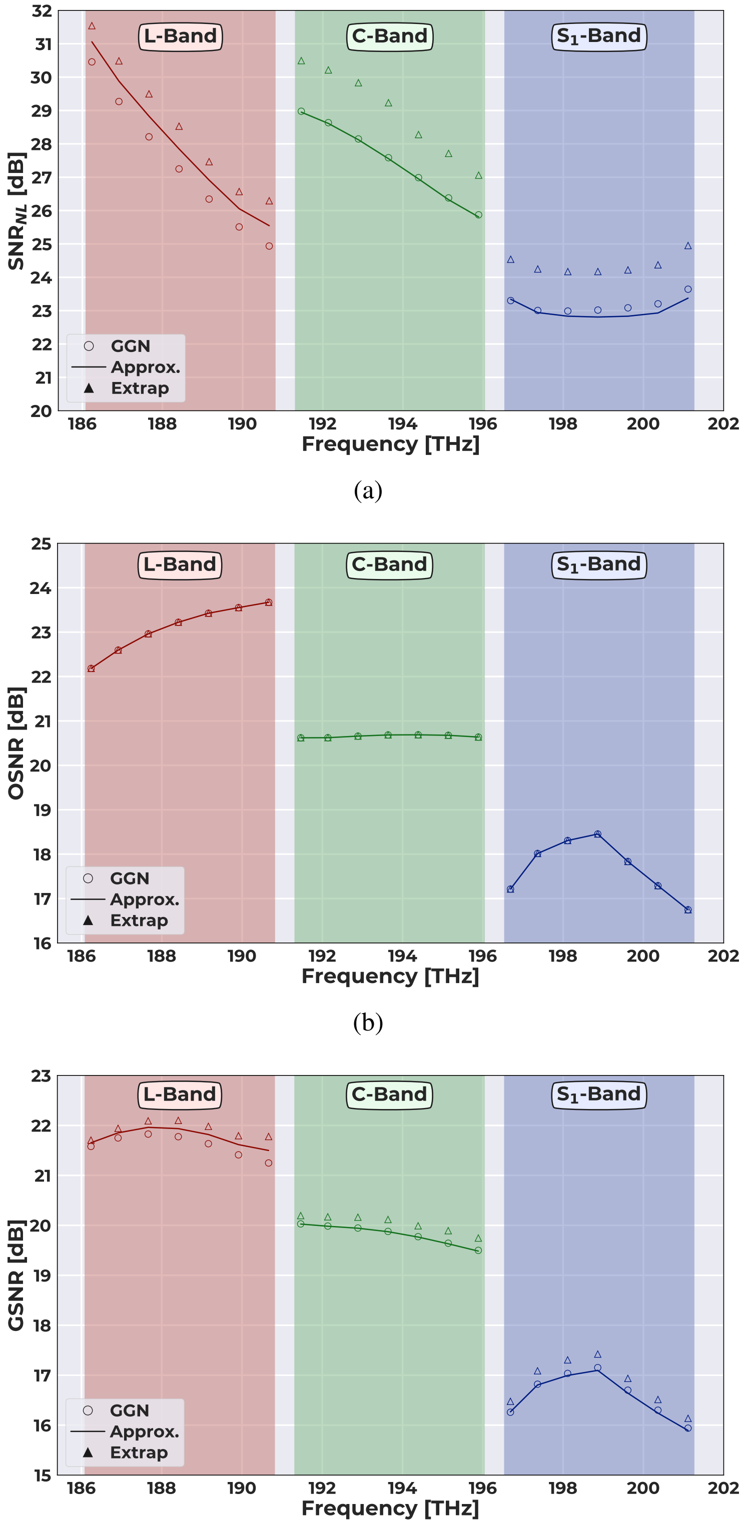

(a)

(b)

(c)

Fig. 4.9 SNR_{NL}, OSNR and GSNR comparison between the SSFM extrapolation, GGN-based GNPy implementation and the proposed approximation, for all CUTs.

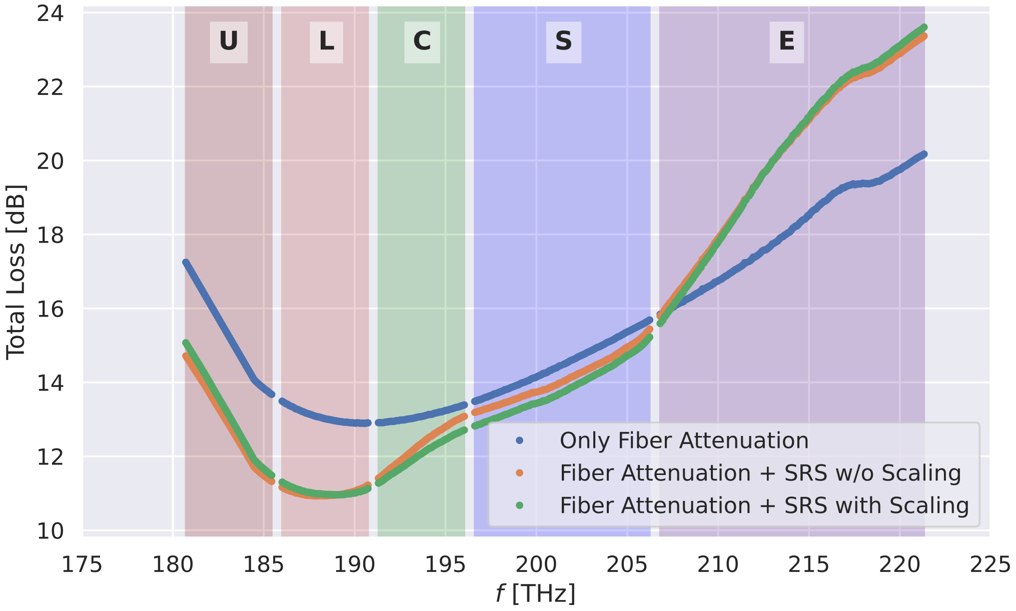

Fig. 4.10 Realistic fiber loss coefficient in a wideband transmission scenario.

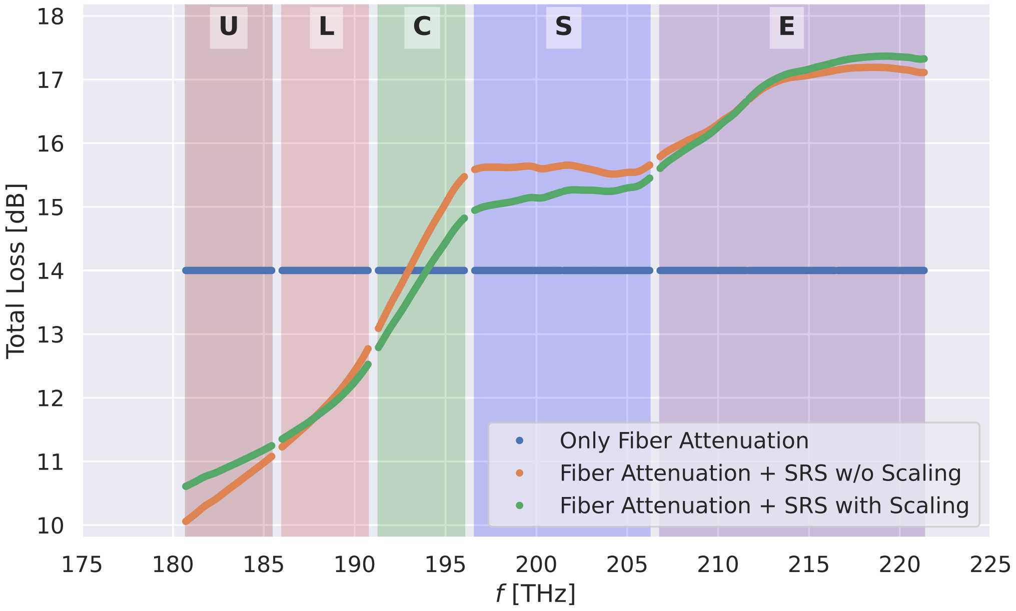

Fig. 4.11 Ideal fiber loss coefficient in a wideband transmission scenario.

wideband context its accumulation across the various spans can generate a significant effect.

First, for all the transmission scenarios, the solution of Eq. 2.12 has been solved using the numerical integration defined in [62], which provides an accurate reference if the position increments are small enough; for the validation purpose, a constant step of 0.8 m has been chosen, providing an accuracy of the evaluated power profile along the fiber of 0.001 dB, for all the frequencies of the transmitted spectra. Then, the reference is compared with a truncated solution of the perturbative expansion presented in Sec. 2.2.2. Given the optimal launch powers of all the considered transmission scenarios, the perturbative expansion Eq. 2.21 is convergent. In particular, the successive orders are monotonously decreasing and, moreover, considering the k-th order truncated solution, the infinite sum of the remainder orders converges. Therefore, an arbitrarily small relative error, $\mathscr{E}_\lambda^{(k)}(z)$, for all the channels of the propagated spectrum can be achieved considering the proper k-th order of the solution.

In Fig. 4.12(b), the 4-th truncated solution of Eq. 2.30 is compared with the reference evaluation in the case flat fiber loss profile and P_λ, shown in Fig. 4.12(a), at the fiber termination, L_s. In Fig. 4.12(c), it is shown that increasing the order of the solution, an increasing accuracy is obtained, until the arbitrary tolerance of 0.1 dB is achieved. Finally, in Fig. 4.12(d), the normalized error $\mathscr{E}_\lambda^{(k)}(L_s)/\max\left(|\mathscr{E}_\lambda^{(k)}(L_s)|\right)$ up to the 4-th order is shown. As expected, it can be observed that the k-th relative error has exactly the symmetry in frequency of the $k+1$-th order, which it is its most significant term. Therefore, odd orders have an even error function in frequency and *vice versa*, demonstrating that the proposed perturbative expansion is exact at every order.

Further analysis on the formal expansion Eq. 2.21 are out of the scope of this study and will be investigated in future publications. A heuristic effective and conservative estimation of the proper order required to achieved at least a given tolerance, τ, has been validated for a set of increasing U-to-E transmission bandwidth and an increasing flat launch power per channel, $P_\lambda \in [-4, 2]$ dBm, resulting in a total power at the fiber input for the full U-to-E scenario of 23.1 and 29.1 dBm, respectively; this evaluation provides the correct order or at most the successive, guaranteeing the required accuracy. Due to the complex spectral shape of the Raman coefficient profile, distinct orders have different interactions with the power profile

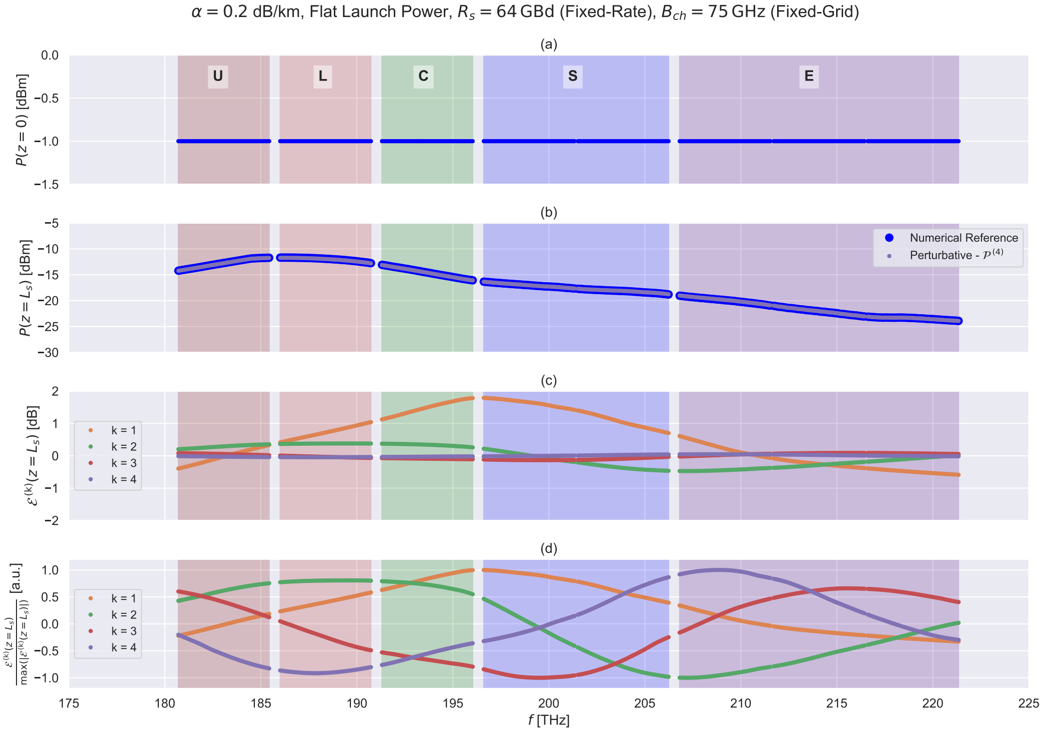

Fig. 4.12 Ideal flat fiber loss profile simulations. In particular, (a) Flat launch power at -1 dBm per channel. (b) Comparison of the numerical reference and the 4-th order perturbative solution. (c) Relative error up to the 4-th order. (d) Normalized relative error up to the 4-th order.

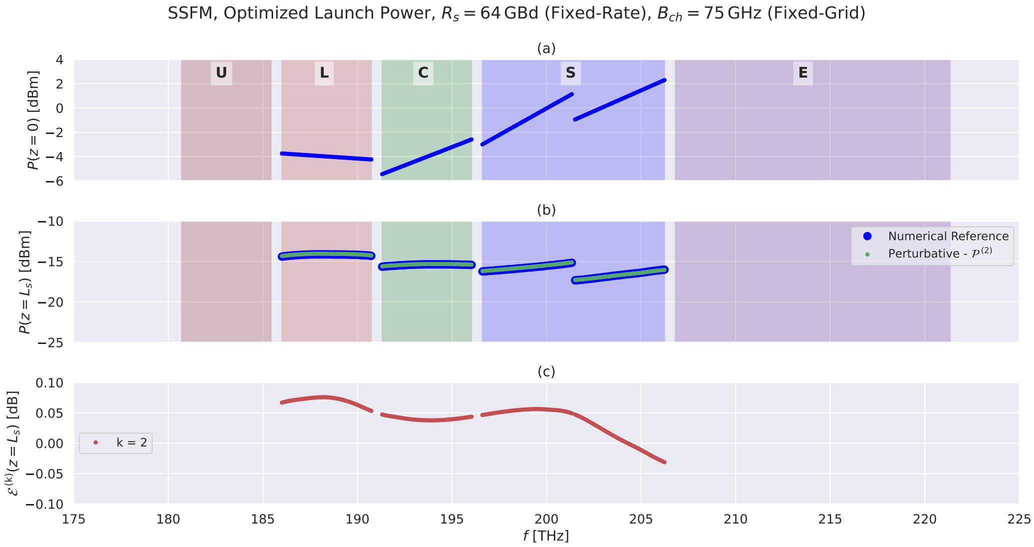

Fig. 4.13 Realistic fiber parameters simulations, C+L+S-band transmission scenario. In particular, (a) Optimal launch power. (b) Comparison of the numerical reference and the 2-nd order perturbative solution. (c) Relative error up to the 2-nd order.

along the fiber, therefore, the proposed estimation procedure has to be perform after the calculation of each order and it is expressed by the following inequality:

$$\left|\mathscr{E}_{\lambda}^{(k)}(z)\right| \leq \frac{10}{\ln(10)}\left[\exp\left(\theta^{(k)}\right) - \sum_{j=0}^{k}\frac{\left(\theta^{(k)}\right)^{j}}{j!}\right] \leq \tau\,, \tag{4.8}$$

with

$$\theta^{(k)} = \sqrt[k]{k!\,\max\left(\left|\Gamma_{\lambda}^{k}(z)\right|\right)}\,. \tag{4.9}$$

Using Eq. 4.8, with a defined tolerance of 0.1 dB, the truncated solution at the proper order of Eq 2.30 has been evaluated for all the investigated realistic transmission scenarios; for both cases the required tolerance is achieved at the exact order evaluated by means of Eq. 4.8. In Fig. 4.13 and Fig. 4.14, the launch power profile, the reference and evaluated power profile at the fiber termination and the relative error are reported for the C+L+S-band and U-to-E transmission scenarios, respectively.

Finally, the proposed methodology enables a faster implementation of the SRS solver for all the transmission scenarios with respect to the numerical integration method, given a certain tolerance value. As an example, the integral solution of

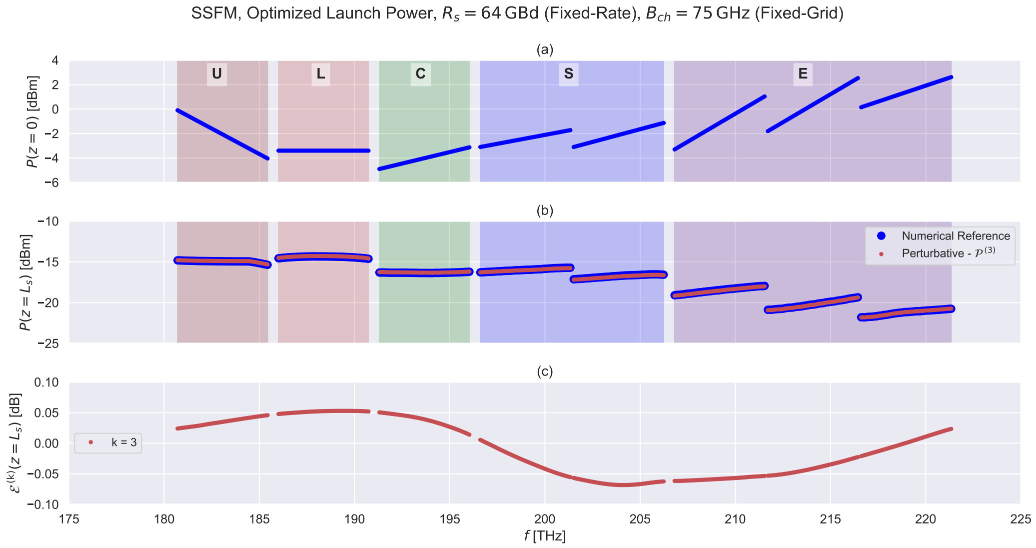

Fig. 4.14 Realistic fiber parameters simulations, U-to-E-band transmission scenario. In particular, (a) Optimal launch power. (b) Comparison of the numerical reference and the 3-rd order perturbative solution. (c) Relative error up to the 3-rd order.

each order, as Eq. 2.24- 2.27, can be integrated numerically in order to obtain the perturbative solution without evaluating an explicit form, as Eq. 2.28, for each perturbative order. Remarkably, the position increment required to achieved a given accuracy spatially integrating the perturbative orders, roughly tens of km if $\tau = 0.1$ dB, is significantly larger then the position increment required by the numerical solution to achieve the very same accuracy, roughly 0.1-1 km. Therefore, the perturbative solution required a significantly lower computational effort to achieve the same result of the numerical solution. Regarding the explicit expression of each order, as anticipated in Sec. 2.2.2, it is not always convenient in terms of computational cost. This is due to the high number of channels involved in a wideband scenario and can be overcome considering a lower number of equivalent macro channels in place of the real propagated channels, assuming that the variations of the intrinsic fiber loss, the Raman coefficient profile and the power spectral density are negligible within the macro channel bandwidths. Further consideration on this aspects will be addressed in a future publication.

In this study, an increasing total transmission bandwidth is considered from 2.5 to 40 THz starting from the first portion of the U-band to the last portion of the E-band, with a step of 2.5 THz. For all this spectra, a fixed power per channel of -1 dBm has been set and the proper order and position increment for the spacial integration has

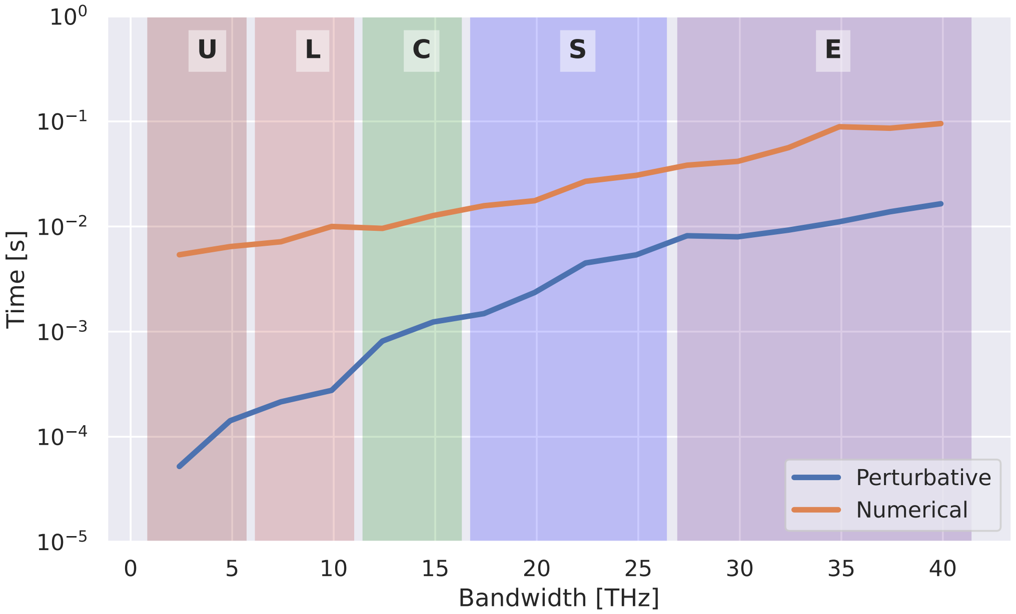

Fig. 4.15 Computational time of the perturbative and numerical solution, respectively, evaluated for an increasing total bandwidth of the transmitted spectrum with a flat power of -1 dBm per channel.

been evaluated for both the perturbative and numerical solution in order to obtain a fixed 0.1 dB tolerance. The resulting computational times are reported in Fig. 4.15, where it can be observed that the perturbative solution perform at least one order of magnitude better than the numerical solution.

4.4 Leading Inter-Band Intra-Channel Nonlinear effects in C+L-Band Transmission Systems

The complexity of the MBT optimization problem arises from the two nonlinear effects due to the fiber propagation, the SRS and the NLI, both depending upon the input signal power profile. As a matter of fact, the nonlinear nature of these two quantities prevents separate optimization from being performed for each λ. In this section, an investigation of these nonlinear effect is presented aiming to a simplification of the MBT optimization problem through an analysis of the inter-band inter-channel (IB-IC) SRS and NLI effects, in order to enable the OLS abstraction to be disaggregated on a per-band basis. It is possible to approximate the shape of the SRS function, which enables the creation of fast, closed-form expressions for aggregated NLI generation [57, 58], providing excellent accuracy in the C-band. Simplifying the effects of SRS as a tilt is not applicable when the transmission bandwidth exceeds the peak of the SRS spectral efficiency, which is reached at approximately 15 THz of spectral distance between the pump and the probe. Furthermore, alongside MBT network upgrades, current trends in optical network architectures are towards disaggregated infrastructures, where the amplified lines connecting the nodes within the network may be open ROADMs, including OLSs that may be wholly independent. In this framework, it is crucial to tackling NLI generation in a spectrally and spatially disaggregated manner to incorporate the possibility of alien wavelengths and unknown physical layer information within the NLI model in use [107, 82]. Approaching modelling from this perspective allows the IB-IC effects of the SRS and NLI to be considered separately, enabling efficient optimization when additional bands are included in a C-band system upgrade. A more precise description of the NLI effects can be provided considering the coherent behavior of the SC-NLI accumulation, which can be taken into account by introducing an asymptotic coefficient that depends on the chromatic dispersion, symbol rate and WDM grid, as shown in [82]. Separating the components of the inter- and intra-band cross channel (XC) -NLI, the total NLI noise can be modeled as in the following expression for a given CUT expressed in the following expression:

$$P_{\mathrm{NLI}} = P_{\mathrm{NLI,Intra}} + P_{\mathrm{NLI,Inter}} = \mathrm{C}_{\infty} P_{\mathrm{SC}} + P_{\mathrm{XC,Intra}} + P_{\mathrm{XC,Inter}} \tag{4.10}$$

where C_{∞} is the asymptotic accumulation coefficient, P_{SC} and P_{XC} are the NLI contributions given by the SC and XC interference, respectively. The effects of all four-wave mixing effects that do not correspond to the SC-NLI and XC-NLI contributions to the NLI can be neglected in the scenario under investigation; $\mathrm{P}_{\mathrm{XC,Intra}}$ is the intra-band contribution from interfering channels within the same band of the CUT, whereas $\mathrm{P}_{\mathrm{XC,Inter}}$ is the inter-band contribution from interfering channels within the other bands, corresponding to the IB-IC NLI.

The work presented in [93] demonstrated that the $\mathrm{P}_{\mathrm{XC,Inter}}$ term in Eq. 4.10 is negligible. This allows further considerations from an optimization perspective as the remainder MBT complexity resides exclusively in the IB-IC SRS-induced power transfer. For completeness, the investigation presented in [93] is here integrated and extended, describing in detail the operational consequences from an optimization standpoint considering a C+L-band transmission scenario.

To investigate the performance of a C+L implementation and, correspondingly, the contributions of IB-IC SRS and NLI to the final GSNR degradation, four distinct SSFM simulations, encompassing three different scenarios have been performed.

- **Scenario 1**: the C and L bands are transmitted independently, with separate SSFM simulations performed for each band. In these two simulations, both the intra-band SRS and the intra-band NLI have been considered. The input power profiles of each band are optimized independently.
- **Scenario 2**: the C and L bands are transmitted simultaneously. However, the IB-IC NLI is completely neglected, with the only observable inter-band interaction being the IB-IC SRS. The entire input power profile is optimized as in Scenario 3.
- **Scenario 3**: the C and L bands are transmitted simultaneously, considering both the IB-IC SRS and NLI. This simulation contains no artifacts and is the reference for the real-case C+L transmission scenario. The entire input power profile is obtained by simultaneously optimizing the GSNR average and flatness on both bands.

The first three scenarios have been simulated in order to separately quantify the effect of the IB-IC SRS and NLI, additionally, a fourth scenario has been simulated in order to compare two distinct implementations of the C+L transmission:

- **Scenario 4**: the C and L bands are transmitted simultaneously, considering both the IB-IC SRS and NLI. With respect to Scenario 3, the input power profile of the C band is kept fixed to the optimum found for the C band only (Scenario 1), so that only the input power profile of the L band is optimized.

This scenario is considered as a naive implementation of a C- to C+L-band upgrade for an existing OLS, as it resembles a case where the L-band is turned on without touching the existing C-band power configuration. Starting from an optimized C-band only transmission, the L-band is loaded and optimized so that a maximum degradation of 0.5 dB in the C-band GSNR offset is permitted. The comparison between Scenario 3 and 4 allows quantification of the performance gain that can be achieved with an overall MBT optimization, and provides an interesting use case where the analysis of the inter-band effects can be effectively exploited. For each optimized input power profile, a power evolution profile is evaluated as the solution of the combined effect of the SRS and the fiber loss for all frequencies along the entire fiber length. This power evolution profile is then used within the implemented software framework to perform the SSFM simulations, which are carried out as described in detail in Sec. 4.2.2.

The optimal input power profiles for all investigated scenarios are described in Tab. 4.2 for each band in terms of spectral tilt and offset with respect to the separately evaluated LOGO values of uniform -0.46 and -0.62 dBm per channel for the L- and C-band, respectively. The average values of GSNR, OSNR and SNR $_{\text{NL}}$ values obtained from the SSFM simulation campaign evaluated over the considered CUTs at the OLS termination for each band are reported in Tab. 4.3.

Table 4.2 EDFA output power offset and tilt value optimization results.

	Offset [dB]		Tilt [dB/THz]	
Band	L	C	L	C
Scenario 1	0.0	0.0	0.3	0.3
Scenario 2 & 3	-0.5	0.5	0.4	0.4
Scenario 4	-0.5	0.0	0.4	0.3

Table 4.3 Simulation results given separately as GSNR, OSNR and SNR_{NL} for each band.

Scenario	1	2	3	4	Band
GSNR [dB]	20.41	20.70	20.65	20.59	L
GSNR [dB]	20.75	20.50	20.46	20.22	C
OSNR [dB]	21.36	21.59	21.59	21.51	L
OSNR [dB]	21.72	21.53	21.53	21.03	C
SNR_{NL} [dB]	27.63	28.03	27.89	27.97	L
SNR_{NL} [dB]	27.84	27.36	27.18	27.94	C

Remarkably, all simulations within this work are performed on a specific OLS for a 400G transmission scenario; however, these results may be generalized to different OLS and transmission configurations, as the GSNR variations that are induced by different input power optimizations are analyzed. Fig. 4.16 reports the GSNR, OSNR, and SNR $_{\mathrm{NL}}$ values obtained from the SSFM simulation campaign at the OLS termination for every CUT, in the first three scenarios. A first clear observation from Fig. 4.16(c) is that an adequate level of flatness is achieved for all the scenarios under investigation, with the final GSNR profile within an interval of 0.2 dB.

Fig. 4.16(c) provide an insight into the leading inter-band interactions: first, introducing the IB-IC SRS (passing from Scenario 1 to Scenario 2) causes the main GSNR variation for every CUT, similar to the OSNR variation that is introduced by the IB-IC SRS, visible in Fig. 4.16(a). On the contrary, when the IB-IC NLI is introduced (passing from Scenario 2 to Scenario 3) the impact upon the GSNR variation is significantly reduced. This variation is essentially negligible for all CUTs except those that are in proximity to the other band, which is still minimal, as can be observed in Fig. 4.16(b). These observations demonstrate that the IB-IC SRS is the greatest contributor to the GSNR variation in a C+L band scenario, with the effects of the IB-IC NLI able to be neglected.

From an optimization perspective, this conclusion leads to the following approximate expression of the GSNR offset for each band:

$$\mathrm{GSNR}_{\mathrm{C}} \approx \frac{P_{\mathrm{C}} - \Delta_{\mathrm{SRS}}P}{P_{\mathrm{ASE}_{\mathrm{C}}} + P_{\mathrm{NLI}_{\mathrm{C}}}(P_{\mathrm{C}})}, \tag{4.11}$$

$$\mathrm{GSNR}_{\mathrm{L}} \approx \frac{P_{\mathrm{L}} + \Delta_{\mathrm{SRS}}P}{\mathrm{P}_{\mathrm{ASE}_{\mathrm{L}}} + P_{\mathrm{NLI}_{\mathrm{L}}}(P_{\mathrm{L}})}, \tag{4.12}$$

where $P_{\mathrm{C,L}}$, $P_{\mathrm{ASE}_{\mathrm{C,L}}}$ and $P_{\mathrm{NLI}_{\mathrm{C,L}}}$ are, respectively, the input signal, the ASE and intra-band NLI power offsets for each band central frequency. $\Delta_{\mathrm{SRS}}P$ represents the power transfer at the band central frequency due to IB-IC SRS being the only considered inter-band effect; this quantity depends on the OLS characteristics and can be found as a solution to the SRS equations, given both P_{C} and P_{L}. By means of Eq. 4.11 and Eq. 4.12, the GSNR offset shift shown in Fig. 4.16(c) for each band passing from Scenario 1 to 3, can be heuristically predicted when $\Delta_{\mathrm{SRS}}P$ has been evaluated.

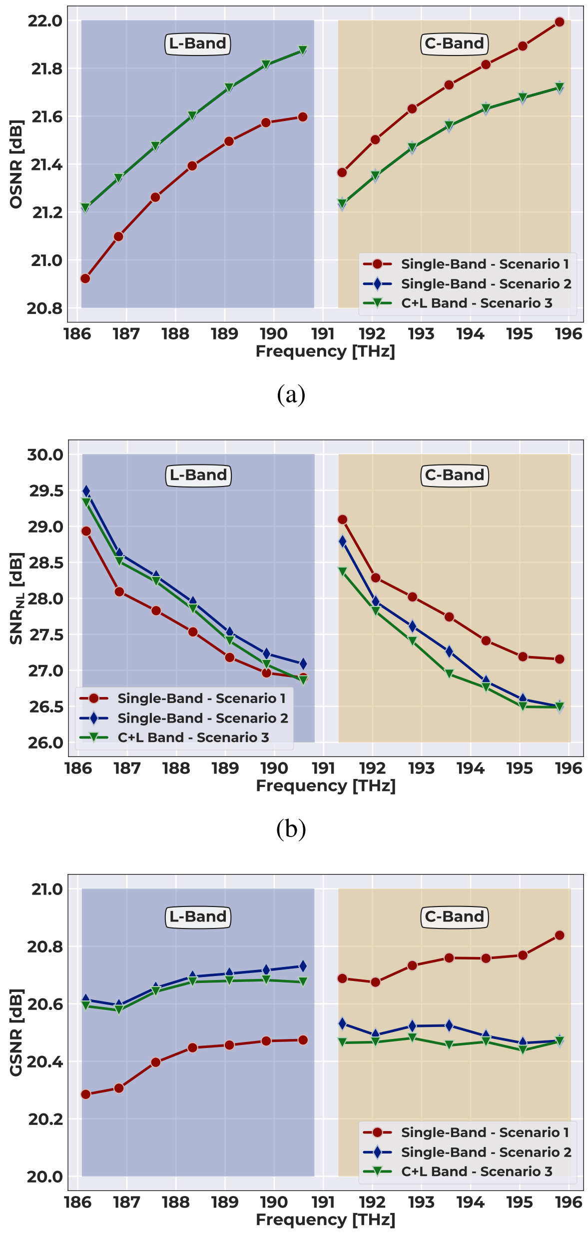

(a)

(b)

(c)

Fig. 4.16 (a) OSNR evaluated for every CUT. For all plots, the red circle, blue diamond and green triangle markers and dashed lines represent the simulation results in Scenario 1, 2 and 3, respectively. (b) SNR_{NL} evaluated for every CUT. For all plots, the red circle, blue diamond and green triangle markers and dashed lines represent the simulation results in Scenario 1, 2 and 3, respectively. (c) GSNR evaluated for every CUT. For all plots, the red circle, blue diamond and green triangle markers and dashed lines represent the simulation results in Scenario 1, 2 and 3, respectively.

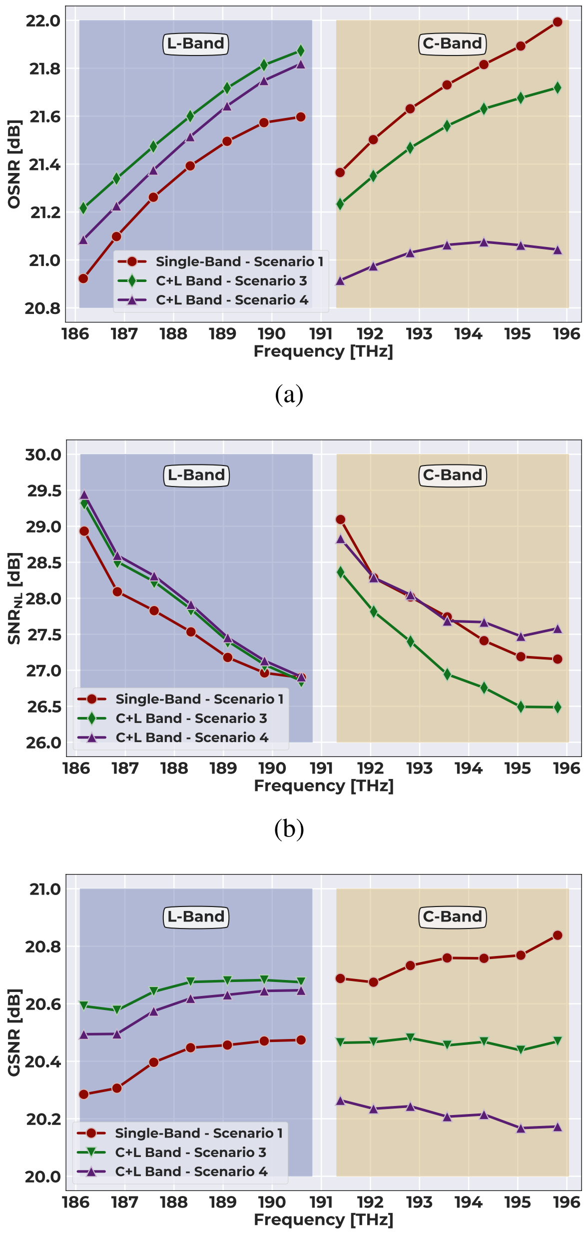

(a)

(b)

(c)

Fig. 4.17 (a) OSNR evaluated for every CUT. For all plots, the red circle, green diamond and purple triangle markers represent the simulation results for all the CUTs in Scenario 1, 3 and 4, respectively. (b) $\mathrm{SNR_{NL}}$ evaluated for every CUT. For all plots, the red circle, green diamond and purple triangle markers represent the simulation results for all the CUTs in Scenario 1, 3 and 4, respectively. (c) GSNR evaluated for every CUT. For all plots, the red circle, green diamond and purple triangle markers represent the simulation results for all the CUTs in Scenario 1, 3 and 4, respectively.

To investigate a realistic use case, the system update from C- to C+L-band transmission is considered. In a first considered scenario the system is upgraded from a standalone C-band scenario (Scenario 1) by beginning transmission in the L-band and keeping the C-band working points unchanged (from Scenario 1 to Scenario 4). As the current traffic on the C-band must be conserved to avoid out-of-service, an available GSNR margin of roughly 0.5 dB is considered. With this requirement, the input power of the L-band cannot be set as the optimum configuration for the L-band, as this would produce an unacceptable high level of degradation of GSNR on the C-band, as quantified by Eq. 4.11. Therefore, the L-band input power profile is set to a sub-optimum solution to maintain the C-band GSNR offset within the given margin; the result of this procedure has been simulated in Scenario 4 and is shown in Fig. 4.17(c). It is worth highlighting that the degradation of GSNR in the C-band that can be observed when adding the L-band upgrade is completely compatible with the OSNR degradation observed in the C-band in Fig. 4.17(a). From an optimization perspective, Eq. 4.11 and Eq. 4.12 provide a deeper insight into the inter-band GSNR correlation. The effect of the IB-IC SRS is that the optimal input power is moved to higher/lower values for the C- and L-bands, respectively; this can be quantitatively observed by comparing the optimal input power offsets of the two bands in Scenario 1 and Scenario 3 in Tab. 4.3. Therefore, it can be deduced that the C- and L-band stand-alone optimum input power offsets correspond to the lower and upper bounds for the MBT optimization. Focusing on the considered use case, P_{C} can be increased up to the optimal value found in Scenario 3. Performing this change incrementally moves GSNR_C towards its optimum and simultaneously changes GSNR_L due to the corresponding change in $\Delta_{\mathrm{SRS}}P$. The increment of P_{C} is limited both by the C- and L-band stand-alone optimum modified by the $\Delta_{\mathrm{SRS}}P$. Furthermore, it is worth noting that as the IB-IC NLI is negligible, there is not any additional $\mathrm{SNR}_{\mathrm{NL}}$ degradation on the L-band when increasing the offset of the input power of the C-band, as shown in Fig. 4.17(b).

4.4.1 LOGO MBT Extension Results and Validation

The literature contributions regarding the MBT optimization problem and reported in 4.1 demonstrate that heuristic and meta-heuristics can be leveraged in order to accelerate the optimum search task, maintaining the accuracy equal to the QoT estimator precision that has been chosen for the system predictions. Even if significant improvements in terms of computational time have been shown, this may be not practical in several use cases; e.g. when considering large-scale network systems or when an instantaneous system response is required in order to minimize service interruption after a network fault.

In this section, an optimization algorithm is based on multi-band extension of LOGO calculation is proposed. In particular, it is demonstrated that by means of a negligible loss of the MBT model precision, an explicit expression of the optimized launch power can be derived, exploiting the intrinsic nature of the major inter-band mutual interactions. While heuristics and meta-heuristics provide the optimized launch power without a direct insight into the multi-band system features, the proposed explicit expression of the optimization problem solution can be used for instant and efficient estimations and analysis for the network planning, design, and control. Additionally, it is worth noting that, when a more accurate evaluation is required, the proposed solution can be effectively considered as initial condition of a heuristic or meta-heuristic optimization algorithm.

The rough heuristic expressed by Eq. 4.11 and 4.12, can be precisely defined considering the final optimized launch power offset, $\tilde{P}_B$, for each band, B, as a perturbation of the optimized launch power offset, $P_B^{(s)}$, obtained in a single-band transmission scenario, respectively. By means of this assumption, the first-order SRS solution in terms of the g_R can be considered to define approximate corrections of both the OSNR and the SNR $_{\mathrm{NL}}$ as functions of the optimal single-band launch powers. Bearing in mind the optimization perspective, the targets of this approach are two values for each band: the launch power offset, $\tilde{P}_B$, and the launch power tilt, $\tilde{T}_B$. In this analysis, an explicit expression of $\tilde{P}_B$ is provided for each band as an extension of the LOGO formula based on the Gaussian noise (GGN) model on the separate single-band transmission scenario, obtaining a solution that depends only on $P_B^{(s)}$ and SRS-induced power transfer. However, an explicit expression of $\tilde{T}_B$ required a more complex approach as on the boundaries channels of each band the IB-IC NLI cannot be neglected due to the proximity of the neighboring bands; this can be observed in Fig. 4.16(b). Indeed, this problem can be overcome considering the IB-IC NLI of the neighboring bands for the boundary channels of each band, but this is out of the scope of this study, as the target of this investigation is a simple expression based on the LOGO optimization of the single-band transmission scenario. Nevertheless, a procedure that provides the $\tilde{T}_B$ values with a single transmission simulation is proposed.

First, focusing on the $\tilde{P}_B$ definition, the following expressions for the central channel of the k-th band can be written:

$$
\begin{aligned}
\tilde{\mathrm{P}}_{\mathrm{ASE},k} &= hf_k NF_k R_{s,k} e^{\tilde{\alpha}_k L}, && (4.13)\\
\tilde{\mathrm{P}}_{\mathrm{NLI},k} &= \tilde{\eta}_k \tilde{P}_k^3, && (4.14)
\end{aligned}
$$

where, with respect to Eq. 2.50 and considering a transparent transmission scenario, G is substituted with the product of the fiber length, L, and $e^{\tilde{\alpha}_k L}$ that represent the first-order SRS correction of the gain/loss power profile along the fiber length. Whereas, $\tilde{\eta}_{k,j}$ is a first-order SRS correction of the η_{NLI} which is defined by the GN model, where any IB-IC NLI contribution is neglected, and only the interference between the central channel and the j-th channel within the very same band is considered. More precisely, $\tilde{\alpha}_k$ and η_k can be written for the central channel of the k-th band as follows:

$$
\begin{aligned}
\tilde{\alpha}_k &= \alpha_k - \sum_{B,i_B} \frac{P_B^{(s)} C_{k,i_B}}{\alpha_{i_B} L} \left(1 - e^{-\alpha_{i_B} L}\right), && (4.15)\\
\tilde{\eta}_k &= \frac{8\gamma_k^2 \left(1 - e^{-\tilde{\alpha}_k L}\right)^2}{27\pi \left|\beta_{2,k}\right| \tilde{\alpha}_k R_{s,k}^2} \operatorname{arcsinh}\left(\frac{\pi^2 \left|\beta_{2,k}\right| R_{s,k}^2 N_{ch,k}^{2\Delta_k}}{2\tilde{\alpha}_k}\right), && (4.16)
\end{aligned}
$$

where α_k, $\beta_{2,k}$, γ_k, $N_{ch,k}$ and $\Delta_k = R_{s,k}/\Delta f_k$ are, respectively, the intrinsic fiber loss, the dispersion coefficient, the nonlinear coefficient and the ratio between the symbol rate and the slot width of the central channel of the k-th band. B the index of the interfering bands, i_B the index of each channel within the interfering band B, C_{k,i_B} is the value of the SRS coefficient evaluated between the k- and i_B-th channels and $P_B^{(s)}$ is the B-th single-band optimized launch power. Eq. 4.15 and Eq. 4.16 can be further simplified by considering equivalent flat values of α_{i_B} and C_{k,i_B} for all channels in the interference band B.

Given these explicit expressions, Eq. 4.13 and Eq. 4.14 can be leveraged to find the solution of the optimization problem for any MBT scenario, applying the optimization constraints on a per-band basis. In particular, by enforcing the optimization strategy described in Sec. 4.1, the optimal launch power offset of each band B can be set such that:

$$\tilde{P}_B = \sqrt[3]{\frac{\tilde{\mathrm{P}}_{\mathrm{ASE},B}}{2\tilde{\eta}_B}} \quad \forall B. \tag{4.17}$$

Remarkably, using Eq.4.17, the solution of the optimization problem for each band depends only on the physical parameter evaluated in the specific band, and on the single-band optimized powers, $P_B^{(s)}$, of all the bands, which are known values that can be evaluated *a priori* using, as an example, a simple expression of the LOGO optimization algorithm for the single-band transmission scenario.

In order to evaluate the generalization of our proposed method, this analysis investigates the single-, two- and three-band transmission scenarios upon a specific OLS. In order to perform a solid validation, the transmitted spectrum is diversified varying the symbol rates and slot widths, 32/64 GBaud and 50/75 GHz, respectively, of each band, obtaining 26 distinct combinations such that these quantities are the same for all the channels within the same band, but they vary from one band to the other.

Exceeding the 10 THz of total transmission bandwidth, it is complicated to manage the complexity of SSFM simulations, which can provide inaccurate estimates of transmission impairments. Moreover, the available SSFM implementation requires a large computational cost resulting in an unfeasible computational time. Therefore, as a transmission simulation environment, the approximate GGN implementation documented in Sec. 2.2.3.

Table 4.4 Optimized launch power offset and tilt, GSNR offset, $\Delta GSNR$, and flatness, $\Delta GSNR$ max/min values for all investigated scenarios with various combinations of symbol rates, R_s, and slot widths, 32/64 GBaud and 50/75 GHz, respectively. Each column represents a different spectral configuration setup.

		Single band						Two bands						Three bands					
R_s [GBaud]	L	-	-	32	64	-	-	32	64	-	-	32	64	32	64	64	32	32	64
	C	32	64	-	-	-	-	32	64	32	64	-	-	32	64	32	64	32	64
	S	-	-	-	-	32	64	-	-	32	64	32	64	32	64	64	32	64	32
Power Offset [dBm]	L	-	-	-3.6	-0.6	-	-	-4.0	-1.0	-	-	-5.5	-2.4	-5.4	-2.4	-2.4	-5.4	-5.4	-2.4
	C	-4.1	-1.1	-	-	-	-	-4.0	-1.0	-5.2	-2.2	-	-	-5.4	-2.4	-5.4	-2.4	-5.4	-2.4
	S	-	-	-	-	-1.2	1.8	-	-	-1.3	1.7	-0.7	2.3	-1.0	2.0	2.0	-1.0	2.0	-1.0
Power Tilt [dB/THz]	L	-	-	0.2	0.2	-	-	0.4	0.4	-	-	0.6	0.6	0.7	0.7	0.7	0.7	0.7	0.7
	C	0.4	0.4	-	-	-	-	0.5	0.5	0.7	0.7	-	-	0.7	0.7	0.7	0.7	0.7	0.7
	S	-	-	-	-	0.0	0.0	-	-	0.1	0.1	-0.1	-0.1	0.1	0.1	0.1	0.1	0.1	0.1
GSNR [dB]	L	-	-	30.8	30.6	-	-	30.9	30.8	-	-	31.1	31.3	31.3	31.5	31.4	31.4	31.7	31.1
	C	30.6	30.3	-	-	-	-	30.2	29.8	30.3	30.2	-	-	29.7	29.5	29.6	29.5	29.8	29.4
	S	-	-	-	-	28.2	27.5	-	-	28.0	27.3	27.6	26.8	27.5	26.7	26.8	27.4	26.9	27.3
GSNR max/min [dB]	L	-	-	0.4	0.2	-	-	0.7	0.2	-	-	0.9	0.4	1.0	0.4	0.4	0.9	0.6	0.6
	C	0.3	0.3	-	-	-	-	0.4	0.2	0.7	0.3	-	-	0.7	0.2	0.4	0.4	0.4	0.5
	S	-	-	-	-	0.7	0.4	-	-	0.8	0.6	0.5	0.5	0.7	0.8	0.7	0.8	0.7	0.8

In Tab. 4.4, the results of the GA optimization method in all transmission scenarios investigated are reported. As mentioned in Sec. 4.1, this algorithm, in general, is extremely accurate compared to the proposed methodology and, therefore, serves as a reference ground truth for the validation.

First, it is worth noting that the difference between the optimized solutions with 32/64 GBaud symbol rates is due to the different spectral power densities of the transmitted spectra. In general, these differences are expected to be negligible when the PSD of each band is preserved, allowing flexible management of the spectrum allocation when a flat GSNR is in place.

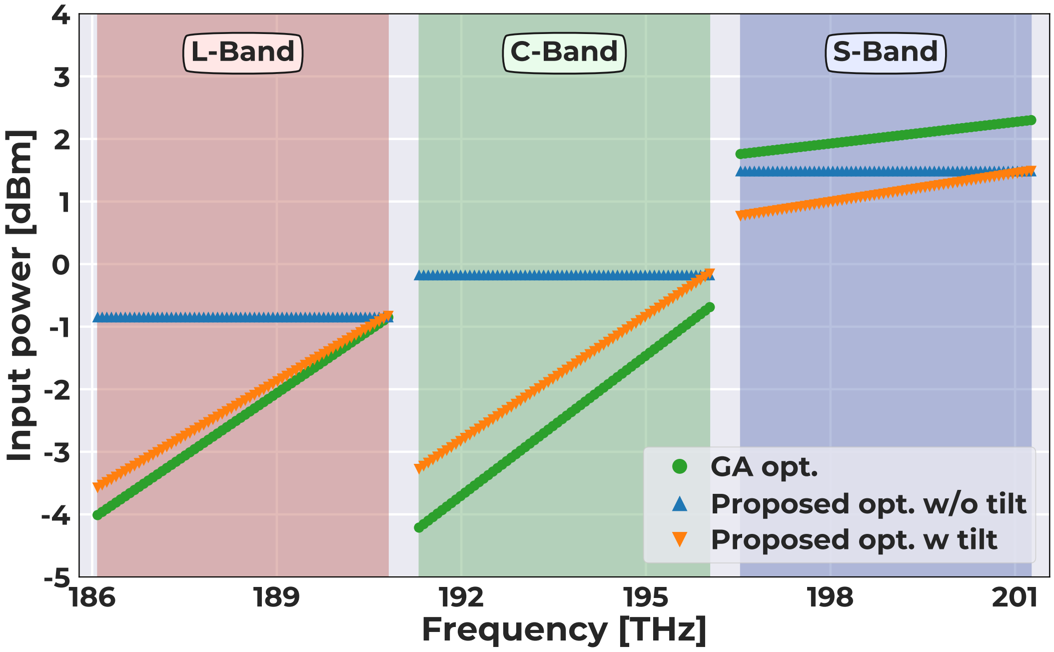

Fig. 4.18 Input power profile for C+L+S scenario using 64 GBaud and 75 THz of symbol rate and WDM grid, respectively, comparing the power optimization using the GA and the proposed method without and with applied tilt.

Regarding the validation of the proposed optimization procedure, first the optimal flat launch powers for each band is evaluated. In Fig. 4.18 and Fig. 4.19, the results of the multi-band extended LOGO are compared with the optimized launch powers and simulated GSNR obtained with the GA optimization. It can be observed that this approach already provides a promising optimized solution in terms of average GSNR. Nevertheless, a clear intra-band GSNR tilt is present that results in GSNR differences of up to 2 dB between channels within the same band. The GSNR flatness is an

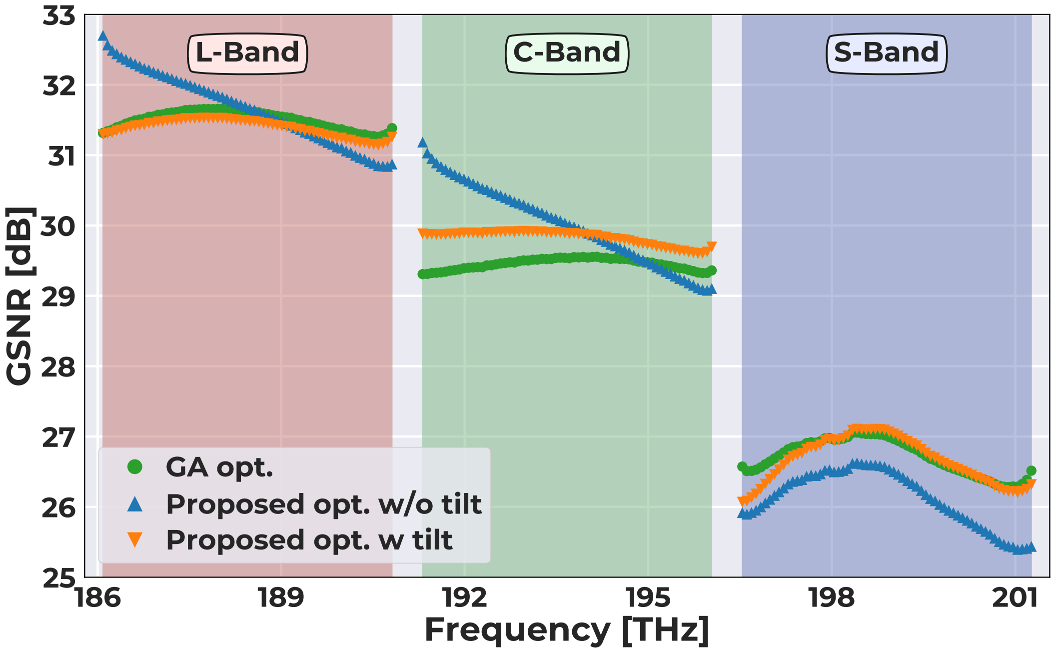

Fig. 4.19 GSNR profile for C+L+S scenario using 64 GBaud and 75 THz of symbol rate and WDM grid, respectively, comparing the power optimization using the GA and the proposed method without and with applied tilt.

essential requirement of the defined optimization strategy, therefore, a second step in the optimization procedure is proposed. Given the flat launch powers evaluated, $\tilde{P}_B$, a single simulation can be performed to find the residual intra-band GSNR tilts induced by SRS power transfer, whose results are shown in Fig. 4.19. In order to compensate for these residual intra-band GSNR tilts, an adequate power tilt can be applied at the launch power $\tilde{P}_B$ of each band. In particular, given an intra-band GSNR tilt, $T_{GSNR,B}$ defined as the GSNR difference in dB between the lowest and highest frequency channels within the band B, the following expression of the launch power tilt, $\tilde{T}_B$ is defined:

$$\tilde{T}_B = \frac{3}{2} T_{GSNR,B}\,, \tag{4.18}$$

where the 3 factor is due to the cubic root in Eq. 4.17, whereas, the 2 factor derives from a system rule of thumb applied when trying to compensate for the SRS effect in single-band transmission scenario. Additionally, as the performance of the worst-case-scenario channel (considering only the lowest and highest frequency channels within the band) depends on the powers of a neighboring band, instead of applying the tilt with respect to the band central channel, the tilt has to be applied to the worst-case-scenario channel itself, as shown in Fig. 4.18.

Finally, the result of the entire proposed optimization procedure is shown in Fig. 4.19, where the obtained GSNR is very similar to the result of the GA optimization. The proposed methodology is employed in all investigated transmission scenarios, obtaining highly satisfactory results in terms of both GSNR offset, $\Delta GSNR$, and flatness, $\Delta GSNR$ max/min. The differences between the GA optimization and the proposed methodology are reported in Tab. 4.5. It can be observed that these differences are always below 1 dB and in several cases the proposed methodology provides better results (negative values in Tab. 4.5) than the optimization results of the reference GA optimization.

Table 4.5 GSNR offset, $\Delta GSNR$, and flatness, $\Delta GSNR$ max/min differences between the GA optimization and the proposed optimization procedure for all the investigated scenarios with various combinations of symbol rates, R_s, and slot widths, 32/64 GBaud and 50/75 GHz, respectively.

		Two bands						Three bands					
R_s [GBaud]	L	32	64	-	-	32	64	32	64	64	32	32	64
	C	32	64	32	64	-	-	32	64	32	64	32	64
	S	-	-	32	64	32	64	32	64	64	32	64	32
ΔGSNR [dB]	L	-0.3	0.0	-	-	-0.6	-0.1	-0.4	0.1	0.0	-0.3	-0.1	-0.2
	C	-0.2	-0.1	-0.4	-0.1	-	-	-0.6	-0.3	-0.6	-0.4	-0.5	-0.4
	S	-	-	0.0	-0.1	-0.1	-0.1	0.2	0.0	0.1	0.1	0.0	0.2
ΔGSNR max/min [dB]	L	0.5	0.0	-	-	0.5	-0.1	0.7	0.0	0.0	0.6	0.2	0.2
	C	0.0	-0.2	0.4	-0.1	-	-	0.4	-0.1	0.1	0.0	0.1	0.2
	S	-	-	-0.3	-0.4	-0.4	-0.4	-0.2	-0.2	-0.3	-0.2	-0.2	-0.2

Chapter 5

Machine-Learning Aided Physical Layer Model

In this chapter, two examples of ML aided physical layer model presented in [105, 42] are documented. The aim of this project is to introduce and validate ML methods capable of accurately forecasting fluctuations in OLS OSNR induced by varying spectral load transmission. As anticipated in Sec. 2.3, EDFAs are designed considering a full spectral load configuration and their gain and NF profiles may vary significantly when only portions of the entire amplification bandwidth are loaded. Remarkably, no analytical expression has been established to describe the fluctuations that impact the overall degradation of OLS OSNR for each transmitted channel. Therefore, in this scenario, a data-driven approach based on ML algorithms is particularly advantageous as it provides accurate predictions of the overall OLS OSNR degradation for each transmitted channel with any spectral load configuration.

The proposed methodology has been validated through two experimental campaigns conducted at the Links Foundation in Turin, Italy.

5.1 ML predictions of Variable Spectral Load EDFA Fluctuations

To reduce the system margins [37], it is mandatory to rely on a quality of transmission estimator (QoT-E) that is able to reliably predict lightpath performance before its actual deployment, i.e., the generalized GSNR. The interaction between ASE noise and NLI [114, 115] occurs in the case of very low operational GSNR, namely for extremely long OLSs, which require several amplification points. These conditions are verified in submarine point-to-point networks, but have negligible effects within terrestrial networks. This investigation focuses on terrestrial regional and national backbone networks for which transparent propagation is over much smaller distances, meaning that considerable ASE-NLI interactions are not produced. Among the ASE noise and NLI contributions, the former is the most dominant, because it is twice the NLI when the system operates at optimal power [116, 117]. Remarkably, it is also the most challenging to estimate. In fact, the ASE noise magnitude depends on the working point of EDFAs [118], which in turn depends on the spectral load [119]. On the contrary, the NLI can be accurately predicted when the ASE noise accumulation is well characterized [120].

Therefore, the reduction of uncertainty in the OSNR prediction is crucial for accurate QoT estimation and, consequently, to enable the network controller to reliably deploy the lightpath at the minimum margin. As worst case margin scenario, a completely agnostic approach is assumed, by relying only on data coming from the optical channel monitor (OCM) available at the end of the OLS. In case of varying spectral load, EDFA frequency-dependent fluctuations induced by a mixed effect of physical phenomena [119] and implementation issues, meaning that an analytic approach is almost impossible to achieve in an open environment. In this scenario, ML techniques are very promising enabling a data-driven approach able to counteract uncontrolled fluctuations, as already effectively tested when managing optical networks; see [121–124] for performance monitoring applications, [125, 126] for prediction estimation of the ML approach and [127] for both. Overall survey of ML applied in optical networks can be found in [128, 129].

Focusing specifically on the quantification of EDFA uncertainties for margin reduction purposes, ML has previously been utilized to model EDFA gain [130, 131], noise figures [132, 133] and power excursions [121, 134], with [134] further demonstrating wavelength assignment using an algorithm that was able to recommend channel provisioning based upon the ML model results. Correction for EDFA gain ripple has also been targeted in [135, 136], with [136] further using monitoring information to significantly reduce the margin of a network planning tool based upon the GN model.

5.1.1 Approaches for QoT Estimation

In Fig. 5.1, three possible datasets, each representing a different level of knowledge of the OLS behavior, with each allowing a different reduction of the GSNR uncertainty. Typically (option (1)), some data is available from the static characterization of devices (e.g., calculating amplifier gain and noise figure in the frequency domain, connector loss, etc.) and is very significant for closed systems. By using this data and characterizing the OLS components, an accurate QoT-E can be implemented in vendor-specific systems. In particular, if all of the physical characteristics of the OLS are known, the OSNR may be calculated using Eq. 2.50. Nevertheless, this static data may be incomplete or inaccurate; even in a best-case scenario, the components experience degeneration due to aging, leading to an progressively unreliable QoT-E over time.

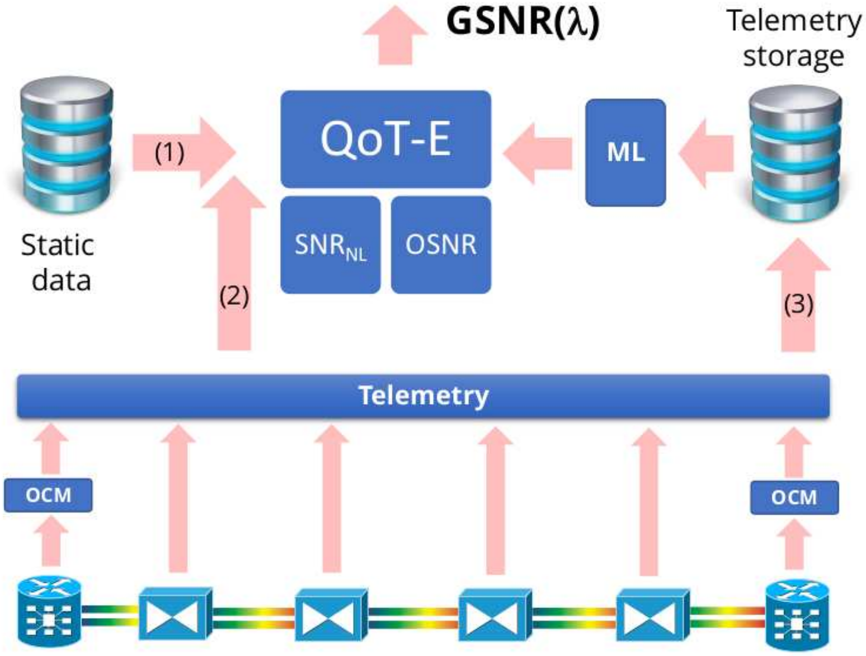

Fig. 5.1 General scheme for a QoT-E module predicting the GSNR(f). The three available datasets are shown: static data from device characterization (1), data from current-state telemetry (2) and stored data from historical telemetry that feeds a ML module (3).

A second possibility is that telemetry data concerning only the current network status is available (option (2)). Assuming an agnostic operation of the OLS (as is required in an open OLS) means that the OLS controller must mainly rely upon telemetry data originating from the OCM and the EDFAs. This approach does not require the knowledge of the device parameters and avoids the deterioration of the QoT-E accuracy due to aging discussed in option (1). In this case it is possible to use the telemetry data to estimate the OSNR response of the system by relying on the current parameter values. The problem of this approach is that the OSNR response is highly dependent upon the spectral load configuration, requiring a large margin, as can be seen from the analysis of the experimental dataset in Sec. 5.1.3.

Lastly, option (3) considers a dataset that collects the QoT responses to random spectral loads. This data can be generated before the in-service operation of the OLS, supposing the availability of a device which is able to supply the OLS with various spectral load configurations and measure the OLS response in terms of OSNR. As OLSs are typically bidirectional, it is conceivable that a two-port portable device operating as an ASE-shaped generator at the output port and an accurate OCM at the input port can be used to retrieve this data. Moreover, a future implementation considers the possibility of these devices being built into the ROADM nodes, which allows the data to be collected with periodical updates via streaming. Utilizing this dataset enables a QoT-E based on the OSNR response to specific spectral load configurations, increasing the accuracy of OSNR predictions with respect to option (2), where only telemetry data is considered. Additionally, this approach does not require the knowledge of the physical parameters of the OLS. This case provides an ideal scenario to apply ML, where the OLS is treated as a black box. In fact, a ML method using a training dataset composed of past spectral load realizations can yield an accurate prediction for every newly generated spectral load realization.

The focus of this work is option (3) and consider a realistic use case. Namely, a scenario where the OLS controller wishes to allocate a new lightpath over the CUT, given an existing spectral load. In particular, the level of OSNR associated with this new lightpath is investigated.

5.1.2 Experimental Setup

To obtain an experimental dataset, it has been design and implement the experimental setup depicted in Fig. 5.2, based on commercial EDFAs [137] used as black boxes. Span losses are obtained by variable optical attenuator (VOA) in order to focus only the OSNR and to avoid any NLI generation. The channel combs which provide

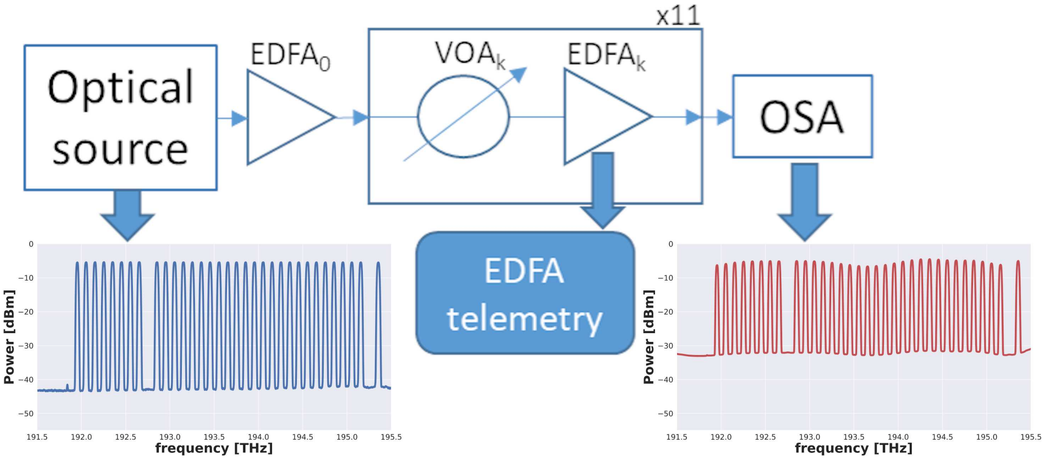

Fig. 5.2 Experimental setup: Here, the OLS under investigation is composed of an initial booster amplifier and a cascade of 11 spans, each containing a VOA and an EDFA. The input and output spectral power measurements obtained using an optical spectrum analyzer are shown in blue and red, respectively.

the OLS spectral load have been obtained by shaping ASE noise. This approach does not limit the generality of the results because of the large time constant that characterizes the physical effects within EDFAs. The output of the ASE noise source is shaped by means of a programmable optical WaveShaper© (1000S from Finisar) to generate a 100 GHz-spaced, 35-channel WDM comb centered at 193.5 THz, amplified by a booster amplifier (EDFA$_0$ in Fig. 5.2). The choice of the 100 GHz spacing was forced by the hardware availability, as well as the overall frequency domain under investigation, which was limited to 3.5 THz (35 channels, each with 100 GHz spacing). These restrictions do not limit the generality of the results, as the OSNR values do not change appreciably within each channel bandwidth and all criticalities concerning the EDFA amplification process are properly captured. The optical line is composed of 11 spans, each made of a VOA, with the optical span attenuation set to 10 dB, each followed by an EDFA that operates at a constant output power of -1 dBm per channel. For the EDFAs, MATLAB® control software has been developed to enable black box control. The OCM at the end of the OLS is mimicked by an OSA. OCMs that are currently present in ROADM nodes are not able to capture the noise floor due to their lack of sensitivity. As mentioned in the option (3) within the previous section, for a real application scenario it has been supposed the presence of a specific device that is able to measure both the channel powers and the noise floor, or, to update the current OCM presence on the ROADM nodes. Regarding the technical aspects of the data collection within this project, the experimental campaign lasted several days due to the OSA usage, which takes significantly longer than an OCM. Within a real application scenario the data collection process is expected to last the duration of a single night before the in-service operation of the OLS, producing the required amount of data needed for training the ML.

For every spectral load, input and output spectrum are measured in order to generate the final dataset. Specifically, the total power over each channel spectral bandwidth is measured, i.e., the noise floor if the channel is *off*, or the channel power if the channel is *on*. As a matter of fact, since the channel bandwidth (32 GHz) is less than half of the channel spacing, the noise floor is measurable even for the *on* channels, estimating their OSNR. An experimental dataset has been generated with 4435 cases representing different spectral load configurations. For clarity, let us define N_{on} as the number of channels in the *on* state in a distinct configuration. Given this definition, the dataset is composed of: a scenario with all channels *on* ($N_{on} = 35$), the 35 cases where only one channel is *on* ($N_{on} = 1$), and 140 configurations for each $N_{on} = 2,...,34$. This final set of configurations includes pairs of spectral loads which are identical, except for the CUT being either within the *on* or *off* state.

5.1.3 Statistical Analysis of Experimental Data

In this section, a statistical analysis of the OSNR fluctuations produced by different spectral loads is presented in order to obtain a quantitative estimation of the total OSNR uncertainty, given a static OLS (the OSNR values are calculated with a noise bandwidth of 12.5 GHz). Moreover, the experimental dataset is used as outlined in option (3) to acquire a prediction of the OSNR responses. To summarize the dataset characteristics, there are 4435 measurements of distinct spectral load configurations, which are a subset of the 2^{35} possibilities, given 35 channels. To populate the dataset, a sample of spectral load configurations which is uniform over the number of channels in the *on* state is selected. Moreover, for the set of configurations with the same N_{on}, the channels that are in the *on* state are chosen randomly, except for the CUT, which is equally divided between the *on* and *off* states. This specific dataset selection method is enacted in order to validate the prediction method on the CUT OSNR response. During the entire analysis, no uncertainties have been taken into account in the measurements, as they are negligible with respect to

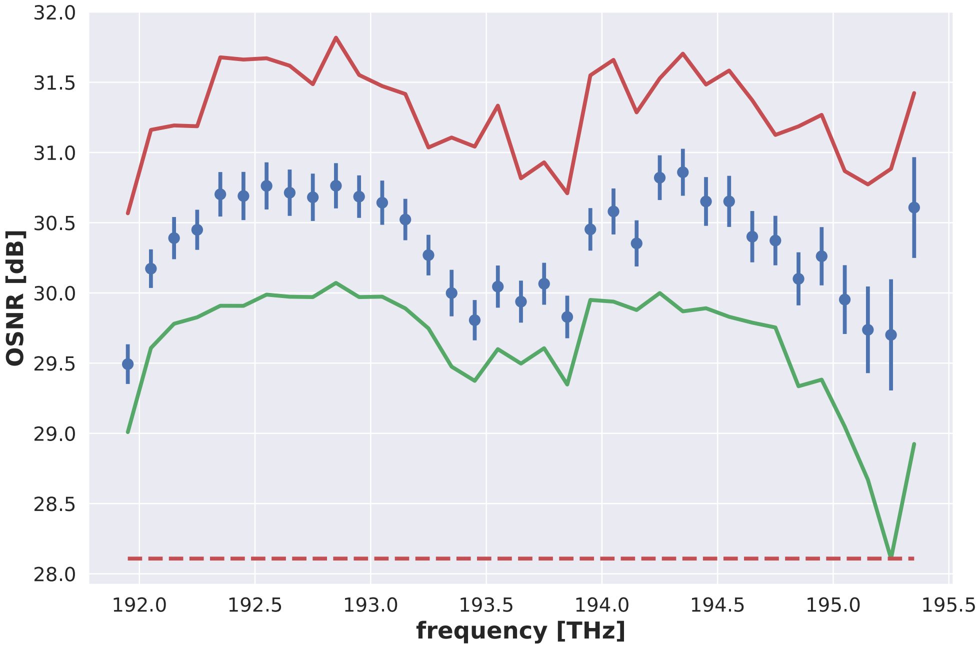

Fig. 5.3 Overall OSNR measurements in the frequency domain. The blue dots are the mean values over the entire sample for each channel; the error bars are equal to the standard deviations. In red and green the maximum and the minimum for each channel are outlined, respectively. The dashed red line indicates the overall OSNR minimum of 28.1 dB.

the characteristic variances of the system. A few basic considerations arise by calculating the average of the OSNRs for each channel over the entire sample, presented in Fig. 5.3. These OSNR averages sketch a characteristic figure of the EDFA amplification process, which takes place between 29.5 and 30.9 dB, with standard deviations from 0.14 to 0.40 dB. In order to learn more about the EDFA cascade behaviour, it is necessary to consider each configuration separately. In fact, the OSNR of each channel depends upon the state of every other channel within the spectral load. For example, as a primitive analysis in this direction, the OSNR distributions variation with regards to the number of *on* channels in the spectral load is investigated. Fig. 5.4 and Fig. 5.5 present the distributions enclosed in Fig. 5.3 for a select subset of channels, plotted against the total number of *on* channels in the configurations: here these figures show the means and standard deviations, σ, of the channels, respectively. It must be noted that because the dataset was further divided into chunks, the reliability of the averaged quantities is substantially decreased. This causes the standard deviation (presented in Fig. 5.5) to be far less

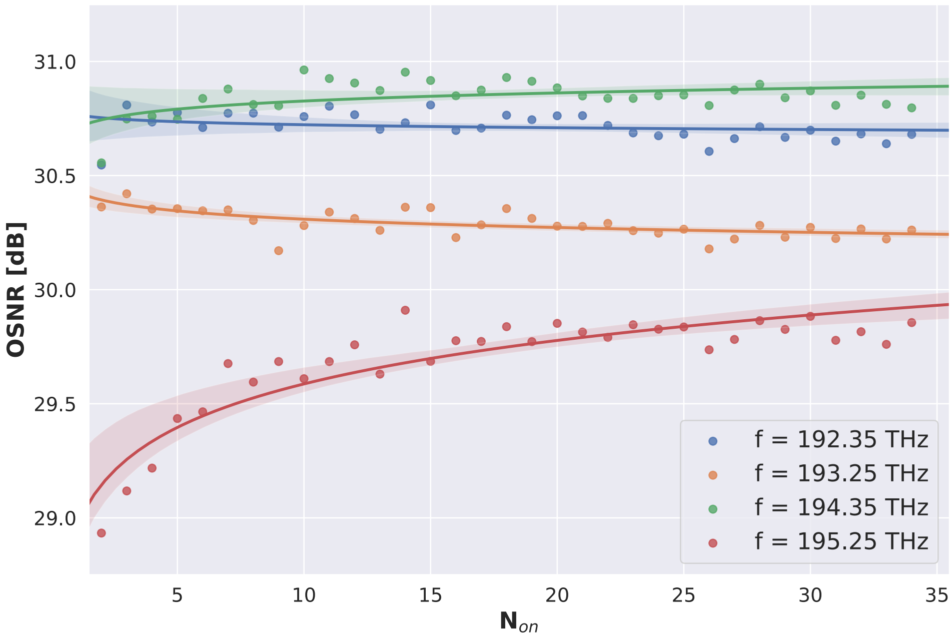

Fig. 5.4 The mean values of four channel OSNRs are plotted with respect to the configurations for an increasing N_{on}. The legend reports the central frequency of the channels considered. The colored lines and shaded areas are qualitative visual expressions of the trend of measured data.

uniform across all channels when only a small number of channels are in the *on* state. Regardless, Fig. 5.4 shows that for the CUT ($f = 195.25\,\mathrm{THz}$), there is an unquestionable increase in the OSNR as the line approaches a full load configuration. Moreover, for all channels σ decreases under the same conditions, meaning that the system tends towards a stable state. To further characterise the OSNR response with respect to a specific configuration, it is necessary to fully understand the intrinsic behaviour of the amplification phenomenon.

5.1.4 Physical Considerations

Despite it being possible to obtain a precise physical description of the emission phenomenon involved in the amplification process, without an accurate knowledge of the OLS physical parameters it is not feasible to determine the evolution of the spectral load through the EDFA cascade. In a general scenario, this obstacle would be exacerbated by the embedded EDFA software controller, which, in order to maintain

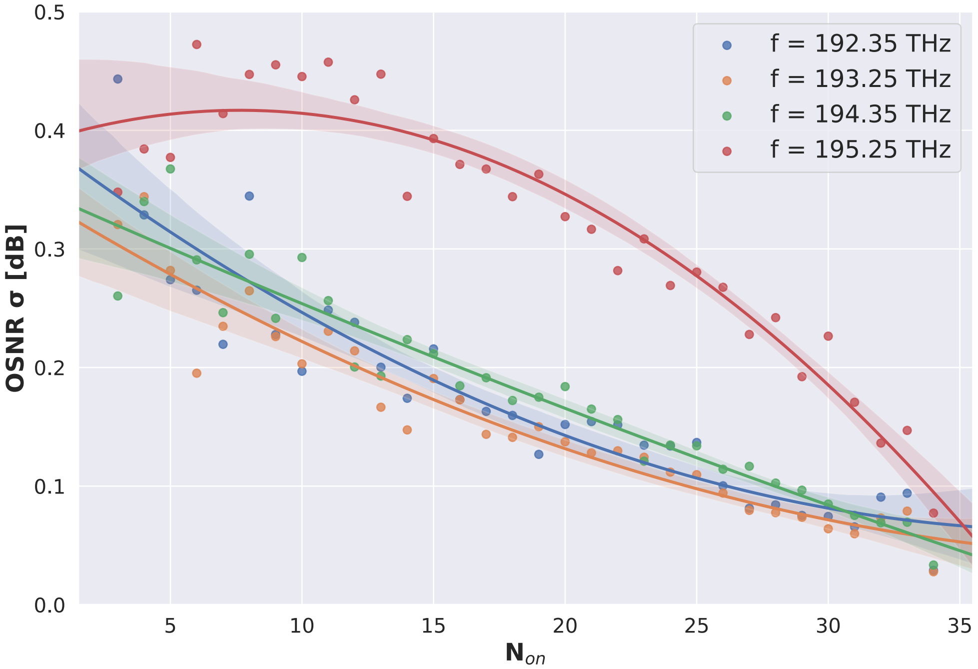

Fig. 5.5 The standard deviation values of the same configurations plotted in Fig. 5.4. As expected, the channel centred at 195.25 THz maintains the highest variance out of all of the configurations. The colored lines and shaded areas are qualitative visual expressions of the trend of measured data.

specific requirements, changes the spectral powers at the output of the amplifiers with an unknown algorithm. Properly addressing the cause of the OSNR fluctuations requires splitting the OSNR into its constituents: the received signal power and the ASE noise. An important point is that intensity of the signal amplification and the ASE noise are strictly related. Essentially, these quantities coincide with the stimulated and spontaneous emission of the amplifiers, respectively, and both depend on the population inversions of the erbium within the EDFAs [119]. As a rough summary, if no power is transmitted in a given frequency band, all the relative population inversion is utilized by the ASE noise, allowing it to reach a maximum value. In contrast, when the transmitted signal is amplified, a smaller amount of population inversion is present, resulting in a lower maximum noise value which may be attained. This effect is shown within Fig. 5.6, where two spectral load configurations are considered. Here, a clear reduction in ASE noise is observed by switching an extra channel *on*. This is the case for all channels, with the minimum amount of ASE noise being achieved when all channels are in the

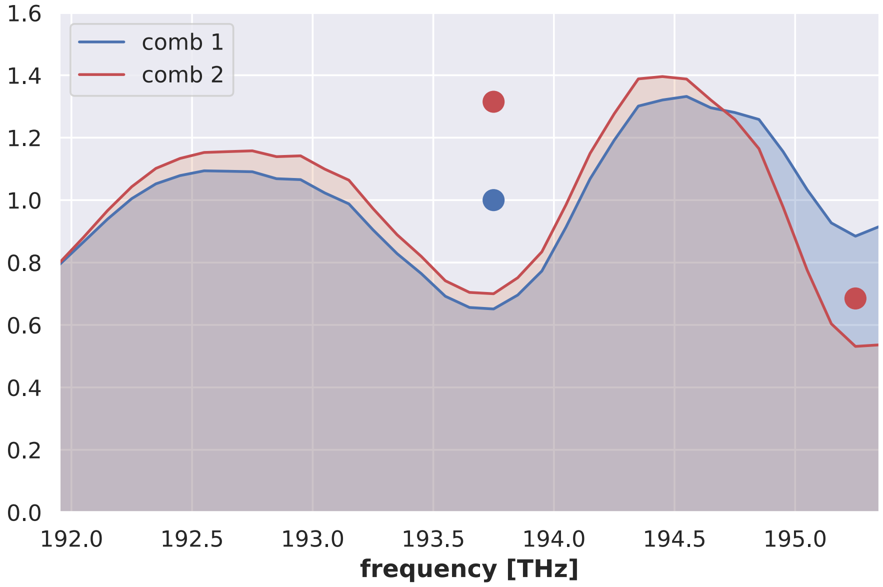

Fig. 5.6 A qualitative visualization of the OSNR fluctuations which arise from turning on a new channel, for both the ASE noise (shaded lines) and the power of the *on* channels (dots). Here, the $N_{on} = 1$ case is given in red, and the $N_{on} = 2$ case is given in blue. In this figure, all quantities are normalized in order to have a unitary mean value.

on state. Furthermore, it should be noted that among all possible configurations, the example shown in Fig. 5.6 experiences the wildest change in noise figure. In fact, the channel switched to the *on* state has a frequency bandwidth centered at 195.25 THz, with a frequency close to the peak of the well-known spectral hole burning phenomenon [119]. Likewise, this behavior is also reflected by the large OSNR variance of this channel. Revisiting the dataset, this feature is pictured in Fig. 5.7, where the standard deviations of the overall OSNR measurements for each channel are plotted. Furthermore, in Fig.5.6 it can be observed that even though channels have a frequency spacing of 32 GHz in this experiment, changing a channel to *on* can affect the power of the noise upon frequency bandwidths hundreds of GHz away. Since the EDFA energy level population inversion quantifies the intensity of both the amplification and of the noise, it can be concluded that the state of a single channel impacts both the signal power and the ASE noise of channels within its frequency neighborhood. This cross-dependency between the power of the channel and the ASE noise, which depends on the state of the other channels, means that calculating the OSNR of every channel is challenging; this is not an intrinsic value

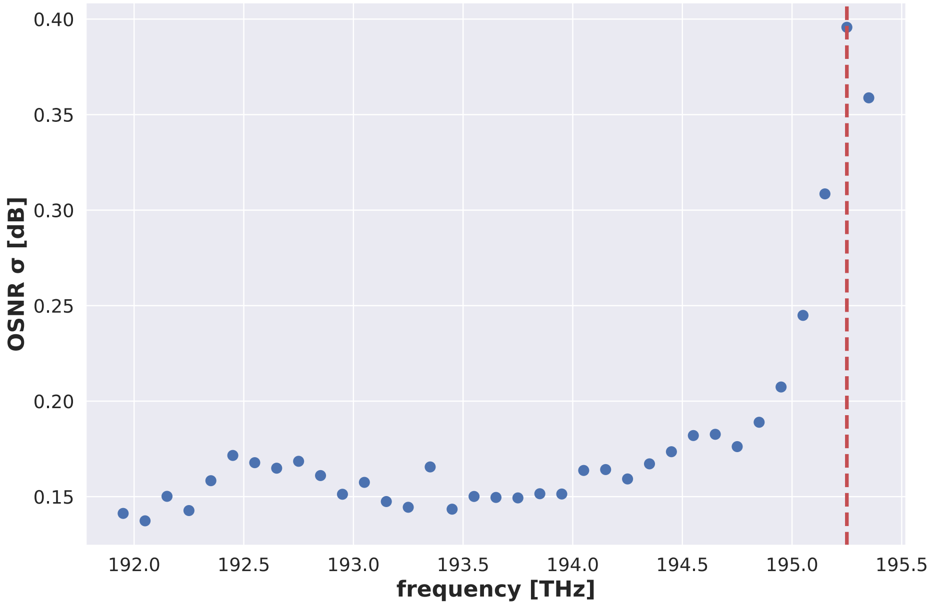

Fig. 5.7 The standard deviation trend over all of the channels, highlighting an increase as the OSNR approaches the frequency where the peak of the spectral hole burning occurs, given by the dashed red line in the figure.

of the channel, but of the entire spectral load. Due to the above considerations, it is not possible to further characterize the OSNR response for a particular configuration if the the parameters of the OLS are not accurately known.

Apart from the statistical description of the entire dataset and the heuristic analysis on OSNR fluctuations, this dataset is used as grounds for a realistic use case. In general, the required margin must be conservative and take into account the OSNR fluctuations and depends upon the needs of the OLS operators; to be agnostic with respect to these needs and to compare different prediction methods in a fair manner, an estimation of the average margin is quantified by calculating the RMSE, given by:

$$\mathrm{RMSE} = \sqrt{\frac{\sum_{i=0}^{N}\left(\mathrm{OSNR}_i^{\mathrm{r}} - \mathrm{OSNR}_i^{\mathrm{p}}\right)^2}{N}}, \tag{5.1}$$

where $\mathrm{OSNR}_i^{\mathrm{r}}$ and $\mathrm{OSNR}_i^{\mathrm{p}}$ are the measured and predicted values of the CUT OSNR for the ith spectral load, respectively, and N is the dimension of the test dataset. If nothing is known about the OSNR dependency upon frequency, the same OSNR threshold must be implemented for all channels with a magnitude lower than an overall expected minimum. In this case, the $\mathrm{OSNR}_i^{\mathrm{p}}$ are set to the constant OSNR threshold of 28.1 dB, producing an average margin of up to 2.28 dB over a set of realizations equivalent to our sample.

Supposing the availability of stored data that describes the frequency-resolved OSNR response (option (3)), one can reduce the margin by setting a minimum value for each channel that must lie beneath the respective minimum measurement (the continuous green line in Fig. 5.3). Although this solution is sub-optimal, it is the best achievable result which is conservative and agnostic in regards to the specific spectral load configuration. This solution produces a limited improvement, compared to the initial value of 2.28 dB, as the average margin would lie between 1.72 dB and 0.46 dB, depending upon the channel. This result can be further improved by characterizing the OSNR fluctuation dependency upon the specific spectral load configuration; as the user knows the number of *on* channels for a given spectral load, they can set the threshold as the minimum value of the OSNR measurement for the given N_{on}. The result of this approach produces an RMSE which lies between 1.22 and 0.09 dB for the CUT (worst case scenario), shown in Fig. 5.8. These improvements would reduce the margin in an effective manner, however, being highly dependent upon the sample features, their accuracy is limited by the statistical incidence of the sample over all possible realizations of the system. This means that having a reliable value for each channel may require considering a large number of instances. In light of this, a ML approach appears to be an appropriate candidate to increase the accuracy of OSNR predictions, if the dimensions of the sample are fixed.

5.1.5 Machine-Learning OSNR Prediction

The prediction of the OSNR based upon a specific spectral load configuration is an ideal scenario for ML, especially within a case where the OLS is treated as a black box, as ML can compensate for the lack of knowledge regarding the OLS parameters. To gauge the effectiveness of the ML approach, a real case scenario is taken into account. The aim of this project is to enhance the accuracy of predicting OSNR through implementing ML techniques within the given scenario. First, it is essential to partition the measurement dataset into training and testing subsets. The former represents the stored dataset on which the OLS controller can base the OSNR

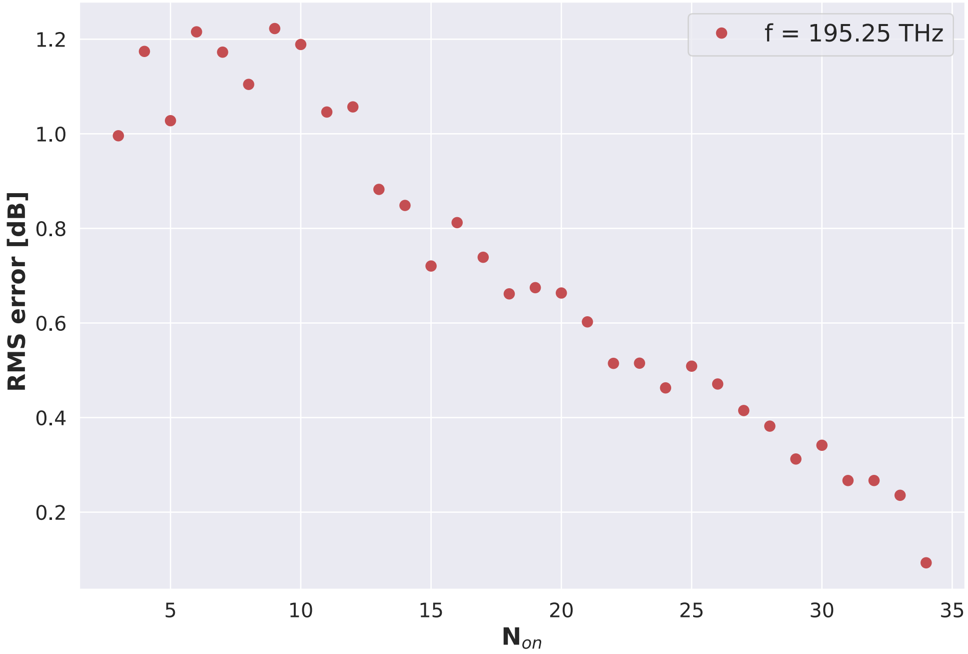

Fig. 5.8 The RMSE for the worst-case scenario channel, with an increasing number of channels in the *on* state within the configuration, obtained considering the respective minimum measured OSNR value used as a margin threshold.

predictions for a lightpath that will be allocated to the CUT. The latter represents a set of real outcomes which can be used to validate the accuracy of a particular prediction method. To estimate this accuracy the RMSE is used, considering $\mathrm{OSNR}_i^{\mathrm{r}}$ and $\mathrm{OSNR}_i^{\mathrm{p}}$ as the measured and predicted values of the CUT OSNR, restricted to the test subset of the dataset. Setting a constant $\mathrm{OSNR}_i^{\mathrm{p}}$ for all i as the minimum measured value of the CUT OSNR yields a value of 1.63 dB RMSE over all the configurations in the test dataset. Following this, the well-known TensorFlow© platform [138] enable performing ML, adapting various high-level features from this platform according to our requirements.

Before proceeding with implementing a ML technique to predict the OSNR of an OLS, preliminary investigations are undertaken at first in order to probe whether a neural network or a linear regression model provides superior performance – as a result the DNN implemented in TensorFlow© has been chosen; it is a feed-forward multi-layer (deep) neural network, because it outperforms a linear regression model in this scenario. Applying the DNN model to the collected dataset, various levels of accuracy are obtained depending on the DNN parameters. This DNN model is characterized by a proximal Adagrad optimizer (again, implemented in TensorFlow© [138]) with a fixed learning rate of 0.1 and a regularization strength of 0.001. Most importantly, the number of hidden layers and nodes have been tuned in order to achieve the best trade-off between precision and computational time. These two parameters are linked to the complexity of the DNN, which in turn is tied to the complexity of the problem to be solved. Although increasing the number of layers and nodes improves the accuracy of the DNN, raising these values also has an adverse effect on computational time. In the end, a DNN with 3 hidden layers have been selected, containing 32 nodes each, taking approximately 8 minutes to train (using a machine running with 32 GB of 2133 MHz RAM and an Intel® Core™ i7 6700 3.4 GHz CPU), as increasing DNN complexity does not further improve the accuracy of the OSNR estimations. These quantities should be changed when considering a system with a larger number of amplifiers, with the computation time increasing accordingly. Once the model has been trained it can be validated and utilized for any possible spectral load configuration, within the overall investigated bandwidth, for the OLS under consideration. Considering a single CUT (with $f = 195.25$ THz), 30% of the dataset is designated as a testing subset. Due to the CUT being close to the spectral hole burning peak, this is a worst-case scenario for OSNR fluctuations, therefore, lower error predictions are expected for all other CUT selections. The testing subset was created by randomly choosing instances from the dataset, with the only requirement being that the uniformity of the distribution with respect to the number of *on* channels in the configurations was preserved. This means that, for each configuration subset with a given N_{on} the 30% is selected to be in the test dataset. DNN training and prediction processes require the definition of features and labels, which indicate system inputs and outputs, respectively. As outlined in the previous section, the uncertainty of the system can be divided along the variances of the received signal power and the ASE noise. Therefore, these two quantities are considered as independent inputs of the system and set them as the DNN features. Correspondingly, the OSNR is the only system output under investigation and so is set as the DNN label. In order to properly address the aforementioned realistic scenario, the DNN features correspond to the quantities measured when the CUT is *off*, whereas the labels correspond to the CUT OSNR when the CUT is in the *on* state. As a consequence of this restriction, the final dataset composed of the training and testing subsets is half the size of the original dataset.

Fig. 5.9 illustrates the distributions of the measured OSNR for the CUT and the predictions of the DNN over the test dataset. This figure highlights how the DNN predictions closely resemble the measured OSNR values, having a similar mean, μ, range and standard deviation, σ. An average margin of 0.15 dB is obtained through this DNN estimation of the CUT OSNR, which is a significant improvement with respect to the previous solutions presented at the end of the previous section. To properly frame these results in the realistic use case scenario, it must be underlined that despite the DNN providing a high level of accuracy, it may make predictions which are not conservative. For example, in this case 38% of the predictions are greater than the real values, even if the majority are greater by a marginal amount. This percentage of non-conservative predictions may be reduced by shifting the OSNR estimations of the DNN by a fixed amount. For example, to reach a scenario where less than 6% of the predictions are non-conservative, the DNN estimations must be shifted by a factor of 0.2 dB, giving an RMSE of 0.27 dB, which still remains a significant improvement over the initial average margin estimations. Furthermore, it should be stressed that the dataset used in this work contains less configurations where a small number of channels are *on*, visible in Fig. 5.10. The result is that these scenarios are underrepresented in the training dataset, causing the accuracy

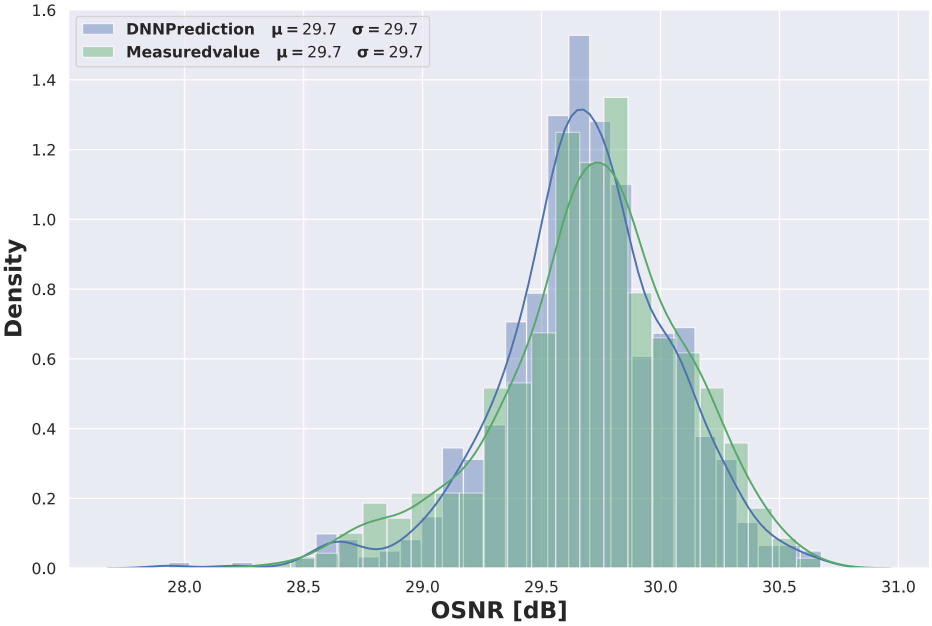

Fig. 5.9 Comparison of the OSNR distributions of the DNN guesses and the measured values, respectively.

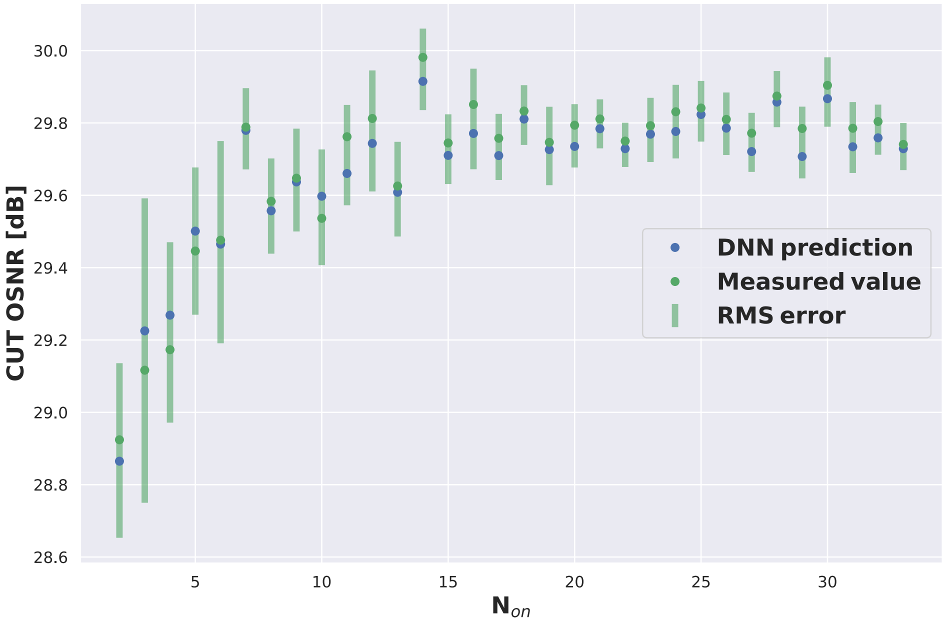

Fig. 5.10 Comparison of the OSNR averages of the DNN guesses and the measured values, respectively, presented in terms of the number of channels, N_{on}. The RMSE is indicated with the error bars.

of the DNN predictions to be lower when $N_{on} < 10$; ensuring that these cases are represented equally would reduce the overall RMSE. Additionally, Fig. 5.10 reveals that all non-conservative cases in this investigation were given when $N_{10} = 10$ or less, further stressing that the criticalities of the DNN prediction depends upon the statistical incidence of the sample over all possible realizations. In light of these results a ML approach exhibits promising accuracy, and it seems that with further, more in-depth parameter selection and training that the DNN may eventually lead to an OSNR margin estimation that approaches zero, at least for similar use cases.

5.2 ML Aided QoT-E Based on GNPy

The ML implementation within this study is performed in a similar way to the previous work [105], described in Sec. 5.1. The objective is the creation and assessment of an overall GSNR QoT-E built from two constituent models; with the SNR $_{\text{NL}}$ contribution being modelled with GNPy, and the OSNR contribution being predicted using two DNNs, estimating the P_{λ} and $P_{\text{ASE};\lambda}$ for each channel across an entire spectrum, no matter the spectral load configuration. This approach has been validated through an experimental campaign, comparing the estimated end-of-line GSNR degradations to real QoT measurements, demonstrating the enhancements that result when combining an analytical QoT-E approach, in this case the GNPy, with a ML algorithm that provides an accurate GSNR prediction. Additionally, the approach taken within this investigation can be applied to next-generation SDN network management scenarios, pursuing an ultimate goal of a fully automated network without human input. As examples, an experimental implementation of an observe-decide-act (ODA) loop utilizing a ML algorithm is performed in [139, 140], a tutorial showing how similar ML implementations may contribute to an automated network architecture in [141], along with a demonstration for a ML-based monitoring system for a fully disaggregated ROADM implementation in [142].

5.2.1 Experimental Setup

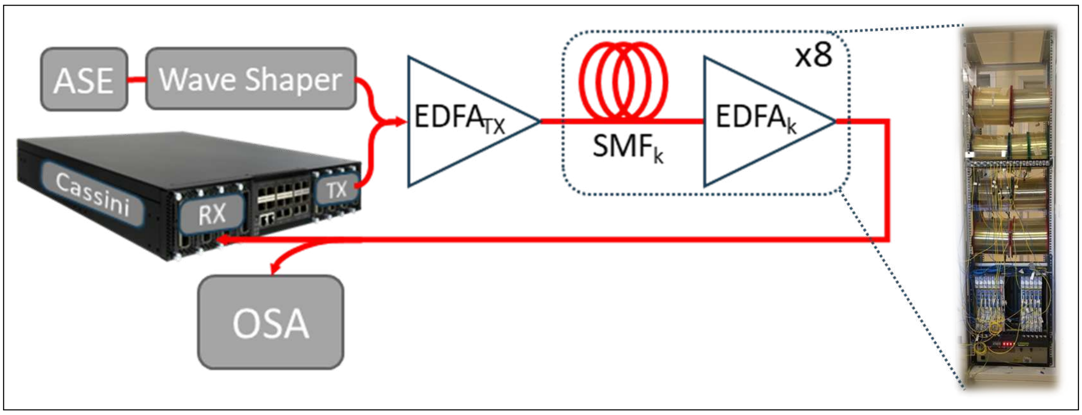

Fig. 5.11 A schematic representation of the experimental setup described within this work.

The experimental setup depicted in Fig. 5.11 was created connecting 9 commercial EDFAs and 8 fibers that are characterized by distinct physical parameters. Starting from the transmitter, the OLS begins with a booster amplifier that is set to produce a flat, constant power value of -1 dBm for each channel (regardless of the spectral load configuration), followed by 8 fiber spans, each approximately 80 km long, with a mixture of single mode fiber types, each followed by a commercial EDFA [143] operating with distinct and constant gain and tilt values. To generate the input spectral loads, an ASE noise source has been manipulated using a commercial programmable WaveShaper© (1000S from Finisar) obtaining a 80 channel

WDM comb, centered at 193.3 THz with a WDM grid spacing of 50 GHz within the C-band, according to ITU-T specifications [144]. Two CUTs, centered at 191.65 and 194.95 THz, are considered and addressed as CUT 7 and CUT 73, respectively, given their cardinal position in the WDM comb. For these CUTs, the signal transmission is managed by a commercial AS7716-24SC Cassini device [145], along with a CFP2-DCO coherent module from Lumentum, that is able to generate and detect either a 32 GBaud, QPSK modulated signal or a 43 GBaud, 8-QAM modulated signal.

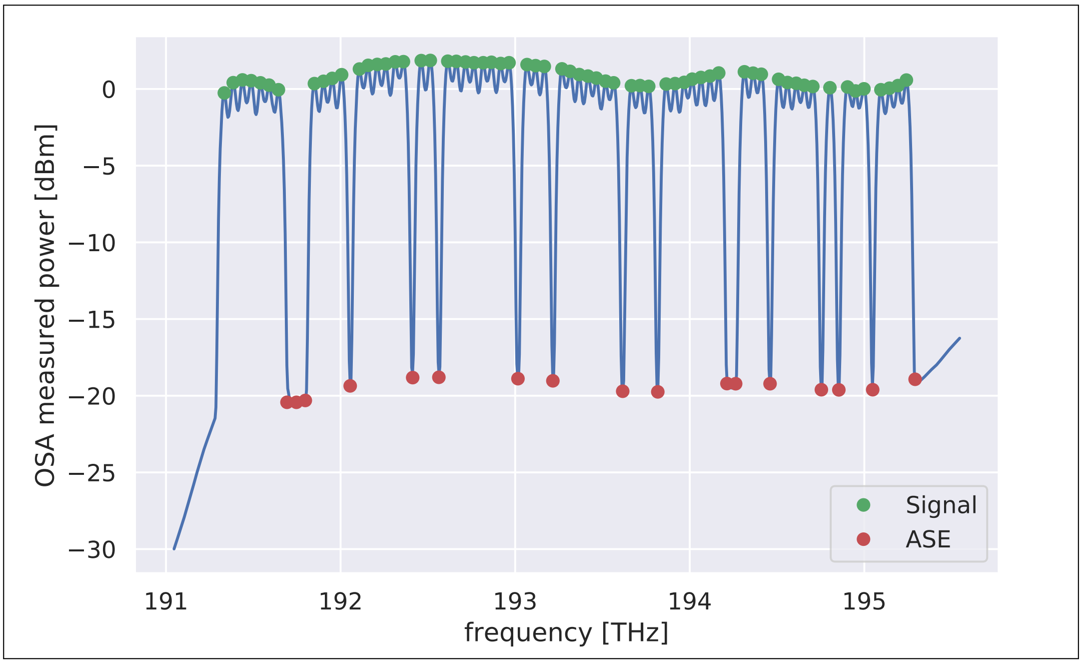

Fig. 5.12 The power measured using the end-of-line OSA for one of the 2520 spectral load configurations. Channels which are turned on provide signal power measurements, whereas channels which are turned off provide ASE noise power measurements.

An OSA has been placed at the end of the OLS to emulate the OCM at the ROADM input and output. Within this experimental framework, 2520 different spectral loads have been generated, iterating through various scenarios where a different number of channels are turned on. In each scenario, permutations that represent unique spectral load configurations are generated, between a minimum of 2 channels turned on up to the maximum spectral load case of 80 channels. For each of these configurations, the power levels of all 80 channels are measured, obtaining the signal power if the channel is turned on and the ASE power if the channel is turned off; an example spectrum power measurement performed using the OSA is shown in Fig. 5.12. In this procedure, the FWM component of the NLI impairment is considered negligible for all the fiber varieties under investigation, as verified in [106, 105]. Furthermore, for all spectral load configurations the BER in transmission associated with the specific CUT is measured. From these quantities a quantitative estimation of the GSNR is obtained by inverting the BER vs the OSNR curve, obtained through a progressive B2B noise loading characterization [146].

5.2.2 Optical Line System Characterization

In general, a digital model requires a comprehensive description of the line physical parameters for accurate QoT predictions. In particular, the physical parameters of the fiber spans were unknown before initiating the experimental campaign. As a preliminary analysis, an optical time domain reflectometer (OTDR) has been used to probe the lengths and α values of the fiber spans within the link at the OTDR pulse frequency, 193.414 THz. The power measurements at the fiber termination suggested that the OTDR measurement of α for the probing frequency was not enough to properly simulate the fiber loss as an unexpected power tilt was observed at the fiber termination. This was due to characterization inaccuracies of both the spectral fiber loss coefficient profile, initially considered flat in frequency, and the efficiency curve of the SRS. To overcome this, given a model for both α and g_R, an optimization algorithm [47, 103] was implemented enabling the joint characterization of these parameters that best matches the experimental signal profile of the full spectrum scenario.

Regarding the SRS contribution, a fixed, normalized efficiency curve [49] multiplied by a fiber span-dependent Raman coefficient, C_R, with the resulting SRS efficiency curves shown in Fig. 5.13(a). Regarding the frequency-dependent α profile, the model expressed in Sec. 2.2.1 has been utilized.

In Fig. 5.13(b), an example of the optimized α and its separate contributions against wavelength, λ.

This approach allowed the fiber α and g_R values to be estimated to a satisfactory level of accuracy. Furthermore, the resulting g_R allow the different fiber types to be classified and enable distinct dispersion coefficients, D to be set. As nonlinear coefficient value, a single value has been considered for all the fibers, $\gamma = 1.27$ $\mathrm{W}^{-1}\,\mathrm{km}^{-1}$. The results of the described characterization procedure for all fibers within the OLS are reported in Tab. 5.1.

Table 5.1 Fiber configurations tested within this experimental campaign.

#	$\bar{\alpha}$ [dB/km]	D [ps/(nm·km)]	C_R [(W·km)$^{-1}$]	L [km]
1	0.191	16.7	0.42	80.4
2	0.194	3.8	0.54	80.4
3	0.188	8.0	0.6	80.6
4	0.196	4.4	0.73	79.9
5	0.199	4.4	0.6	79.8
6	0.210	4.4	0.73	75.8
7	0.189	3.8	0.44	66.8
8	0.187	16.7	0.54	78.6

Table 5.2 EDFA configurations tested within this experimental campaign

#	Gain [dB]	Tilt [dB]
0	19.8	0.2
1	16.9	1.4
2	16.5	1.4
3	17.9	1.4
4	19.1	1.4
5	18.7	1.4
6	17.3	1.6
7	18.7	1.4
8	20.6	1.4

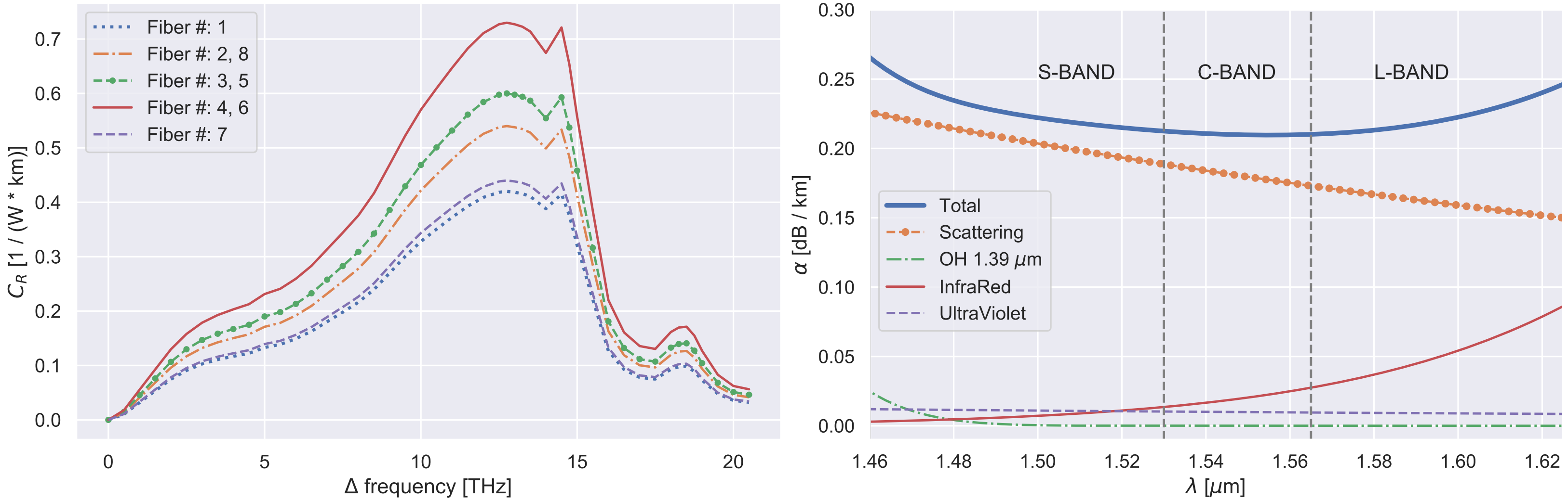

(a)

(b)

Fig. 5.13 (a) Final SRS efficiency curves deduced and used for each fiber span.(b) A generic loss coefficient profile and the related four model contributions.

5.2.3 ML and GNPy for QoT Estimation

As a follow-up of the approach presented in [105], an ML algorithm has been implemented, enhancing QoT computation over the OLS under investigation by means of a significant reduction of OSNR estimation inaccuracies. Firstly, it is worth underlining that, with the considered monitoring equipment, the application of ML must be restricted to the OSNR contribution of the total GSNR, as the SNR $_{\text{NL}}$ can only be measured if the channel transports a modulated signal; creating a training dataset before traffic deployment is unfeasible within the considered network framework. Moreover, various mathematical models, have been shown to provide a precise estimation of NLI impairment due to fiber propagation, dependent upon certain physical parameters being given with a required level of accuracy. In this framework a ML approach provides the greatest benefit when used to reduce uncertainties that are often accounted for simply through use of a design margin. Such uncertainties include the aging of optical components, a lack of device characterizations, inaccuracies due to estimations made by proprietary software and fluctuations in the amplification process which are unaccounted for by the current model in question. It is worth noting that the ASE noise measurements, which are carried out when the channel is turned off, is a biased estimator of the actual ASE noise that affects the channel when it is turned on. Nevertheless, the bias in this prediction decreases significantly as the number of channels contributing to the spectral load increases – this value is always an overestimation that results in a conservative QoT prediction. As the spacing of the channels prevents measurement of the ASE noise within the channel frequency neighborhood, the ASE noise may only be measured for a given channel when the channel is turned off.

Considering the ML algorithm implemented within this work, the dataset is normalized and divided into training, validation and testing subsets, making up 60%, 10% and 30% of the total dataset size, respectively. Using the open source TensorFlow© library, a DNN model has been implemented consisting of 4 hidden layers, each including 512 nodes; these values have been found to be optimal from the validation process, providing a satisfactory trade-off between the accuracy of the ML predictions and the overall training time. The computer used to run this training procedure contained a quad-core Intel® Core™ i7-8565U CPU running at 1.80GHz, along with 8 GB of RAM, giving a total training time for each DNN of approximately 6 hours.

In order to estimate the OSNR, two distinct ML models have been trained, predicting the signal and ASE noise power levels, respectively. As the spectral load changes for every measurement within the dataset, it is important to choose a suitable set of features that serve as DNN inputs, as well as suitable outputs. Considering first the feature requirements, these must be fixed before the training process is started and cannot be changed once they have been chosen. These features used for the training stage must correspond to known system variables to obtain any individual prediction of the DNN outputs. Therefore, by exclusion, the entire set of power measurements can be used uniquely as DNN outputs, as they are not known for any individual spectral load. The only information that is known before a prediction is made are the channel statuses, which are either on or off. This information is relatively limited with respect to the entire realization space of both the signal and ASE power levels and leads to a low accuracy prediction.

In order to increase the DNN prediction performance the following methodology, presented diagrammatically in Fig. 5.14, has been applied. Firstly, the ML models are fed with the array of channel statuses, along with the signal and the ASE noise predictions obtained using the GNPy – this enriches the input information, providing a partial insight of the OLS responses to specific spectral loads. Secondly, DNN training process is performed over the entire spectral load, requesting information over all channels, not only the CUTs. As the number of channels varies between distinct spectral loads, the number of DNN outputs is set equal to the maximum number of available channels within the system under investigation. As the node weights are shared among the DNN outputs, specific channel predictions are tuned by considering the entire spectrum; consequently, precise information provided by the measurements is propagated through the entire DNN.

A straightforward issue is that when a channel is turned on, the signal power can be measured, however, the power of the ASE noise cannot. On the contrary, when a channel is turned off, by definition there is no signal power, but the ASE noise power can be measured. A naive solution is to set the unmeasured channel power quantities to zero during the training procedure. In the proposed implementation a better solution is achieved leveraging the correlation between the spectral profiles of the signal and ASE noise power levels at the OLS output. As a matter of fact, both of these quantities are subject to the same gain and loss profiles during propagation and can be combined, creating two unique, normalized and power arrays, with the proper dimension, which maximize the information supplied to the DNN. These two arrays

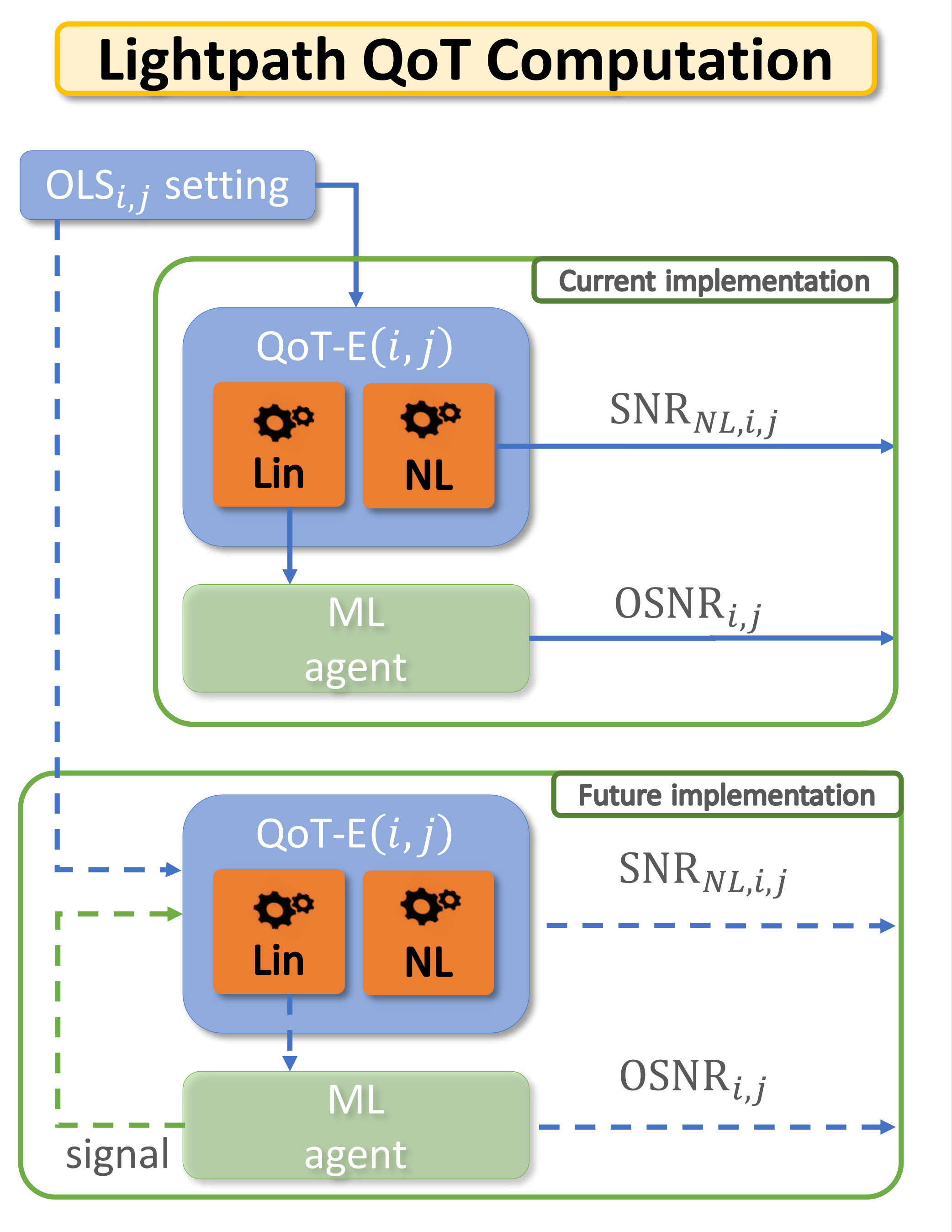

Fig. 5.14 A description of the ML process used within this work; after the OLS$_{i,j}$ settings are provided, the linear components (the signal and ASE noise powers) are supplied to the ML agent, whereas the NLI component is estimated using the GNPy engine. A future implementation scenario is also shown.

of artificial quantities are used, respectively, for the prediction of the signal and ASE noise powers. Considering the signal power inputs and outputs, the missing elements in the array of signal powers, corresponding to the channels turned off, are filled with the rescaled ASE noise powers. For the ASE noise power inputs and outputs, *vice versa*, all missing elements are replaced with rescaled signal power values.

With this strategy, each DNN has a total of 160 inputs and 80 outputs; the inputs are composed of 80 channel statuses, combined with 80 power level estimates of ASE noise or signal power (depending upon the DNN model), whereas the outputs represent 80 power level values. Enhancing the ML implementation in this way enables accurate predictions of both the signal and ASE noise powers and hence a precise OSNR estimation to be obtained.

5.2.4 Overall QoT Prediction

In this section, first the ML predictions are presented as results obtained for a testing dataset containing 808 different spectral load configurations. As accuracy metrics, alongside the RMSE definition in Eq. 5.1, also the difference between the measured and predicted quantities is considered:

$$\Delta X = X^m - X^p \,. \tag{5.2}$$

As a first demonstration of the benefits in utilizing a ML approach, the DNN accuracy is assessed, estimating the signal and ASE noise power levels over the entire spectrum and compared with the corresponding results obtained using the GNPy. Regarding the signal power predictions, RMSE values ranging between 0.2 and 1.5 dBm were found using the GNPy (depending upon the channel under investigation). Using instead a ML approach, the RMSE values ranged between 0.2 and 0.3 dBm, demonstrating an increase in prediction accuracy. Similarly, considering the ASE noise power predictions, the RMSE range prediction is reduced from 0.5 to 1.5 dBm to 0.3 to 0.4 dBm. A qualitative insight of this accuracy improvement is shown in Fig. 5.15, where the signal and ASE noise results are reported for both prediction methods, illustrating the error distribution as a vertical colored strip for each channel, with brighter colors representing a higher distribution density, and vice versa. This figure serves as a qualitative visualization – the real error distributions have been replaced by equivalent Gaussian distributions with the same mean and standard deviation values. Nevertheless, Fig. 5.15 presents some interesting conclusions: firstly, applying ML moves the error distributions into a dense region of values concentrated around a zero mean, for both the signal and ASE noise power predictions, representing the best feature for a generic estimator. It is also visible that the higher RMSE values obtained using the GNPy are due to a biased estimation rather than incorrect modelling, as the error distributions maintain a limited standard deviation for every channel. This bias can be attributed to the fluctuations of the ILA responses to different spectral loads, which cannot be modelled in advance and consequently cannot be accounted for in the GNPy simulation. Moreover, the GNPy power predictions feature an increasing uncertainty as the characteristic spectral hole burning frequency (approximately 195 THz) is approached.

Regarding the overall GSNR, it has been measured only for the CUTs, as it requires modulated signal to be estimated, and in what follows the analysis is restricted to the two CUTs. As expected, through investigation of the dataset, the OSNR and SNR $_{\text{NL}}$ covariance is non-trivial. Therefore, in order to have a fair estimation of the enhancement provided by the ML approach, first the prediction accuracy of the OSNR are discussed. Fig. 5.16 - 5.17 illustrate the error distributions of the OSNR predictions obtained with and without the ML models, for both CUTs. In this case, the ML methodology reduces the RMSE of the OSNR from 0.5 to 0.2 dB for CUT 7 and from 0.7 to 0.2 dB for CUT 73.

Finally, the final GSNR prediction obtained by applying the proposed methodology described in Fig. 5.14 is investigated. Fig. 5.18 showcase the comparison between both the measured GSNR and fully predicted GSNR, and the ΔGSNR distributions for the two CUTs. The total RMSE value of the GSNR estimation is 0.3 dB for CUT 7 and 0.5 dB for CUT 73. Additionally, it can be observed in this case that the ML-aided prediction does not contain a bias for either of these CUTs. As the same behaviour is expected across the entire spectrum, it is possible to set a margin that yields conservative results in most cases. However, this feature is not guaranteed when using the GNPy due to the aforementioned estimation biases for the signal and ASE noise power predictions – this prevents a fixed margin, and hence a conservative result from always being reached. In this study,a margin of 0.5 dB is applied to the obtained predictions, shifting the error distributions as shown in Fig. 5.18; the error is calculated using Eq.5.2, with positive values of this quantity representing conservative GSNR estimations.

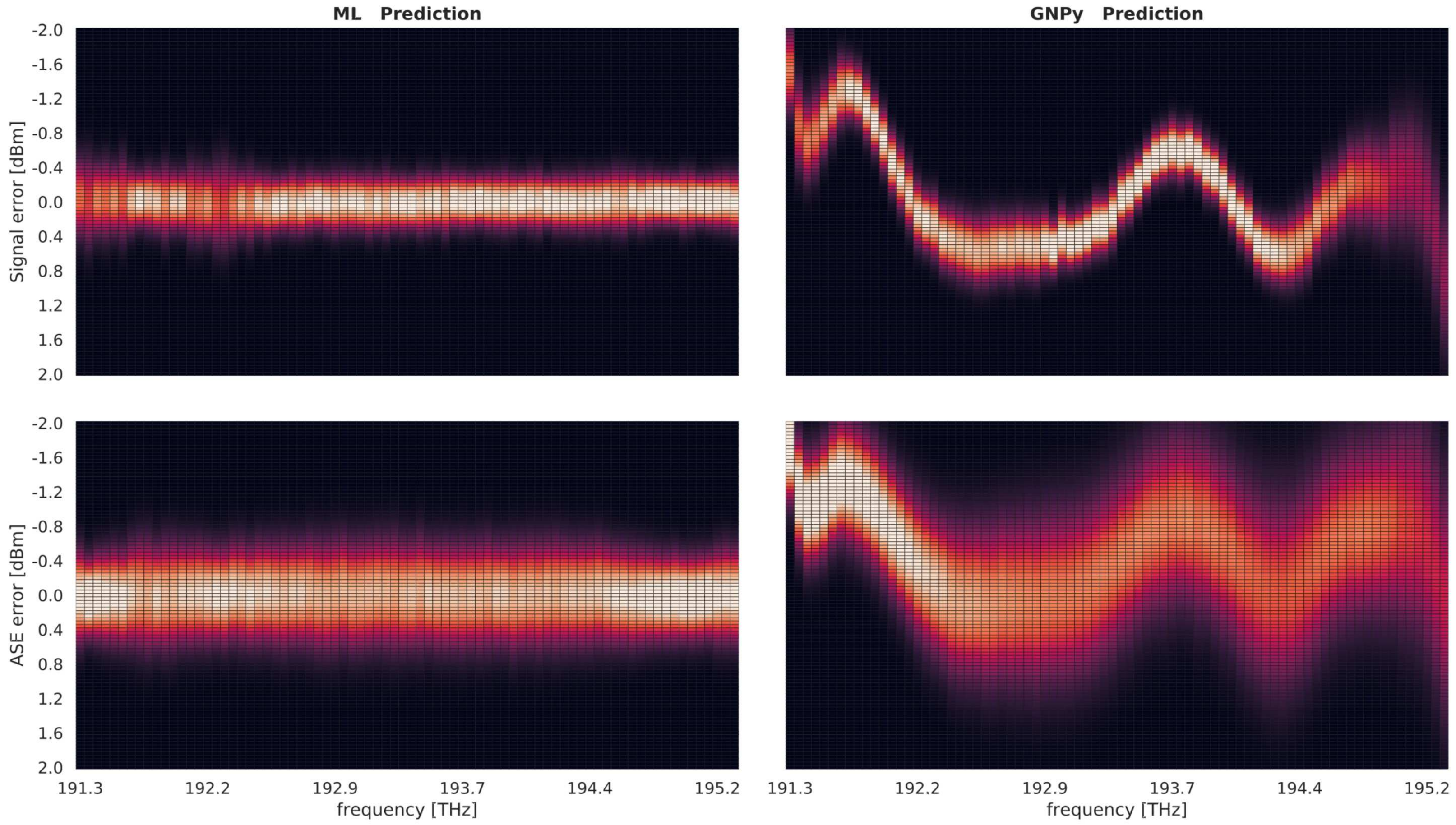

Fig. 5.15 Error distribution of the signal and ASE noise prediction obtained with the the ML models and the GNPy engine, respectively.

Remarkably, a margin of this size does not significantly affect the accuracy of the final predictions and is limited with respect to most currently employed design margins [147]. This procedure provides a 90.5% and 94.6% conservative GSNR prediction for CUTs 7 and 73, respectively. Moreover, such a margin may also be defined to take into account additional SNR degradations, e.g. filtering penalties.

In conclusion, the separate estimation of these two quantities can be used to optimize the OLS settings, further increasing the accuracy of the proposed QoT-E and improving the SNR $_{\mathrm{NL}}$ predictions, shown in Fig. 5.14 as a future implementation.

It is worth noticing that the proposed solution is completely agnostic with respect to both the hardware and the control strategy, as it only requires ASE-shaped generators and measurements from the OCMs, both commonly available in ROADM input and output, in order to create a ML training dataset. Consequently, the presented methodology is demonstrated to be a feasible and non-intrusive method for lightpath feasibility computation improvements, allowing a seamless increase in network performance.

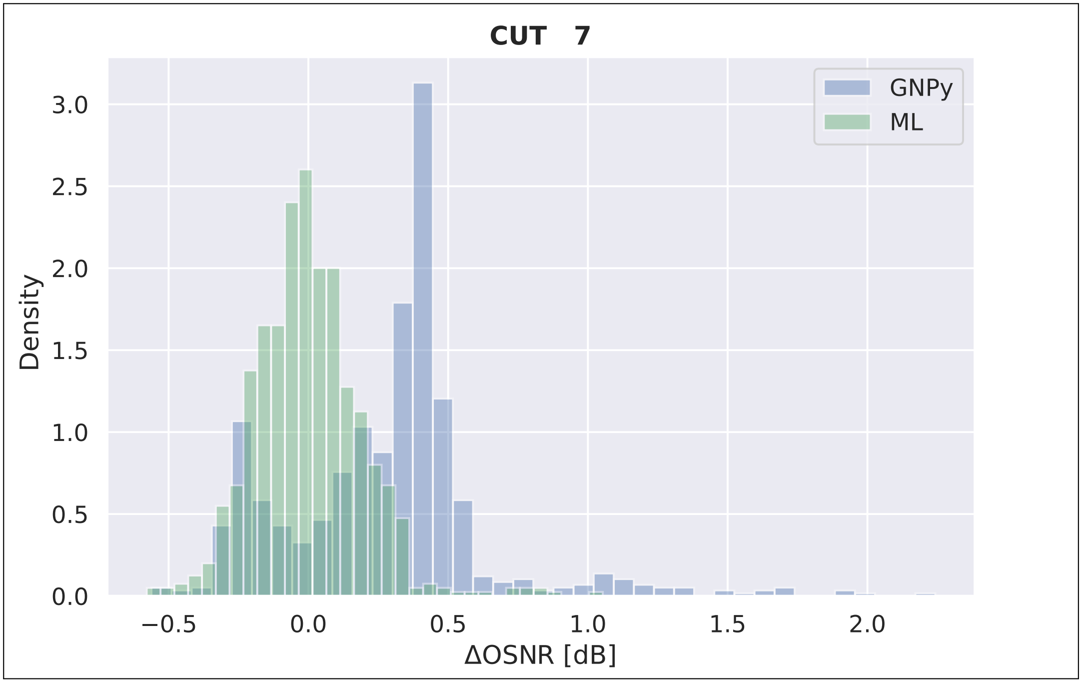

Fig. 5.16 The error distribution for the OSNR predictions provided by the GNPy engine and the ML algorithm, for CUT 7.

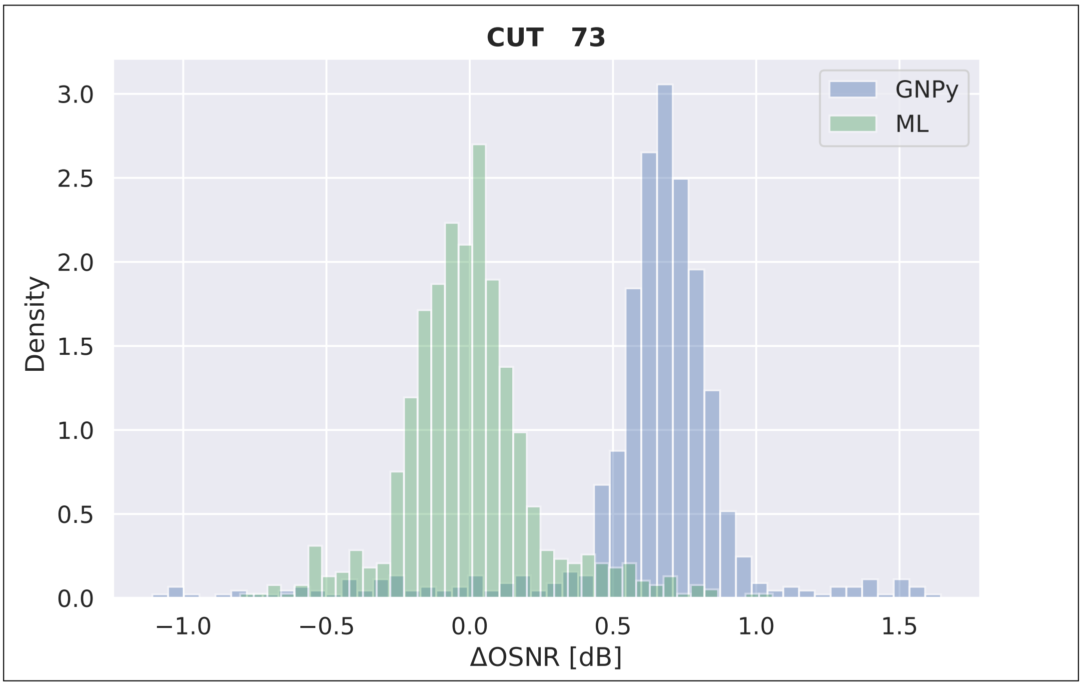

Fig. 5.17 The error distribution for the OSNR predictions provided by the GNPy engine and the ML algorithm, for CUT 73.

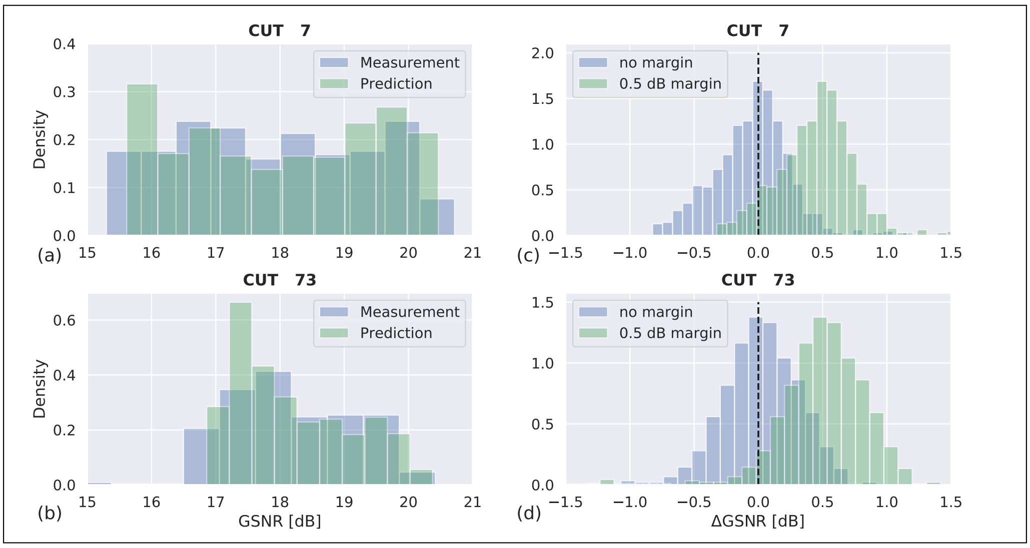

Fig. 5.18 The measured and predicted GSNR power distributions for: (a) CUT 7 and (b) CUT 73, along with the corresponding ΔGSNR power distributions with and without a 0.5 dB margin for: (c) CUT 7 and (d) CUT 73.

Chapter 6

Conclusions

In this thesis work, efficient and analytical models and ML solutions have been proposed and validated in an open and partially disaggregated framework.

First, a general introduction regarding SDN and open and partially disaggregated optical networks is given, describing the importance of an accurate and reliable digital model for an optimal network planning and control.

Chapter 2 introduces a comprehensive formulation for physical layer modeling of each network element. It presents an efficient and precise approximation of the GGN model, which serves as a fast solution for multi-band transmission scenarios. Additionally, a perturbative solution for SRS is proposed, providing explicit formulations for higher-order terms in the SRS-induced power transfer. The chapter also delves into the statistical approach for analyzing the PDL effect.

Chapter 3 focuses on demonstrating the improved implementation of GNPy, utilizing the proposed transmission models. The experimental validation is carried out in a 20-span testbed located at Orange Labs. GNPy exhibits significant accuracy in flex-grid, flex-rate transmission scenarios up to 800 Gbit/s, including Nyquist multi-subcarrier transceivers. Moreover, the chapter presents validations of a statistical approach to model the PDL effect.

In Chapter 4, the proposed digital model is validated through extensive simulation campaigns based on the SSFM and the numerical solution of SRS. The chapter proposes a model-driven approach for optimizing multi-band transmission problems, achieving highly satisfactory results by extending the LOGO framework in a fast and descriptive manner.

Finally, Chapter 5 introduces two ML solutions, which are experimentally validated for a variable spectral load transmission scenario. The implementation of DNN enables accurate predictions of signal and ASE noise power fluctuations induced by the behavior of EDFA in partially loaded transmission scenarios.

6.1 Future Work

As a matter of fact, GNPy has gained an increasing interest for both academia and industry, representing an accurate, vendor-agnostic QoT estimator used for network design and standards definition and for lightpath computation, paving the way towards a SDN in open and disaggregated optical networks planning and controlling. This broad interest in GNPy is due to the rising request in optical network communities of a reliable and efficient digital twin of the optical systems.

In order to catch up on this request, future research activities will be focused towards the development of an advanced software framework based on an improved digital twin implementation, including a more precise and efficient physical-layer signal propagation model, along with a faster and more flexible structure, to enable the simulation of new transmission technologies, dynamic application of automated AI, and heuristic methods for optimization and margin management in software-defined networks. This software framework, integrating the QoT engine with AI and heuristic methods, can be considered from two main perspectives, both of which are particularly interesting and imply significant benefits for real network applications:

- **Direct approach -** the accuracy and reliability of QoT estimations are leveraged for lightpath computation and modulation format feasibility, along with power optimization, soft-failure forecasting and physical-layer-based optimal routing and wavelength assignment, enabled by heuristic and AI algorithms.
- **Indirect approach -** heuristic and AI algorithms leverage the accuracy of the QoT engine to provide adequate system margins and/or to probe the optical system by estimating unknown or inaccurate physical parameters; a sort of QoT-based optical network tomography. In this scenario, an improved

implementation of an advance orchestration utilizes information retrieved from QoT, telemetry and sensing, combining and harmonizing in order to deliver an innovative framework for both network performance analysis and forecasting, and environmental observation and recognition.

References

[1] Cisco visual networking index: Forecast and methodology. https://www.cisco.com/c/en/us/solutions/service-provider/visual-networking-index-vni/index.html, 2018. [Online; accessed 25-April-2023].

[2] Glenn Wellbrock and Tiejun J Xia. How will optical transport deal with future network traffic growth? In *2014 The European Conference on Optical Communication (ECOC)*, pages 1–3. IEEE, 2014.

[3] D.-S. Ly-Gagnon, S. Tsukamoto, K. Katoh, and K. Kikuchi. Coherent detection of optical quadrature phase-shift keying signals with carrier phase estimation. *Journal of Lightwave Technology*, 24(1):12–21, 2006.

[4] M.G. Taylor. Coherent detection method using dsp for demodulation of signal and subsequent equalization of propagation impairments. *IEEE Photonics Technology Letters*, 16(2):674–676, 2004.

[5] V. Curri, P. Poggiolini, A. Carena, and F. Forghieri. Dispersion compensation and mitigation of nonlinear effects in 111-gb/s wdm coherent pm-qpsk systems. *IEEE Photonics Technology Letters*, 20(17):1473–1475, 2008.

[6] Seb J. Savory, Giancarlo Gavioli, Robert I. Killey, and Polina Bayvel. Electronic compensation of chromatic dispersion using a digital coherent receiver. *Opt. Express*, 15(5):2120–2126, Mar 2007.

[7] Henning Bulow, Fred Buchali, and Axel Klekamp. Electronic dispersion compensation. *Journal of Lightwave Technology*, 26(1):158–167, 2008.

[8] Seb J. Savory. Digital coherent optical receivers: Algorithms and subsystems. *IEEE Journal of Selected Topics in Quantum Electronics*, 16(5):1164–1179, 2010.

[9] Sheryl L. Woodward, Mark D. Feuer, and Paparao Palacharla. Chapter 15 - roadm-node architectures for reconfigurable photonic networks. In Ivan P. Kaminow, Tingye Li, and Alan E. Willner, editors, *Optical Fiber Telecommunications (Sixth Edition)*, Optics and Photonics, pages 683–707. Academic Press, Boston, sixth edition edition, 2013.

[10] Jan Kundrát, Ondřej Havliš, Jaroslav Jedlinskỳ, and Josef Vojtěch. Opening up roadms: let us build a disaggregated open optical line system. *Journal of Lightwave Technology*, 37(16):4041–4051, 2019.

[11] A. Campanella, H. Okui, A. Mayoral, D. Kashiwa, O. Gonzalez de Dios, D. Verchere, Q. Pham Van, A. Giorgetti, R. Casellas, R. Morro, and L. Ong. Odtn: Open disaggregated transport network. discovery and control of a disaggregated optical network through open source software and open apis. In *Optical Fiber Communication Conference (OFC) 2019*, page M3Z.4. Optica Publishing Group, 2019.

[12] Ramon Casellas, Ricardo Martínez, Ricard Vilalta, and Raül Muñoz. Abstraction and control of multi-domain disaggregated optical networks with openroadm device models. *Journal of Lightwave Technology*, 38(9):2606–2615, 2020.

[13] Alessio Giorgetti, Andrea Sgambelluri, Ramon Casellas, Roberto Morro, Andrea Campanella, and Piero Castoldi. Control of open and disaggregated transport networks using the open network operating system (onos) [invited]. *J. Opt. Commun. Netw.*, 12(2):A171–A181, Feb 2020.

[14] C Manso, R Muñoz, N Yoshikane, R Casellas, R Vilalta, R Martínez, T Tsuritani, and I Morita. Tapi-enabled sdn control for partially disaggregated multi-domain (ols) and multi-layer (wdm over sdm) optical networks. *Journal of Optical Communications and Networking*, 13(1):A21–A33, 2021.

[15] Vittorio Curri. Gnpy model of the physical layer for open and disaggregated optical networking. *J. Opt. Commun. Netw.*, 14(6):C92–C104, Jun 2022.

[16] Emilio Riccardi, Paul Gunning, Óscar González de Dios, Marco Quagliotti, Víctor López, and Andrew Lord. An operator view on the introduction of white boxes into optical networks. *Journal of Lightwave Technology*, 36(15):3062–3072, 2018.

[17] Internet Engineering Task Force. https://www.ietf.org/. Accessed: June 4, 2023.

[18] Open Networking Foundation. https://opennetworking.org/. Accessed: June 4, 2023.

[19] OIF (Optical Internetworking Forum). https://www.oiforum.com/. Accessed: June 4, 2023.

[20] Open ROADM. http://www.openroadm.org/. Accessed: June 4, 2023.

[21] OpenConfig. https://www.openconfig.net/. Accessed: June 4, 2023.

[22] Telecom Infra Project. https://telecominfraproject.com/. Accessed: June 4, 2023.

[23] TIP OOPT MUST. Optical Whitepaper Target Architecture for Disaggregated Open Optical Networks v. 10. https://cdn.brandfolder.io/D8DI15S7/at/k53xb6fw8f7nrjnw4fvx4c8/TIP_OOPT_MUST_Optical_Whitepaper_Target_Architecture_-_Disaggregated_Open_Optical_Networks__v10_-_GREENPUBLIC_ACCESS.pdf. Accessed: June 4, 2023.

[24] OpenROADM. Device White Paper v. 1.2. https://0201.nccdn.net/4_2/000/000/072/2aa/open-roadm-msa-release-7-device-white-paper-v1.2.pdf. Accessed: June 4, 2023.

[25] Danshi Wang, Zhiguo Zhang, Min Zhang, Meixia Fu, Jin Li, Shanyong Cai, Chunyu Zhang, and Xue Chen. The role of digital twin in optical communication: Fault management, hardware configuration, and transmission simulation. *IEEE Communications Magazine*, 59(1):133–139, 2021.

[26] R. Vilalta, R. Casellas, Ll. Gifre, R. Mu noz, R. Martínez, A. Pastor, D. López, and J.P. Fernández-Palacios. Architecture to deploy and operate a digital twin optical network. In *Optical Fiber Communication Conference (OFC) 2022*, page W1F.4. Optica Publishing Group, 2022.

[27] Vittorio Curri. Digital-twin of physical-layer as enabler for open and disaggregated optical networks. In *2023 International Conference on Optical Network Design and Modeling (ONDM)*, pages 1–6, 2023.

[28] GitHub repository of GNPy. https://github.com/Telecominfraproject/oopt-gnpy.

[29] B. Ramamurthy, H. Feng, D. Datta, J.P. Heritage, and B. Mukherjee. Transparent vs. opaque vs. translucent wavelength-routed optical networks. In *OFC/IOOC . Technical Digest. Optical Fiber Communication Conference, 1999, and the International Conference on Integrated Optics and Optical Fiber Communication*, volume 1, pages 59–61 vol.1, 1999.

[30] D.A. Schupke and D. Sellier. Lightpath configuration of transparent and static wdm networks for ip traffic. In *ICC 2001. IEEE International Conference on Communications. Conference Record (Cat. No.01CH37240)*, volume 2, pages 494–498 vol.2, 2001.

[31] Nicola Sambo, Yvan Pointurier, Filippo Cugini, Luca Valcarenghi, Piero Castoldi, and Ioannis Tomkos. Lightpath establishment assisted by offline qot estimation in transparent optical networks. *J. Opt. Commun. Netw.*, 2(11):928–937, Nov 2010.

[32] Mark Filer, Mattia Cantono, Alessio Ferrari, Gert Grammel, Gabriele Galimberti, and Vittorio Curri. Multi-Vendor Experimental Validation of an Open Source QoT Estimator for Optical Networks. *J. of Lightwave Tech.*, 36(15):3073–3082, aug 2018.

[33] Martin Birk, Olivier Renais, Guillaume Lambert, Christophe Betoule, Gilles Thouenon, Ahmed Triki, Dhruv Bhardwaj, Shweta Vachhani, Narayan Padi, and Simon Tse. The openroadm initiative. *IEEE/OSA Journal of Optical Communications and Networking*, 12(6):C58–C67, 2020.

[34] Ahmed Triki, Esther Le Rouzic, Olivier Renais, Guillaume Lambert, Gilles Thouenon, Christophe Betoule, Emmanuelle Delfour, Shweta Vachhani, and Balagangadhar Bathula. Open-source qot estimation for impairment-aware path computation in openroadm compliant network. In *2020 European Conference on Optical Communications (ECOC)*, pages 1–3, 2020.

[35] E. Le Rouzic, A Lindgren, S. Melin, D. Provencher, R. Subramanian, R. Joyce, F. Moore, D. Reeves, A. Rambaldi, P. Kaczmarek, K. Weeks, S. Neidlinger, G. Agrawal, S. Krishnamoha, B. Raszczyk, T. Uhlar, R. Casellas, O. Gonzalez de Dios, and V. Lopez. Operationalizing partially disaggregated optical networks: An open standards-driven multi-vendor demonstration. In *2021 Optical Fiber Communications Conference and Exhibition (OFC)*, pages 1–3, 2021.

[36] Vittorio Curri. Software-defined wdm optical transport in disaggregated open optical networks. In *2020 22nd International Conference on Transparent Optical Networks (ICTON)*, pages 1–4, 2020.

[37] Yvan Pointurier. Design of low-margin optical networks. *Journal of Optical Communications and Networking*, 9(1):A9–A17, 2017.

[38] Govind P Agrawal. *Fiber-optic communication systems*. John Wiley & Sons, 2012.

[39] Toru Mano, Andrea D'Amico, Emanuele Virgillito, Giacomo Borraccini, Yue-Kai Huang, Kei Kitamura, Kazuya Anazawa, Akira Masuda, Hideki Nishizawa, Ting Wang, Koji Asahi, and Vittorio Curri. Accuracy of nonlinear interference estimation on launch power optimization in short-reach systems with field trial. In *2022 European Conference on Optical Communication (ECOC)*, pages 1–4, 2022.

[40] Toru Mano, Andrea D'Amico, Emanuele Virgillito, Giacomo Borraccini, Yue-Kai Huang, Kazuya Anazawa, Hideki Nishizawa, Ting Wang, Koji Asahi, and Vittorio Curri. Modeling transceiver ber-osnr characteristic for qot estimation in short-reach systems. In *2023 International Conference on Optical Network Design and Modeling (ONDM)*, pages 1–3, 2023.

[41] A. Ferrari, M. Filer, K. Balasubramanian, Y. Yin, E. Le Rouzic, J. Kundrat, G. Grammel, G. Galimberti, and V. Curri. GNPy: an open source application for physical layer aware open optical networks. *IEEE/OSA Journal of Optical Communications and Networking*, 12(6):C31–C40, 2020.

[42] Andrea D'Amico, Stefano Straullu, Giacomo Borraccini, Elliot London, Stefano Bottacchi, Stefano Piciaccia, Alberto Tanzi, Antonino Nespola, Gabriele

Galimberti, Scott Swail, et al. Enhancing lightpath qot computation with machine learning in partially disaggregated optical networks. *IEEE Open Journal of the Communications Society*, 2:564–574, 2021.

[43] Andrea D'Amico, Elliot London, Bertrand Le Guyader, Florian Frank, Esther Le Rouzic, Erwan Pincemin, Nicolas Brochier, and Vittorio Curri. Experimental validation of gnpy in a multi-vendor flex-grid flex-rate wdm optical transport scenario. *J. Opt. Commun. Netw.*, 14(3):79–88, Mar 2022.

[44] Govind Agrawal. *Nonlinear Fiber Optics*. Academic Press, Boston, fifth edition, 2013.

[45] Tingye Li. *Optical fiber communications: fiber fabrication*. Elsevier, 2012.

[46] S Walker. Rapid modeling and estimation of total spectral loss in optical fibers. *J. Lightw. Technol.*, 4(8):1125–1131, 8 1986.

[47] Giacomo Borraccini, Andrea D'Amico, Stefano Straullu, Antonino Nespola, Stefano Piciaccia, Alberto Tanzi, Gabriele Galimberti, Stefano Bottacchi, Scott Swail, and Vittorio Curri. Cognitive and autonomous QoT-driven optical line controller. *Journal of Optical Communications and Networking*, 13(10):E23–E31, 2021.

[48] Gordon A Thomas, Boris I Shraiman, Paul F Glodis, and Michael J Stephen. Towards the clarity limit in optical fibre. *Nature*, 404(6775):262–264, 2000.

[49] Jake Bromage. Raman amplification for fiber communications systems. *J. Lightw. Technol.*, 22(1):79, 1 2004.

[50] Erwan Pincemin, Didier Grot, Laurence Bathany, Stéphane Gosselin, Michel Joindot, Sylvain Bordais, Yves Jaouen, and Jean-Marc Delavaux. Raman gain efficiencies of modern terrestrial transmission fibers in S-, C-and L-band. In *Nonlinear Guided Waves and Their Applications*, page NLTuC2. Optical Society of America, 2002.

[51] Karsten Rottwitt, Jake Bromage, Andrew J Stentz, Lufeng Leng, Malcolm E Lines, and Henrik Smith. Scaling of the Raman gain coefficient: applications to germanosilicate fibers. *Journal of lightwave technology*, 21(7):1652, 2003.

[52] D.N. Christodoulides and R.B. Jander. Evolution of stimulated raman crosstalk in wavelength division multiplexed systems. *IEEE Photonics Technology Letters*, 8(12):1722–1724, 1996.

[53] M Zirngibl. Analytical model of raman gain effects in massive wavelength division multiplexed transmission systems. *Electronics Letters*, 34(8):789–790, 1998.

[54] Chiara Lasagni, Paolo Serena, Alberto Bononi, and Jean-Christophe Antona. A generalized raman scattering model for real-time snr estimation of multiband systems. *Journal of Lightwave Technology*, pages 1–11, 2023.

[55] AR Chraplyvy. Optical power limits in multi-channel wavelength-division-multiplexed systems due to stimulated raman scattering. *Electronics letters*, 2(20):58–59, 1984.

[56] Mattia Cantono, Dario Pilori, Alessio Ferrari, Clara Catanese, Jordane Thouras, Jean-Luc Augé, and Vittorio Curri. On the interplay of nonlinear interference generation with stimulated raman scattering for qot estimation. *Journal of Lightwave Technology*, 36(15):3131–3141, 2018.

[57] Daniel Semrau, Eric Sillekens, Polina Bayvel, and Robert I Killey. Modeling and mitigation of fiber nonlinearity in wideband optical signal transmission. *Journal of Optical Communications and Networking*, 12(6):C68–C76, 2020.

[58] Chiara Lasagni, Paolo Serena, and Alberto Bononi. A raman-aware enhanced gn-model to estimate the modulation format dependence of the snr tilt in c+ l band. In *45th European Conference on Optical Communication (ECOC 2019)*, pages 1–4. IET, 2019.

[59] Andrea D'Amico, Bertrand Le Guyader, Florian Frank, Esther Le Rouzic, Erwan Pincemin, Nicolas Brochier, and Vittorio Curri. An experimental observation of the disaggregated nonlinear interference noise generation. In *2022 Asia Communications and Photonics Conference (ACP)*, pages 530–533, 2022.

[60] Curtis R. Menyuk and Brian S. Marks. Interaction of polarization mode dispersion and nonlinearity in optical fiber transmission systems. *J. Lightwave Technol.*, 24(7):2806, Jul 2006.

[61] Dario Pilori, Mattia Cantono, Alessio Ferrari, Andrea Carena, and Vittorio Curri. Observing the effect of polarization mode dispersion on nonlinear interference generation in wide-band optical links. *OSA Continuum*, 2(10):2856–2863, Oct 2019.

[62] S. Tariq and J.C. Palais. A computer model of non-dispersion-limited stimulated Raman scattering in optical fiber multiple-channel communications. *Journal of Lightwave Technology*, 11(12):1914–1924, 1993.

[63] P. Poggiolini et al. The GN-model of fiber non-linear propagation and its applications. *IEEE / OSA JLT*, 32.4:694–721, 2014.

[64] Ankush Mahajan, Konstantinos Christodoulopoulos, Ricardo Martínez, Salvatore Spadaro, and Raul Muñoz. Modeling EDFA gain ripple and filter penalties with machine learning for accurate QoT estimation. *Journal of Lightwave Technology*, 38(9):2616–2629, 2020.

[65] Rodolfo Di Muro. The er3+ -fiber gain coefficient derived from a dynamic gain tilt technique. *J. Lightwave Technol.*, 18(3):343, Mar 2000.

[66] Mi Wang, Liangjia Zong, Lei Mao, Andres Marquez, Yabin Ye, Han Zhao, and Francisco Javier Vaquero Caballero. Lcos slm study and its application in wavelength selective switch. In *Photonics*, volume 4, page 22. Multidisciplinary Digital Publishing Institute, 2017.

[67] Antonio Mecozzi and Mark Shtaif. Signal-to-noise-ratio degradation caused by polarization-dependent loss and the effect of dynamic gain equalization. *J. Lightwave Technol.*, 22(8):1856, Aug 2004.

[68] Andrea D'Amico, Giacomo Borraccini, Stefano Straullu, Francesco Aquilino, Stefano Piciaccia, Alberto Tanzi, Gabriele Galimberti, and Vittorio Curri. Statistical analysis of pdl penalty on coherent transmission technologies based on wss experimental characterization. In *2022 Asia Communications and Photonics Conference (ACP)*, pages 874–877, 2022.

[69] Andrea D'Amico, Giacomo Borraccini, Stefano Straullu, Francesco Aquilino, Stefano Piciaccia, Alberto Tanzi, Gabriele Galimberti, and Vittorio Curri. Experimental probing and modeling of the pdl impact on the optical signal-to-noise ratio. In *Optical Fiber Communication Conference (OFC) 2023*, page W1E.6. Optica Publishing Group, 2023.

[70] N Gisin. Statistics of polarization dependent losses. *Optics Communications*, 114(5):399–405, 1995.

[71] A. El Amari, N. Gisin, B. Perny, H. Zbinden, and C.W. Zimmer. Statistical prediction and experimental verification of concatenations of fiber optic components with polarization dependent loss. *Journal of Lightwave Technology*, 16(3):332–339, 1998.

[72] B. Huttner, C. Geiser, and N. Gisin. Polarization-induced distortions in optical fiber networks with polarization-mode dispersion and polarization-dependent losses. *IEEE Journal of Selected Topics in Quantum Electronics*, 6(2):317–329, 2000.

[73] Y. Fukada. Probability density function of polarization dependent loss (pdl) in optical transmission system composed of passive devices and connecting fibers. *Journal of Lightwave Technology*, 20(6):953–964, 2002.

[74] A. Galtarossa and L. Palmieri. The exact statistics of polarization-dependent loss in fiber-optic links. *IEEE Photonics Technology Letters*, 15(1):57–59, 2003.

[75] A. Mecozzi and M. Shtaif. Signal-to-noise-ratio degradation caused by polarization-dependent loss and the effect of dynamic gain equalization. *Journal of Lightwave Technology*, 22(8):1856–1871, 2004.

[76] Lynn E. Nelson, Cristian Antonelli, Antonio Mecozzi, Martin Birk, Peter Magill, Anton Schex, and Lutz Rapp. Statistics of polarization dependent loss in an installed long-haul wdm system. *Opt. Express*, 19(7):6790–6796, Mar 2011.

[77] Segev Zarkosvky and Mark Shtaif. Statistical distribution of polarization-dependent loss in systems characterized by the hinge model. *Opt. Lett.*, 45(5):1224–1227, Mar 2020.

[78] Andrea D'Amico, Elliot London, Bertrand Le Guyader, Florian Frank, Esther Le Rouzic, Erwan Pincemin, Nicolas Brochier, and Vittorio Curri. Gnpy experimental validation on flex-grid, flex-rate wdm optical transport scenarios. In *Optical Fiber Communication Conference*, pages W1G–2. Optical Society of America, 2021.

[79] A. D'Amico, B. Le Guyader, F. Frank, E. Le Rouzic, E. Pincemin, A. Napoli, H. Sun, B. Spinnler, N. Brochier, and V. Curri. Gnpy experimental validation for nyquist subcarriers flexible transmission up to 800 g. In *2022 Optical Fiber Communications Conference and Exhibition (OFC)*, pages 1–3, 2022.

[80] Li Yan, Erik Agrell, Madushanka Nishan Dharmaweera, and Henk Wymeersch. Joint assignment of power, routing, and spectrum in static flexible-grid networks. *Journal of Lightwave Technology*, 35(10):1766–1774, 2017.

[81] Vittorio Curri, Andrea Carena, Andrea Arduino, Gabriella Bosco, Pierluigi Poggiolini, Antonino Nespola, and Fabrizio Forghieri. Design strategies and merit of system parameters for uniform uncompensated links supporting nyquist-wdm transmission. *Journal of Lightwave Technology*, 33(18):3921–3932, 2015.

[82] Andrea D'Amico, Elliot London, Emanuele Virgillito, Antonio Napoli, and Vittorio Curri. Quality of transmission estimation for planning of disaggregated optical networks. In *2020 International Conference on Optical Network Design and Modeling (ONDM)*, pages 1–3. IEEE, 2020.

[83] Mark Filer, Mattia Cantono, Alessio Ferrari, Gert Grammel, Gabriele Galimberti, and Vittorio Curri. Multi-Vendor Experimental Validation of an Open Source QoT Estimator for Optical Networks. *Journal of Lightwave Technology*, 36(15):3073–3082, aug 2018.

[84] Alessio Ferrari, Mark Filer, Karthikeyan Balasubramanian, Yawei Yin, Esther Le Rouzic, Jan Kundrát, Gert Grammel, Gabriele Galimberti, and Vittorio Curri. Gnpy: an open source application for physical layer aware open optical networks. *J. Opt. Commun. Netw.*, 12(6):C31–C40, Jun 2020.

[85] Alessio Ferrari, Karthikeyan Balasubramanian, Mark Filer, Yawei Yin, Esther Le Rouzic, Jan Kundrát, Gert Grammel, Gabriele Galimberti, and Vittorio Curri. Assessment on the in-field lightpath qot computation including connector loss uncertainties. *J. Opt. Commun. Netw.*, 13(2):A156–A164, Feb 2021.

[86] Giacomo Borraccini, Andrea D'Amico, Stefano Straullu, Antonino Nespola, Stefano Piciaccia, Alberto Tanzi, Gabriele Galimberti, Stefano Bottacchi, Scott Swail, and Vittorio Curri. Cognitive and autonomous qot-driven optical line controller. *J. Opt. Commun. Netw.*, 13(10):E23–E31, 10 2021.

[87] K. Ishida, H. Goto, K. Matsuda, M. Binkai, T. Yoshida, T. Tokura, and T. Mizuochi. Experimental study of spm and xpm using real time coherent dsp for roadm systems. In *2013 18th OptoElectronics and Communications Conference held jointly with 2013 International Conference on Photonics in Switching*, page TuR1 3. Optica Publishing Group, 2013.

[88] A. Nafta and M. Shtaif. The ultimate cost of pdl in fiber-optic systems. In *Conference on Lasers and Electro-Optics/International Quantum Electronics Conference*, page CMC2. Optica Publishing Group, 2009.

[89] Joana Girard-Jollet, Matteo Lonardi, Petros Ramantanis, Paolo Serena, Chiara Lasagni, Patricia Layec, and Jean-Christophe Antona. Estimating network components polarization-dependent loss using performance statistical measurements. In *2021 European Conference on Optical Communication (ECOC)*, pages 1–4, 2021.

[90] Matteo Lonardi, Paolo Serena, Petros Ramantanis, Nicola Rossi, and Simone Musetti. Kerr nonlinearity dominance diagnostic for polarization-dependent loss impaired optical transmissions. In *2021 European Conference on Optical Communication (ECOC)*, pages 1–4, 2021.

[91] Kaoutar Benyahya, Christian Simonneau, Amirhossein Ghazisaeidi, Philippe Plantady, Alexis Carbo Meseguer, Alain Calsat, Haik Mardoyan, Vincent Letellier, and Jérémie Renaudier. Analysis of impact of polarization dependent loss in point to multi-point subsea communication systems. In *Optical Fiber Communication Conference*, pages M2C–2. Optica Publishing Group, 2022.

[92] R Pastorelli, S Piciaccia, G Galimberti, E Self, M Brunella, G Calabretta, F Forghieri, D Siracusa, A Zanardi, E Salvadori, et al. Optical control plane based on an analytical model of non-linear transmission effects in a self-optimized network. In *39th European Conference and Exhibition on Optical Communication (ECOC 2013)*, pages 1–3. IET, 2013.

[93] Andrea D'Amico, Elliot London, Emanuele Virgillito, Antonio Napoli, and Vittorio Curri. Inter-band gsnr degradations and leading impairments in c+l band 400g transmission. In *2021 International Conference on Optical Network Design and Modeling (ONDM)*, pages 1–3, 2021.

[94] Emanuele Virgillito, Elliot London, Andrea D'Amico, Bruno Correia, Antonio Napoli, and Vittorio Curri. Single- vs. multi-band optimized power control in c+l wdm 400g line systems. In *2021 Optical Fiber Communications Conference and Exhibition (OFC)*, pages 1–3, 2021.

[95] Fukutaro Hamaoka, Masanori Nakamura, Seiji Okamoto, Kyo Minoguchi, Takeo Sasai, Asuka Matsushita, Etsushi Yamazaki, and Yoshiaki Kisaka. Ultra-wideband wdm transmission in s-, c-, and l-bands using signal power optimization scheme. *Journal of Lightwave Technology*, 37(8):1764–1771, 2019.

[96] Bruno Correia, Rasoul Sadeghi, Emanuele Virgillito, Antonio Napoli, Nelson Costa, João Pedro, and Vittorio Curri. Power control strategies and network performance assessment for C+L+S multiband optical transport. *Journal of Optical Communications and Networking*, 13(7):147, jul 2021.

[97] Bruno Correia, Rasoul Sadeghi, Emanuele Virgillito, Antonio Napoli, and Vittorio Curri. Optical Power Control Strategies for Optimized C + L + S-bands Network Performance. In *Optical Fiber Communication Conference (OFC) 2021*, page W1F.8, 2021.

[98] Sam Nallaperuma, Nikita A. Shevchenko, and Seb J. Savory. Parameter Optimisation for Ultra-Wideband Optical Networks in the Presence of Stimulated Raman Scattering Effect. In *2021 International Conference on Optical Network Design and Modeling (ONDM)*, pages 1–6. IEEE, jun 2021.

[99] Henrique Buglia, Eric Sillekens, Anastasiia Vasylchenkova, Wenting Yi, Robert Killey, Polina Bayvel, and Lidia Galdino. Challenges in Extending Optical Fibre Transmission Bandwidth Beyond C+L Band and How to Get There. In *2021 International Conference on Optical Network Design and Modeling (ONDM)*, volume 3, pages 1–4. IEEE, jun 2021.

[100] Salma Escobar Landero, Ivan Fernandez, Jauregui Ruiz, Alessio Ferrari, Dylan Le Gac, Yann Frignac, and Gabriel Charlet. Link Power Optimization for S+C+L Multi-band WDM Coherent Transmission Systems. In *2022 Optical Fiber Communications Conference and Exhibition (OFC)*, pages 1–3. OSA, 2022.

[101] Amp-fl8221-sb-16 amplifier datasheet from fiberlabs inc.

[102] Uiara Celine de Moura, Md Asif Iqbal, Morteza Kamalian, Lukasz Krzczanowicz, Francesco Da Ros, Ann Margareth Rosa Brusin, Andrea Carena, Wladek Forysiak, Sergei Turitsyn, and Darko Zibar. Multi–band programmable gain Raman amplifier. *Journal of Lightwave Technology*, 39(2):429–438, 2021.

[103] Giacomo Borraccini, Stefano Straullu, Andrea D'Amico, Antonino Nespola, Stefano Piciaccia, Alberto Tanzi, Gabriele Galimberti, and Vittorio Curri. Autonomous Raman amplifiers in multi-band software-defined optical transport networks. *Journal of Optical Communications and Networking*, 13(10):E53–E62, 2021.

[104] Chiara Lasagni, Paolo Serena, and Alberto Bononi. Modeling nonlinear interference with sparse raman-tilt equalization. *Journal of Lightwave Technology*, 39(15):4980–4989, 2021.

[105] Andrea D'Amico, Stefano Straullu, Antonino Nespola, Ihtesham Khan, Elliot London, Emanuele Virgillito, Stefano Piciaccia, Aberto Tanzi, Gabriele Galimberti, and Vittorio Curri. Using machine learning in an open optical line system controller. *J. Opt. Commun. Netw.*, 12(6):C1–C11, Jun 2020.

[106] Emanuele Virgillito, Andrea D'Amico, Alessio Ferrari, and Vittorio Curri. Observing and modeling wideband generation of non-linear interference. In *2019 21st International Conference on Transparent Optical Networks (ICTON)*, pages 1–4. IEEE, 2019.

[107] Elliot London, Emanuele Virgillito, Andrea D'Amico, Antonio Napoli, and Vittorio Curri. Simulative assessment of non-linear interference generation within disaggregated optical line systems. *OSA Continuum*, 3(12):3378–3389, 2020.

[108] D. Pilori, M. Cantono, A. Carena, and V. Curri. FFSS: The fast fiber simulator software. In *2017 19th International Conference on Transparent Optical Networks (ICTON)*, pages 1–4, 2017.

[109] Simone Musetti, Paolo Serena, and A. Bononi. On the accuracy of split-step Fourier simulations for wideband nonlinear optical communications. *Journal of Lightwave Technology*, PP:1–1, 10 2018.

[110] Bruno Correia, Rasoul Sadeghi, Emanuele Virgillito, Antonio Napoli, Nelson Costa, Jo ao Pedro, and Vittorio Curri. Power control strategies and network performance assessment forc+l+s multiband optical transport. *J. Opt. Commun. Netw.*, 13(7):147–157, Jul 2021.

[111] E. London, E. Virgillito, A. D'Amico, A. Napoli, and V. Curri. Observing cross-channel NLI generation in disaggregated optical line systems. In *Asia Communications and Photonics Conference (ACP)*, 2021.

[112] A. Carena, G. Bosco, V. Curri, P. Poggiolini, M. Tapia Taiba, and F. Forghieri. Statistical characterization of PM-QPSK signals after propagation in uncompensated fiber links. In *36th European Conference and Exhibition on Optical Communication*, pages 1–3, 2010.

[113] Alessio Ferrari, Antonio Napoli, Johannes K Fischer, Nelson Costa, Andrea D'Amico, João Pedro, Wladek Forysiak, Erwan Pincemin, Andrew Lord, Alexandros Stavdas, et al. Assessment on the achievable throughput of multi-band itu-t g. 652. d fiber transmission systems. *Journal of Lightwave Technology*, 38(16):4279–4291, 2020.

[114] Alberto Bononi, Paolo Serena, and Nicola Rossi. Nonlinear signal–noise interactions in dispersion-managed links with various modulation formats. *Optical Fiber Technology*, 16(2):73–85, 2010.

[115] Pierluigi Poggiolini, Andrea Carena, Yanchao Jiang, Gabriela Bosco, Vittorio Curri, and Fabrizio Forghieri. Impact of low-osnr operation on the performance of advanced coherent optical transmission systems. In *2014 The European Conference on Optical Communication (ECOC)*, pages 1–3. IEEE, 2014.

[116] Vittorio Curri, Andrea Carena, Andrea Arduino, Gabriella Bosco, Pierluigi Poggiolini, Antonino Nespola, and Fabrizio Forghieri. Design strategies and merit of system parameters for uniform uncompensated links supporting nyquist-WDM transmission. *Journal of Lightwave Technology*, 33(18):3921–3932, sep 2015.

[117] Alessio Ferrari, Giacomo Borraccini, and Vittorio Curri. Observing the generalized snr statistics induced by gain/loss uncertainties. In *2019 European Conference on Optical Communication (ECOC)*. IEEE, 2019.

[118] Brian Taylor, Gilad Goldfarb, Saumil Bandyopadhyay, Vittorio Curri, and HansJuergen Schmidtke. Towards a route planning tool for open optical networks in the telecom infrastructure project. In *Optical Fiber Communication Conference/National Fiber Optic Engineers Conference 2018*, 2018.

[119] Maxim Bolshtyansky. Spectral hole burning in erbium-doped fiber amplifiers. *Journal of lightwave technology*, 21(4):1032–1038, 2003.

[120] Gert Grammel, Vittorio Curri, and Jean Luc Auge. Physical simulation environment of the telecommunications infrastructure project (tip). In *Optical Fiber Communication Conference/National Fiber Optic Engineers Conference 2018*, 2018.

[121] Maria Freire, Sébastien Mansfeld, Djamel Amar, Franck Gillet, Antoine Lavignotte, and Catherine Lepers. Predicting optical power excursions in erbium doped fiber amplifiers using neural networks. In *2018 Asia Communications and Photonics Conference (ACP)*, pages 1–3. IEEE, 2018.

[122] Jakob Thrane, Jesper Wass, Molly Piels, Julio CM Diniz, Rasmus Jones, and Darko Zibar. Machine learning techniques for optical performance monitoring from directly detected pdm-qam signals. *Journal of Lightwave Technology*, 35(4):868–875, 2017.

[123] Faisal Nadeem Khan, Chao Lu, and Alan Pak Tao Lau. Optical performance monitoring in fiber-optic networks enabled by machine learning techniques. In *2018 Optical Fiber Communications Conference and Exposition (OFC)*, pages 1–3. IEEE, 2018.

[124] Luca Barletta, Alessandro Giusti, Cristina Rottondi, and Massimo Tornatore. Qot estimation for unestablished lighpaths using machine learning. In *Optical Fiber Communication Conference*, pages Th1J–1. Optical Society of America, 2017.

[125] Ippokratis Sartzetakis, Konstantinos Kostas Christodoulopoulos, and Emmanouel Manos Varvarigos. Accurate quality of transmission estimation with machine learning. *Journal of Optical Communications and Networking*, 11(3):140–150, 2019.

[126] Weiyang Mo, Yue-Kai Huang, Shaoliang Zhang, Ezra Ip, Daniel C Kilper, Yoshiaki Aono, and Tsutomu Tajima. Ann-based transfer learning for qot prediction in real-time mixed line-rate systems. In *2018 Optical Fiber Communications Conference and Exposition (OFC)*, pages 1–3. IEEE, 2018.

[127] Cristina Rottondi, Luca Barletta, Alessandro Giusti, and Massimo Tornatore. Machine-learning method for quality of transmission prediction of unestablished lightpaths. *Journal of Optical Communications and Networking*, 10(2):A286–A297, 2018.

[128] Javier Mata, Ignacio De Miguel, Ramon J Duran, Noemi Merayo, Sandeep Kumar Singh, Admela Jukan, and Mohit Chamania. Artificial intelligence (ai) methods in optical networks: A comprehensive survey. *Optical Switching and Networking*, 28:43–57, 2018.

[129] Yvan Pointurier. Machine learning techniques for quality of transmission estimation in optical networks. *J. Opt. Commun. Netw.*, 13(4):B60–B71, Apr 2021.

[130] Shengxiang Zhu, Craig L Gutterman, Weiyang Mo, Yao Li, Gil Zussman, and Daniel C Kilper. Machine learning based prediction of erbium-doped fiber wdm line amplifier gain spectra. In *2018 European Conference on Optical Communication (ECOC)*, pages 1–3. IEEE, 2018.

[131] Maria Ionescu. Machine learning for ultrawide bandwidth amplifier configuration. In *2019 21st International Conference on Transparent Optical Networks (ICTON)*, pages 1–4. IEEE, 2019.

[132] Erick de A Barboza, Carmelo JA Bastos-Filho, Joaquim F Martins-Filho, Uiara C de Moura, and Juliano RF de Oliveira. Self-adaptive erbium-doped fiber amplifiers using machine learning. In *2013 SBMO/IEEE MTT-S International Microwave & Optoelectronics Conference (IMOC)*, pages 1–5. IEEE, 2013.

[133] Emmanuel Seve, Jelena Pesic, and Yvan Pointurier. Accurate qot estimation by means of a reduction of edfa characteristics uncertainties with machine learning. In *2020 International Conference on Optical Network Design and Modeling (ONDM)*, pages 1–3. IEEE, 2020.

[134] Yishen Huang, Craig L Gutterman, Payman Samadi, Patricia B Cho, Wiem Samoud, Cédric Ware, Mounia Lourdiane, Gil Zussman, and Keren Bergman. Dynamic mitigation of edfa power excursions with machine learning. *Optics express*, 25(3):2245–2258, 2017.

[135] Ankush Mahajan, Kostas Christodoulopoulos, Ricardo Martinez, Salvatore Spadaro, and Raul Munoz. Machine learning assisted edfa gain ripple modelling for accurate qot estimation. In *2019 European Conference on Optical Communication (ECOC)*. IEEE, 2019.

[136] Ankush Mahajan, Konstantinos Christodoulopoulos, Ricardo Martínez, Salvatore Spadaro, and Raul Muñoz. Modeling edfa gain ripple and filter penalties with machine learning for accurate qot estimation. *Journal of Lightwave Technology*, 38(9):2616–2629, 2020.

[137] https://www.cisco.com/c/en/us/products/collateral/optical-networking/ons-15454-series-multiservice-transport-platforms/data_sheet_c78-658542.html.

[138] https://www.tensorflow.org/.

[139] K Christodoulopoulos, C Delezoide, N Sambo, A Kretsis, I Sartzetakis, A Sgambelluri, N Argyris, G Kanakis, P Giardina, G Bernini, et al. Toward efficient, reliable, and autonomous optical networks: the orchestra solution. *IEEE/OSA Journal of Optical Communications and Networking*, 11(9):C10–C24, 2019.

[140] Rui Manuel Morais. Machine learning in multi-layer optical networks. In *Optical Fiber Communication Conference*, pages M1B–1. Optical Society of America, 2020.

[141] Danish Rafique and Luis Velasco. Machine learning for network automation: Overview, architecture, and applications [invited tutorial]. *J. Opt. Commun. Netw.*, 10(10):D126–D143, Oct 2018.

[142] Andrea Sgambelluri, J-L Izquierdo-Zaragoza, Alessio Giorgetti, Ll Gifre, Luis Velasco, Francesco Paolucci, Nicola Sambo, Francesco Fresi, Piero Castoldi, A Chiadò Piat, et al. Fully disaggregated roadm white box with netconf/yang control, telemetry, and machine learning-based monitoring. In *Optical Fiber Communication Conference*, pages Tu3D–12. Optical Society of America, 2018.

[143] https://www.cisco.com/c/en/us/products/collateral/optical-networking/ons-15454-series-multiservice-transport-platforms/data$_sheet_c78-658542.html$.

[144] ITU-T Recommendation G.694.1. SERIES G: TRANSMISSION SYSTEMS AND MEDIA, DIGITAL SYSTEMS AND NETWORKS - Transmission media characteristics – Characteristics of optical components and subsystems - Spectral grids for WDM applications: DWDM frequency grid. https://www.itu.int/rec/T-REC-G.694.1/en, 2002. [Online; accessed 14-January-2021].

[145] https://www.edge-core.com/productsList.php?cls=291&cls2=347.

[146] Alessio Ferrari, Mark Filer, Karthikeyan Balasubramanian, Yawei Yin, Esther Le Rouzic, Jan Kundrat, Gert Grammel, Gabriele Galimberti, and Vittorio Curri. Gnpy: an open source application for physical layer aware open optical networks. *Journal of Optical Communications and Networking*, 12(6):C31–C40, 2020.

[147] Polyzois Soumplis, Konstantinos Christodoulopoulos, Marco Quagliotti, Annachiara Pagano, and Emmanouel Varvarigos. Network planning with actual margins. *Journal of Lightwave Technology*, 35(23):5105–5120, 2017.